

REPORT DOCUMENTATION PAGE

Form Approved

AFRL-SR-BL-TR-98-

Public reporting burden for this collection of information is estimated to average 1 hour per response, including the time for and maintaining the data needed, and completing and reviewing the collection of information. Send comments regarding information, including suggestions for reducing this burden, to Washington Headquarters Services, Directorate for Information Operations, 1204, Arlington, VA 22202-4302, and to the Office of Management and Budget, Paperwork Reduction Project (0704-0188).

1. AGENCY USE ONLY (Leave Blank)	2. REPORT DATE February 1993	3. REPORT TYPE Final
----------------------------------	---------------------------------	-------------------------

6415

4. TITLE AND SUBTITLE Investigations of the GaN, AlN, and InN Semiconductors: Structural, Optical, Electronic and Interfacial Properties	5. FUNDING NUMBERS
---	--------------------

6. AUTHORS Samuel Clagett Strite III	5. FUNDING NUMBERS
---	--------------------

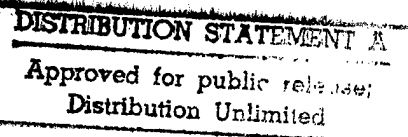
7. PERFORMING ORGANIZATION NAME(S) AND ADDRESS(ES) University of Illinois at Urbana-Champaign	8. PERFORMING ORGANIZATION REPORT NUMBER
--	--

9. SPONSORING/MONITORING AGENCY NAME(S) AND ADDRESS(ES) AFOSR/NI 110 Duncan Avenue, Room B-115 Bolling Air Force Base, DC 20332-8080	10. SPONSORING/MONITORING AGENCY REPORT NUMBER
---	--

11. SUPPLEMENTARY NOTES	12b. DISTRIBUTION CODE
-------------------------	------------------------

12a. DISTRIBUTION AVAILABILITY STATEMENT Approved for Public Release	12b. DISTRIBUTION CODE
---	------------------------

13. ABSTRACT (Maximum 200 words) See attached.	DISTRIBUTION STATEMENT A Approved for public release; Distribution Unlimited
---	--



DTIC QUALITY INSPECTED 4

19980505 135

14. SUBJECT TERMS	15. NUMBER OF PAGES
-------------------	---------------------

16. PRICE CODE

17. SECURITY CLASSIFICATION OF REPORT Unclassified	18. SECURITY CLASSIFICATION OF THIS PAGE Unclassified	19. SECURITY CLASSIFICATION OF ABSTRACT Unclassified	20. LIMITATION OF ABSTRACT UL
---	--	---	----------------------------------

AFRL-SR-BL-TR-98-

0415

**INVESTIGATIONS OF THE GaN, AlN AND InN SEMICONDUCTORS:
STRUCTURAL, OPTICAL, ELECTRONIC AND INTERFACIAL PROPERTIES**

BY

SAMUEL CLAGETT STRITE III

B.S., Bucknell University, 1987
M.S., University of Illinois, 1988

THESIS

Submitted in partial fulfillment of the requirements
for the degree of Doctor of Philosophy in Physics
in the Graduate College of the
University of Illinois at Urbana-Champaign, 1993

Urbana, Illinois

AUG 9 1993
JST

UNIVERSITY OF ILLINOIS AT URBANA-CHAMPAIGN

THE GRADUATE COLLEGE

FEBRUARY 1993

WE HEREBY RECOMMEND THAT THE THESIS BY

SAMUEL CLAGETT STRITE III

ENTITLED INVESTIGATIONS OF THE GaN, AlN and InN SEMICONDUCTORS:

STRUCTURAL, OPTICAL, ELECTRONIC AND INTERFACIAL PROPERTIES

BE ACCEPTED IN PARTIAL FULFILLMENT OF THE REQUIREMENTS FOR

THE DEGREE OF DOCTOR OF PHILOSOPHY

W. S. Rothery

Director of Thesis Research

Gal K. Ophir

Head of Department

Committee on Final Examination†

W. S. Rothery

Chairperson

Richard P. Mart

James H. Greene

Sh. D. Gilli

† Required for doctor's degree but not for master's.

INVESTIGATIONS OF THE GaN, AlN AND InN SEMICONDUCTORS:
STRUCTURAL, OPTICAL, ELECTRONIC AND INTERFACIAL PROPERTIES

Samuel Clagett Strite III, Ph.D.

Department of Physics

University of Illinois at Urbana-Champaign, 1993

H. Morkoç, Advisor

Abstract

Described in this thesis is an investigation of some fundamental physical properties of both zincblende and wurtzite Group III - Nitride wide bandgap semiconductor materials. All of the thin films studied were grown by plasma-enhanced molecular beam epitaxy on either GaAs and SiC substrates. This growth method proved to be suitable for nitride epitaxial growth although compromises between the plasma power and the crystal growth rate had to be sought. The zincblende polytypes of GaN and InN were studied with the intent of evaluating their potential as a wide bandgap semiconductor system for short wavelength optical devices. The metastability of these crystals has led us to the conclusion that the zincblende nitrides are not a promising candidate for these applications due to their tendency to nucleate wurtzite domains. Bulk samples of zincblende GaN and InN and wurtzite GaN, AlN and InN were studied by x-ray photoemission spectroscopy (XPS) in an effort to determine their valence band structure. We report the various energies of the valence band density of states maxima as well as the ionicity gaps of each material. Wurtzite GaN/AlN and InN/AlN heterostructures were also investigated by XPS in order to estimate the valence band discontinuities of these heterojunctions. We measured valence band discontinuities of $\Delta E_v^{\text{GaN/AlN}} = 0.4 \pm 0.4 \text{ eV}$ and $\Delta E_v^{\text{InN/AlN}} = 1.1 \pm 0.4 \text{ eV}$. Our results indicate that both systems have heterojunction band lineups fundamentally suitable for common optical device applications.

ACKNOWLEDGEMENTS

I would like to express my appreciation to many people who have helped me before and during my graduate studies. First, I must thank my thesis advisor, Prof. H. Morkoç, who provided me with the opportunity to pursue this project and the resources to succeed. I would especially like to thank Prof. A. Rockett for his guidance and collaboration throughout my graduate career. I gratefully acknowledge the outstanding contributions of Profs. D. J. Smith, W. J. Choyke, and H. Chen towards this work. Thanks are also due to the members of my thesis committee, Profs. R. Martin, L. Greene, and G. Gollin. Special mention is reserved for Prof. R. Henry of Bucknell University for his inspirational teaching which was influential in my choice of science as a career.

This work was made possible by funding from the Office of Naval Research under Contract # N00014-89J-1780. The Epicenter crystal growth facility was supported by the DOE under contract # DOE-DE-AC02-76ER01198. During different parts of my graduate career I was supported by National Science Foundation and Air Force Office of Scientific Research fellowships.

I owe a great deal of thanks to my fellow coworkers for their friendship, advice, and assistance. I would especially like to thank Dr. Selim Ünlü for his unique friendship and his profound influence on my development as a scientist. I wish to thank Levent Demirel for making long days in the MBE lab more pleasant. I benefitted from my discussions with Drs. J.-I. Chyi, B. Sverdlov, D. Mui, T. Lei, W. Lambrecht and N. Teraguchi. The technical assistance of D. Jeffers and B. Bowdish contributed greatly to my accomplishments. The friendships of S. White, J. Reed, K. Adomi, and G. Martin in the lab and Dan, Grayson,

the Bird, the Chimp, the Rabbit, Stainless, Schatz, Dr. Venkman, OG, the Colonel, Pudge, Shelly, van du Soleil, Marlin, Mishka, Pinar, Murat, Furth, Josh, Mary and Sara outside of the lab will remain with me.

Finally, I extend my warmest thanks to my father, my mother, and my brother for their support and encouragement of my strange endeavor over these many years.

TABLE OF CONTENTS

	Page
1. INTRODUCTION	1
2. PROPERTIES OF THE III-V NITRIDES	3
2.1 GaN	4
2.2 AlN	6
2.3 InN	7
3. MBE CRYSTAL GROWTH OF THE III-V NITRIDES	9
3.1 Substrates	9
3.1 Substrate Preparation	10
3.3 Crystal Growth	18
4. THE ZINCBLENDE NITRIDES AND POLYTYPISM	33
4.1 Wurtzite and Zincblende Crystal Structures	33
4.2 Structural Properties of InN Thin Films Grown on GaAs	36
4.3 Structural Properties of GaN Thin Films Grown on GaAs	43
5. OPTICAL PROPERTIES OF ZINCBLENDE GaN	52
5.1 Cathodoluminescence	52
5.2 Optical Reflectivity and the Refractive Index	59
6. GaAs-GaN SEMICONDUCTOR-INSULATOR DEVICE STRUCTURES	66
6.1 GaN/GaAs Metal-Insulator-Semiconductor Diodes	66
6.2 GaAs/GaN/GaAs Semiconductor-Insulator-Semiconductor Diodes	70
7. X-RAY PHOTOEMISSION SPECTROSCOPY AND VALENCE BAND OFFSETS	79
7.1 Experiment	80
7.2 Zincblende GaN and InN	82
7.3 Wurtzite GaN, AlN and InN	85
7.4 Valence Band Offsets	92
8. DISCUSSIONS AND CONCLUSIONS	104
APPENDIX A. APPROACH OF LAMBRECHT AND SEGALL	106
REFERENCES	107
VITA	112

1. INTRODUCTION

The III-V nitrides have long been viewed as a promising system for semiconductor device applications in the blue and ultraviolet wavelengths. The wurtzite polytypes of GaN, AlN and InN form a continuous alloy system whose direct bandgaps range from 1.9 eV for InN, to 3.4 eV for GaN, to 6.2 eV for AlN. Improved epitaxial crystal growth techniques have led to a rapid improvement in the quality of these materials. The recent demonstration of high efficiency p-n junction light emitting diodes in several laboratories has raised hopes that a GaN laser diode can be fabricated in the near future. However, important interfacial properties of GaN and AlN, such as the heterojunction band offsets, which are critical for laser design, have not yet been reliably measured.

Like many wide bandgap semiconductors, most notably carbon and SiC, the III-V nitrides can crystallize in more than one polytype. The zincblende nitride polytypes have only recently been grown and few of their properties have yet been catalogued. The similarity of the wurtzite and zincblende crystal structures has led some to suggest the zincblende nitride polytypes as a potential alternative wide bandgap semiconductor system for device development. However, until researchers can determine a number of the fundamental physical properties of these materials, their device potential remains, for now, purely speculation.

In this thesis we address some of these outstanding relevant issues in the study and development of the Group III - Nitride semiconductors. Chapter 2 provides a brief background of GaN, AlN and InN. Chapter 3 describes the molecular beam epitaxial crystal growth technique used to grow the GaN, AlN and InN samples studied in this work.

Chapter 4 details the structural properties of zincblende InN and GaN grown on GaAs substrates. In Chapter 5, we analyze the optical properties of zincblende GaN. Chapter 6 describes the insulating properties of zincblende GaN in GaN/GaAs insulator-semiconductor devices structures. Chapter 7 presents x-ray photoemission data dealing with the valence band structure of zincblende GaN and InN and wurtzite GaN, AlN and InN. Estimates are made of the valence band offsets between wurtzite AlN/GaN and AlN/InN. Finally, in Chapter 8, we discuss our results in the context of optical device applications.

2. PROPERTIES OF THE III-V NITRIDES

The III-V nitride semiconductors GaN, AlN and InN are of interest for their potential applications as short wavelength semiconductor optoelectronic devices. This is due to their large direct bandgaps which range continuously, as a function of alloy fraction, from the orange (InN, 1.9 eV) deep into the ultraviolet (AlN, 6.2 eV). Present day semiconductor technology is routinely used for red and yellow light emitters. However, there is as yet no semiconductor technology for blue light, the third primary color. If a high efficiency, low cost blue light emitter can be developed, this technology will allow full color displays to be manufactured much more cheaply and compactly with semiconductor technology. Short wavelength semiconductor lasers are of interest to optical memory designers. By reducing the wavelength of the laser light used for reading and writing, greater bit densities can be realized. A semiconductor ultraviolet photodetector is of great interest to the petroleum and aviation industries who need *in situ* diagnostics at these wavelengths for oil drilling and aircraft engine combustion processes. These devices need not only be sensitive to the ultraviolet spectrum, but must also be stable at high temperatures. The nitrides offer a wider bandgap range, better lattice matched alloys, and improved thermal stability when compared to the Zn based II-VI semiconductors, the other material system commonly considered promising for these applications.

The III-V nitrides received a good deal of attention in the 1970's and many of the fundamental physical properties of the wurtzite polytypes were determined. However, interest waned as many researchers were discouraged by the problems encountered in obtaining high quality material. Specifically, all GaN and InN grown at that time suffered from a high ($\sim 10^{19}/\text{cm}^3$) background electron concentration and researchers were unable to dope either material p-type. Workers were unable to obtain conductive AlN films which limits its usefulness towards optoelectronic applications. All of the nitrides proved to be

highly resistant to wet chemical etching, the standard patterning method of the day. In the past several years, modern crystal growth techniques have begun to produce III-V nitride epilayers of sufficient quality that device development has become feasible. A detailed review describing the history and present day status of the nitride field has been published [1]. Below, we briefly review the fundamental physical properties of GaN, AlN and InN as they are presently understood.

2.1 GaN

GaN is by far the best studied III-V nitride semiconductor due to its potential as a blue and ultraviolet light emitter. GaN normally crystallizes in the wurtzite crystal structure having lattice constants $a = 3.189 \text{ \AA}$ and $c = 5.185 \text{ \AA}$ [2], and occasionally in the zincblende structure [3,4] having a lattice constant $a \sim 4.52 \text{ \AA}$. Maruska and Tietjen [2] measured the lattice constant from 300-900 K and a mean coefficient of thermal expansion of $\Delta a/a = 5.59 \times 10^{-6}/\text{K}$ was observed across the entire range. Values of $\Delta c/c = 3.17 \times 10^{-6}/\text{K}$ and $7.75 \times 10^{-6}/\text{K}$ were approximated for the temperature ranges 300-700 K and 700-900 K, respectively. Sichel and Pankove [5] measured the thermal conductivity of GaN from 25-360 K obtaining a room temperature value of $\kappa = 1.3 \text{ W/cmK}$. The properties of both GaN polytypes are tabulated in Table 2.1.

Table 2.1 Properties of GaN

Wurtzite Polytype

Bandgap Energy	$E_g(300K) = 3.39 \text{ eV}$	$E_g(1.6K) = 3.50 \text{ eV}$
Temperature Coefficient	$\frac{dE_g}{dT} = -6.0 \times 10^{-4} \text{ eV/K}$	
Pressure Coefficient	$\frac{dE_g}{dP} = 4.2 \times 10^{-3} \text{ eV/kbar}$	
Lattice Constants	$a = 3.189 \text{ \AA}$	$c = 5.185 \text{ \AA}$
Thermal Expansion	$\frac{\Delta a}{a} = 5.59 \times 10^{-6}/\text{K}$	$\frac{\Delta c}{c} = 3.17 \times 10^{-6}/\text{K}$
Thermal Conductivity	$\kappa = 1.3 \text{ W/cmK}$	
Index of Refraction	$n(1 \text{ eV}) = 2.33$	$n(3.38 \text{ eV}) = 2.67$
Dielectric Constants	$\epsilon_0 \approx 9$	$\epsilon_\infty = 5.35$

Zincblende Polytype

Bandgap Energy	$E_g(300K) = 3.2 - 3.3 \text{ eV}$
Lattice Constant	$a = 4.52 \text{ \AA}$

Control of the electrical properties remains the foremost obstacle hindering GaN device efforts. Unintentionally doped GaN has in all cases been observed to be n-type, normally in the $n = 10^{17} \text{ cm}^{-3}$ range, with a low value of $n = 4 \times 10^{16} \text{ cm}^{-3}$ [6]. This layer's 300 K and 77 K bulk mobilities of $\mu_n = 600 \text{ cm}^2 \text{ V}^{-1} \text{ s}^{-1}$ and $\mu_n = 1500 \text{ cm}^2 \text{ V}^{-1} \text{ s}^{-1}$ are the highest yet reported. No impurity has been observed in sufficient quantity to account for the background carriers in GaN, so the electrons have been attributed to native defects which are widely thought to be nitrogen vacancies.

One of the long standing problems in GaN research has been the search for a shallow p-type dopant. Most potential dopants have been observed to compensate GaN producing highly resistive material. Only recently has a Mg doping technique which produces p-type GaN and AlGaN been reported [7], [8]. N-type doping has only recently become

important as background electron concentrations continue to fall. Nakamura et al. [9] have successfully doped GaN n-type using Si and Ge. Reproduceable carrier concentrations for GaN:Si ranging from 1×10^{17} - 2×10^{19} cm $^{-3}$ were reported.

Since GaN is primarily of interest as a light emitter, much effort has been devoted to determining its optical properties and a fairly complete account of the optical properties of wurtzite GaN is possible. Maruska and Tiëtjen [2] were the first to accurately measure the 3.39 eV room temperature direct bandgap, and soon after, several excellent studies reported on the low temperature photoluminescence (PL) spectrum of wurtzite GaN [10], [11], [12]. Pankove et al. [10] reported the bandgap temperature coefficient $\frac{dE_g}{dT} = -6.0 \times 10^{-4}$ eV K $^{-1}$. Ejder [13] first measured the GaN refractive index obtaining values of $n = 2.67$ and $n = 2.33$ at and below the bandgap respectively. Matsubara and Takagi [14] measured a dc dielectric constant of $\epsilon_0 = 8.9$.

2.2 AlN

AlN has some outstanding physical properties that have attracted much interest. Its hardness, high thermal conductivity, resistance to high temperature and caustic chemicals makes AlN an attractive material for electronic packaging applications. However, the majority of interest is directed towards the properties of its alloys with GaN which may permit the fabrication of AlGaN based optical devices active well into the ultraviolet. AlN is most commonly observed to crystallize in the wurtzite structure with lattice constants $a = 3.112$ Å and $c = 3.112$ Å [15]. Slack [16] measured the thermal conductivity of AlN to be $\kappa = 2$ W/cmK. Yim and Paff [17] measured the thermal expansion coefficient of AlN obtaining mean values of $\Delta a/a = 4.2 \times 10^{-6}/K$ and $\Delta c/c = 5.3 \times 10^{-6}/K$. In the past several years, both a zincblende and a 6H hexagonal AlN polytype have been synthesized [18]. Zincblende AlN was reported to have a lattice constant $a = 4.38$ Å [19]. Table 2.2 summarizes the known structural and optical properties of the various AlN polytypes.

Table 2.2 Properties of AlN

Wurtzite Polytpe

Bandgap Energy	$E_g(300K) = 6.2 \text{ eV}$	$E_g(5K) = 6.28 \text{ eV}$
Lattice Constants	$a = 3.112 \text{ \AA}$	$c = 4.982 \text{ \AA}$
Thermal Expansion	$\frac{\Delta a}{a} = 4.2 \times 10^{-6}/\text{K}$	$\frac{\Delta c}{c} = 5.3 \times 10^{-6}/\text{K}$
Thermal Conductivity	$\kappa = 2 \text{ W/cmK}$	
Index of Refraction	$n = 2.15 \pm .05$	
Dielectric Constants	$\epsilon_0 = 8.5 \pm 0.2$	$\epsilon_\infty = 4.68 - 4.84$

Zincblende Polytpe

Bandgap Energy	$E_g(300K) = 5.11 \text{ eV (Theory)}$
Lattice Constant	$a = 4.38 \text{ \AA}$

Electrical characterization has been limited to resistivity measurements due to the low carrier concentrations resulting from the deep native defect and impurity energy levels of AlN. High quality bulk AlN typically has a resistivity in the $\rho = 10^{11} - 10^{13} \Omega\text{cm}$ range [20]. Dopant incorporation has not yet produced conductive material. Optical absorption has been used to measure a room temperature direct bandgap value of 6.2 eV [15]. The AlN index of refraction is commonly observed to be $n = 2.15 \pm 0.05$ [21], [22], [23], [24]. The long wavelength dielectric constant of AlN has been measured to be $\epsilon_0 = 8.5 \pm 0.2$ [23], [25], [26], [27]. Two groups have measured the high frequency dielectric constant reporting $\epsilon_\infty = 4.68$ [25] and $\epsilon_\infty = 4.84$ [28].

2.3 InN

InN has not received the attention given to GaN and AlN, partly because it has proved to be the most difficult of the III-V nitrides to grow, and also because it is active in a portion of the electromagnetic spectrum in which alternative semiconductor technology

is available. While suffering from the same problems as the other nitrides, InN also has rather poor thermal stability [29], [30], and no group has yet grown a high quality single crystal film. The wurtzite polytype of InN has lattice constants $a = 3.548 \text{ \AA}$ and $c = 5.760 \text{ \AA}$ [31]. The zincblende polytype has a lattice constant of $a = 4.98 \text{ \AA}$ [32]. Table 2.3 lists the properties of InN.

Table 2.3 Properties of InN

Wurtzite Polytype

Bandgap Energy	$E_g(300K) = 1.89 \text{ eV}$
Temperature Coefficient $\frac{dE_g}{dT} = -1.8 \times 10^{-4} \text{ eV/K}$	
Lattice Constants	$a = 3.548 \text{ \AA}$
Index of Refraction	$n = 2.80 - 3.05$

Zincblende Polytype

Bandgap Energy	$E_g(300K) = 2.2 \text{ eV (Theory)}$
Lattice Constant	$a = 4.98 \text{ \AA}$

InN is generally observed to have a high background electron concentration with the exception of one report [33] of a room temperature electron concentration and mobility of $5 \times 10^{16} \text{ cm}^{-3}$ and $2700 \text{ cm}^2 \text{ V}^{-1} \text{ s}^{-1}$ in a polycrystalline film. That same group reported the room temperature InN direct bandgap value to be 1.89 eV as measured by optical absorption [31]. No experimental investigations of the doping properties of InN have been reported since neither the crystal growth or the background electron concentration has yet been brought under control.

3. MBE CRYSTAL GROWTH OF THE III-V NITRIDES

In this chapter we describe the experimental details of our nitride crystal growth. Section 3.1 overviews the properties of various potential substrates for nitride growth and the reasons behind our choice of GaAs and SiC as substrate materials. Section 3.2 outlines the pre-growth preparation process used for each substrate material including an original procedure developed for SiC substrates. Section 3.3 discusses the epitaxial growth of GaN, AlN and InN on those substrates by the plasma enhanced molecular beam epitaxy (MBE) technique. Particular attention is paid to critical heteroepitaxial growth issues such as initial conditions and buffer layer growth.

3.1 Substrate Selection

One of the major problems hindering nitride research is the difficulty in finding a suitable substrate material that is lattice matched and thermally compatible with GaN. Table 3.1 compares the important structural and thermal properties of various potential substrates with those of GaN and AlN.

Table 3.1 Properties of GaN, AlN and Prospective Substrates

Substrate Material	Lattice Parameters	Thermal Conductivity	Coefficients of Thermal Expansion
GaN	$a = 3.189 \text{ \AA}$ $c = 5.185 \text{ \AA}$	1.3 W/cmK	$5.59 \times 10^{-6}/\text{K}$ $3.17 \times 10^{-6}/\text{K}$
AlN	$a = 3.112 \text{ \AA}$ $c = 4.982 \text{ \AA}$	2.0 W/cmK	$4.2 \times 10^{-6}/\text{K}$ $5.3 \times 10^{-6}/\text{K}$
6H SiC	$a = 3.08 \text{ \AA}$ $c = 15.12 \text{ \AA}$	4.9 W/cmK	$4.2 \times 10^{-6}/\text{K}$ $4.68 \times 10^{-6}/\text{K}$
Sapphire	$a = 4.758 \text{ \AA}$ $c = 12.99 \text{ \AA}$	3.5 W/cmK	$7.5 \times 10^{-6}/\text{K}$ $8.5 \times 10^{-6}/\text{K}$
GaAs	$a = 5.653 \text{ \AA}$	0.5 W/cmK	$6.0 \times 10^{-6}/\text{K}$
Si	$a = 5.430 \text{ \AA}$	1.5 W/cmK	$3.59 \times 10^{-6}/\text{K}$

It is well documented that epitaxial nitride films adopt the symmetry of the substrate material [1]. We chose (001) GaAs for the growth of the zincblende nitride polytypes and (0001)_{Si} 6H SiC for the growth of the wurtzite nitride polytypes. The choice of a GaAs substrate was convenient. Our MBE is a modified GaAs system so the growth of a homoepitaxial GaAs buffer layer was possible. In this way a clean, defect free surface could be prepared for nitride heteroepitaxy. GaAs is by no means a perfect substrate for the zincblende nitrides since the lattice and thermal mismatches are quite large. However, the goal of our zincblende nitride work was to make initial investigations into the physical properties of these unstudied materials, and in the case of InN, to simply verify its existence. 6H SiC is better matched to GaN and AlN which dictated its selection as our hexagonal substrate material. SiC substrates have only recently become commercially available [34] and we expect many researchers in the near future will switch from sapphire to SiC to capitalize on its superior properties as a nitride substrate. The work reported in Chapter 7 is among the first accomplished on SiC.

3.2 Substrate Preparation

Substrate preparation is a crucial step for epitaxial crystal growth. In the case of nitride growth, the preparation is especially important because the growth is heteroepitaxial. Due to the lattice and thermal mismatch, the majority of defects are created at the substrate/nitride interface. A smooth, clean initial growth surface is critical for obtaining optimal epilayer quality.

3.2.1 GaAs Substrate Preparation

In using (100) GaAs substrates, we were able to draw upon many years of experience, both in our own laboratory and from around the world. Several standard GaAs substrate preparation procedures have been developed over the past twenty years. We chose a procedure which has been successfully used in our laboratory for the past ten years.

GaAs substrates were initially degreased by organic solvents to remove hydrocarbons from the surface. Substrates were boiled ($\sim 80^{\circ}\text{C}$) then rinsed in 1-1-1 trichlorethane three times before rinsing in acetone, methanol and finally deionized water (DI). Before etching, metallic impurities were removed from the substrate surface in hot (80°C) H_2SO_4 . Etching is necessary to remove surface material which has been damaged by mechanical polishing by the vendor. Our substrates were etched for several minutes in warm (50°C) $\text{H}_2\text{SO}_4:\text{DI}:\text{H}_2\text{O}_2$ (5:1:1) which removed approximately $100 \mu\text{m}$ of GaAs leaving a volatile protective surface oxide. The etch was terminated by a dip into HCl followed by an extended rinse in DI. Samples were blown dry using filtered N_2 .

For introduction into the vacuum chamber, the GaAs substrates were mounted onto Mo sample holders using In solder. The use of In solder ensured the adherence of the substrate to the Mo holder to temperatures up to 700°C . The In also provides excellent thermal contact leading to good temperature uniformity across the substrate during crystal growth. The substrates were rapidly transported to the vacuum chamber and introduced into the load lock where completely oil free pumps were used to attain ultra high vacuum (UHV).

Once a load lock pressure of 10^{-6} torr was reached, samples were mechanically transferred into the transfer tube (base pressure 10^{-9} torr) which acts as the second vacuum buffer between the MBE system and the ambient. In the transfer tube, samples were outgassed at 200°C on a tantalum heater. Outgassing is necessary to desorb volatile gases from the substrate surface as well as to remelt the In solder allowing trapped gases to escape. After one half hour of outgassing, the transfer tube pressure generally returned to its base value and the substrate and the holder were ready for transfer into the MBE system.

In order to reach the growth temperature, the substrate and holder were heated using a tantalum heater. The temperature was monitored by an optical pyrometer. When the sample temperature reached 500°C, an As flux was supplied at the substrate surface to prevent a depletion of surface As. The GaAs native oxide generally desorbed at ~610°C. The desorption was directly observed by in situ reflection high energy electron diffraction which monitored the conversion of the amorphous oxide to the clean reconstructed (2×4) As-stabilized GaAs surface. Once oxide desorption was complete, the substrate temperature was decreased to 580°C and the GaAs buffer layer growth was commenced.

3.2.2 SiC Substrate Preparation

SiC substrates cannot be prepared in a manner similar to GaAs. This is due to the resistance of SiC to chemical etches and the thermal stability of its oxide. To successfully prepare SiC substrates for nitride heteroepitaxy, a completely new procedure needed to be developed [35].

The (0001)_{Si} face of SiC has only Si dangling bonds in the ideal case (Fig. 3.1). It is quite similar to the (111) Si face, differing though the presence of C atoms in the atomic plane directly below the surface. We therefore expected that (0001)_{Si} would have chemical properties similar to (111) Si and that standard Si preparation procedures [36], [37] could be adapted to SiC. Specifically, we developed a SiC preparation procedure using HF to hydrogen passivate surface Si dangling bonds followed by in situ cleaning of the substrate in a H₂ plasma.

The SiC substrates were degreased in a manner identical to that described above for GaAs. Metallic impurities were removed in a heated (80°C) H₂SO₄:HNO₃ (1:1) solution. A surface oxide was grown in a 60°C HCl:H₂O₂:H₂O (5:3:3) solution and then stripped in a diluted H₂O:HF (10:1) solution. These two steps were repeated several times in order

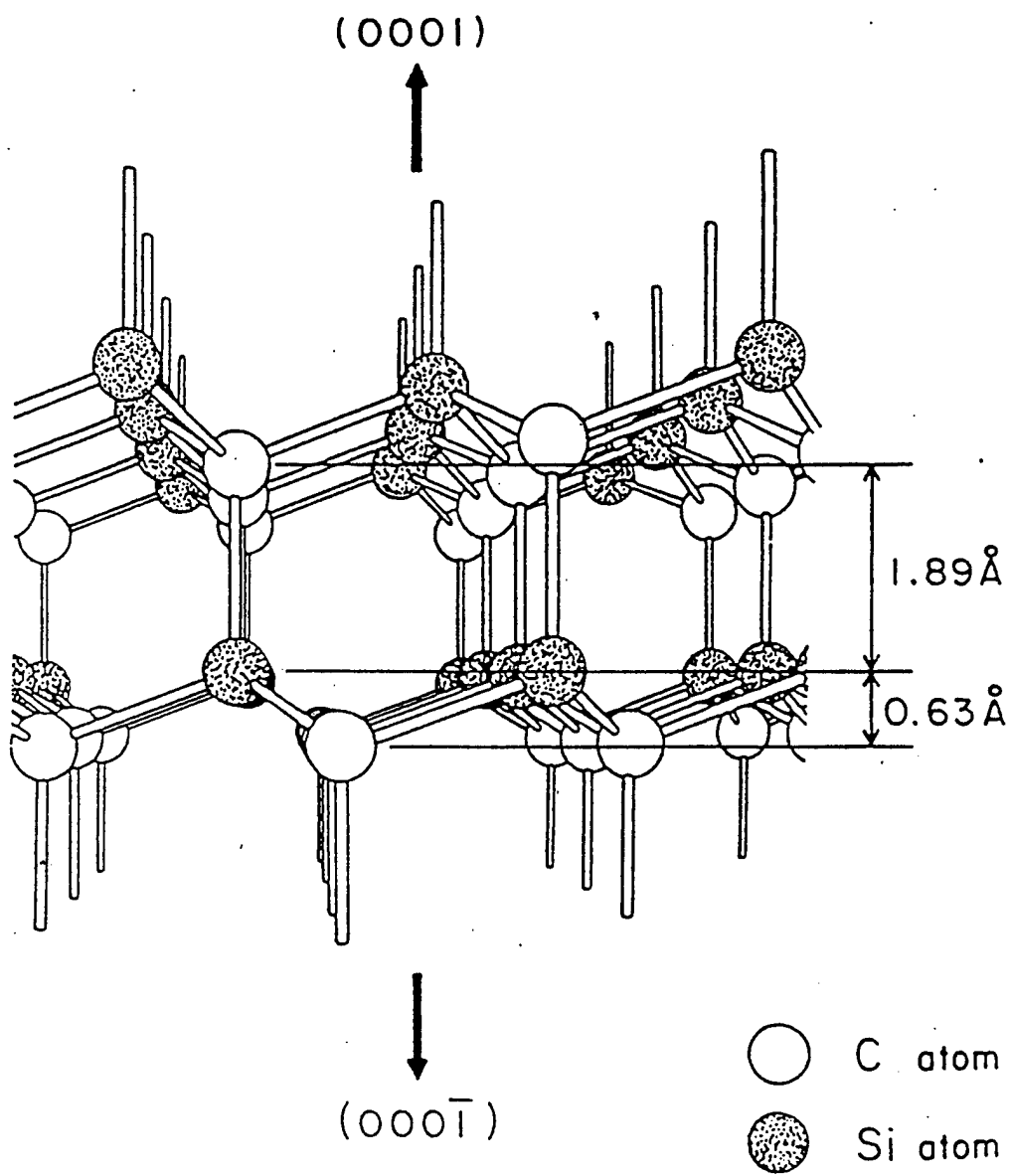


Fig. 3.1. Crystal structure of the $(0001)_{\text{Si}}$ 6H SiC face. Each surface Si atom has a single dangling bond which is passivated by a hydrogen atom.

to remove damaged or contaminated surface material. A final HF dip was performed which was intended to passivate the surface Si dangling bonds with hydrogen in the same manner observed on Si substrates [36]. The substrates were then mounted on Mo blocks with In solder, introduced into the vacuum system, and outgassed. For comparison, some substrates were introduced into the system without the final HF passivation step.

For the H₂ plasma treatment, the substrates were transferred under UHV into a chamber equipped with an electron cyclotron resonance plasma source (see Section 3.3.2) located directly above the sample at a distance of 30 cm. The substrates were then exposed for 90 min in a H₂:He (1:1) plasma at 5×10^{-4} torr at 650°C. Samples were cooled to below 200°C under a H₂ overpressure before transfer so that surface hydrogen would not be thermally desorbed.

To understand the chemistry of our preparation procedure, the SiC substrate surfaces were studied in-situ by x-ray photoemission spectroscopy (XPS) which is a sensitive surface analysis technique. All sample transfers were performed under UHV conditions resulting in undetectable levels of surface contamination. All spectra were taken using Mg K_α x-rays at a 30° photoelectron escape angle. Figure 3.2 compares the Si 2p_{3/2} peaks of two SiC substrates. The spectrum labelled (a) was taken from a SiC substrate loaded into the vacuum after the oxide growth cycle but without the HF passivation. Spectrum (b) corresponds to a sample that received the full preparation including the final HF dip. The high energy tail observed in the unpassivated case corresponds to SiO_x bonds which have binding energies from 0.8 to 4.0 eV above the Si 2p_{3/2} peak depending on the oxidation state [38]. In the HF passivated case, the Si 2p_{3/2} peak is symmetric with no observable tail indicating that the quantity of SiO_x bonds is below the XPS detection limit. After the final H₂ plasma clean no further change in the Si 2p_{3/2} signal was detected. We conclude from our XPS data that the final oxide strip successfully removes all of the oxygen from the

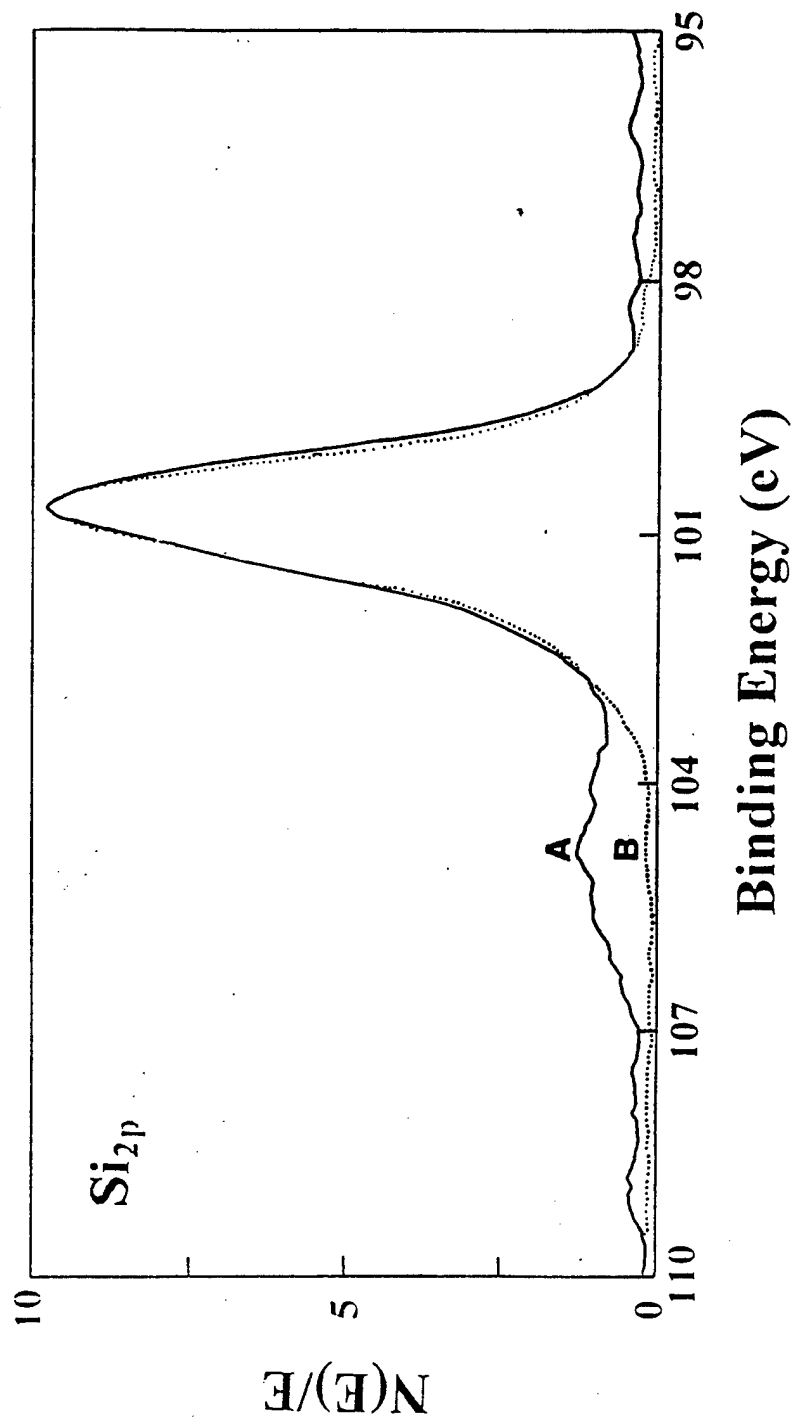


Fig. 3.2. XPS Si 2p_{3/2} peaks of SiC substrates. (a) no HF passivation. (b) HF passivation. The HF passivated surface has no high energy tail resulting from Si_x bonds.

surface Si dangling bonds and the HF dip protects the surface from oxygen contamination by passivating the Si dangling bonds with hydrogen.

However, the C $1s_{1/2}$ spectrum of the HF passivated substrate continued to show a significant high energy tail in which two peaks are resolved (Fig. 3.3, spectrum (a)). The higher energy peak is consistent with surface fluoro carbons resulting from residual F from the HF dip bonding to C. The presence of F was confirmed by observing the F $1s_{1/2}$ signal. The lower energy peak is consistent with the known chemical shift caused by graphitic C bonding which could only occur on a disordered SiC surface. Both peaks rise above a high energy background tail in the C $1s_{1/2}$ signal. This background is evidence of some C-O bonds as well. Since an ideal $(0001)_{Si}$ face has only Si atoms at the surface (Fig. 3.1), C-O bonding can occur only at surface steps, at points of surface disorder, or be caused by some form of subcutaneous oxidation. In order to investigate subcutaneous oxidation, the C $1s_{1/2}$ spectrum was examined at a 60° degree collection angle which is less surface sensitive. The magnitude of the high energy tail decreased markedly compared to the 30° scan from which we conclude that the C-F, C-C and C-O bonding occurs in the top several monolayers.

After H_2 plasma cleaning, the high energy C $1s_{1/2}$ tail was reduced to below the XPS detection limit (Fig. 3.3, spectrum (b)). This indicates that the H_2 plasma was successful in removing surface O and F, and was able to etch the graphitic C. To investigate whether the H_2 plasma treatment preferentially depleted surface Si or C atoms, the integrated peak areas of the Si $2p_{3/2}$ and C $1s_{1/2}$ peaks were compared at large and small angles before and after plasma exposure. No significant change in the relative intensities of the signals was observed indicating that the relative concentration of surface and bulk Si and C remains the same. We conclude that the H_2 plasma does not have the deleterious effect of removing C from Si-C bonds.

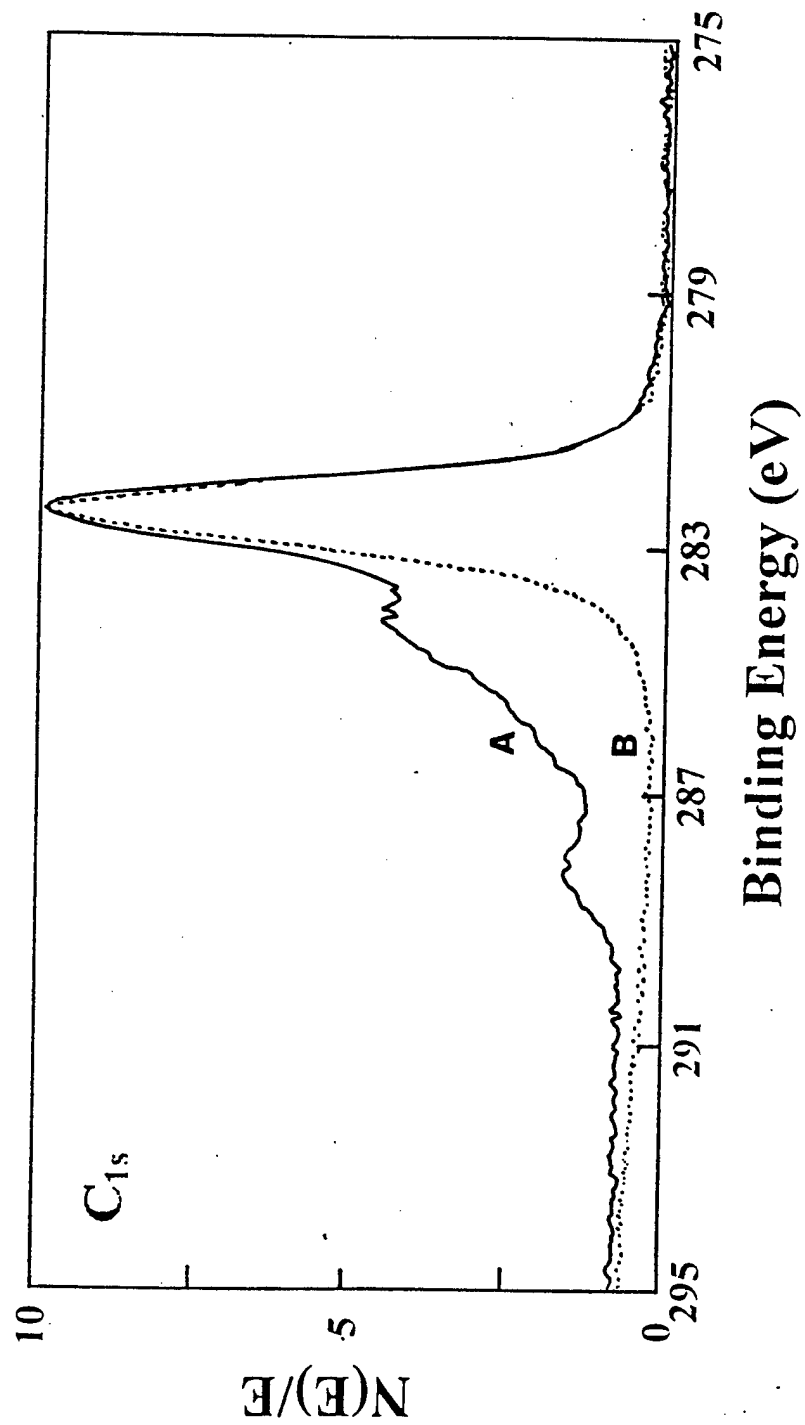


Fig. 3.3. XPS C $1s_{1/2}$ peaks of SiC substrates. (a) HF passivated surface. (b) H_2 plasma treated surface. H_2 plasma treatment reduces the high energy C-O tail to below the XPS detection limit.

3.3 Crystal Growth

The major difficulty in growing nitrides, regardless of the growth method employed, is incorporating stoichiometric quantities of nitrogen into the bulk film. MBE is a very powerful growth technique which has recently been applied to the nitride crystal growth problem [1]. In order to obtain reactive nitrogen species in an MBE growth environment, electron cyclotron resonance (ECR) microwave plasma sources were used.

3.3.1 Overview of MBE

Figure 3.4 is a schematic of the Perkin Elmer 430 MBE which was used to grow the III-V nitride semiconductors. The MBE technique essentially impinges atomic or molecular beams of reactants onto a heated substrate where they react causing the epitaxial growth of a crystal. For the III-V nitrides, solid source Ga, Al and In are used for the group III flux while plasma activated nitrogen provides the group V constituent. The group III fluxes rates are precisely controlled by the Knudsen cell temperature and can be abruptly turned on and off by opening and closing a shutter positioned between the group III oven and the substrate. The MBE crystal growth technique is capable of providing monolayer thickness control and atomically abrupt interfaces.

The substrate temperature is monitored by an optical pyrometer which observes the infrared portion of the substrate blackbody spectrum. The temperature is controlled by an external power supply connected to a resistive tantalum wire heater. The epitaxial surface can be studied *in situ* by reflection high energy electron diffraction (RHEED). All materials introduced into the MBE vacuum are of the highest available cleanliness. The inner portion of the growth chamber is encased within a liquid nitrogen cryoshroud which effectively cryopumps the background gases producing the cleanest growth environment possible.

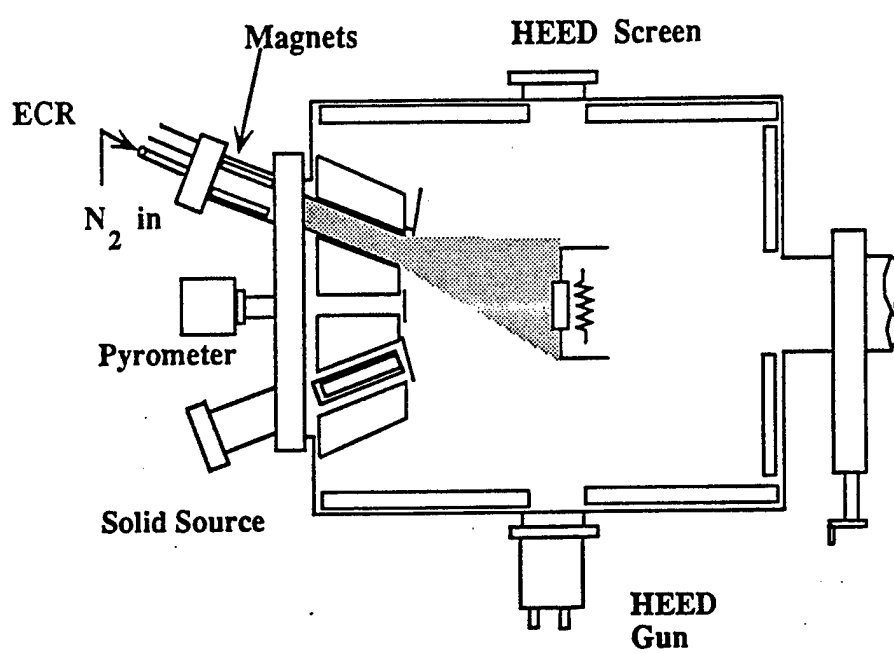


Fig. 3.4. Schematic of plasma enhanced MBE growth chamber using an ECR nitrogen plasma source.

3.3.2 ECR Microwave Plasma Sources

As alluded to in Chapter 2, incorporating stoichiometric quantities of nitrogen into the epitaxial film has been the greatest challenge faced by crystal growers. Early nitride growth efforts typically produced GaN having background electron concentrations in the $10^{19}/\text{cm}^3$ range [2]. The electron background has generally been attributed to nitrogen vacancies. Recent advances in crystal growth technology have allowed improved nitride films to be grown. Vapor phase growth techniques rely on high substrate temperatures ($\sim 1000^\circ\text{C}$) to thermally crack NH_3 molecules [6]. MBE systems typically operate at substrate temperatures in the $600\text{-}700^\circ\text{C}$ range so some other method of nitrogen incorporation must be found.

Plasma excitation of nitrogen or nitrogen containing molecules for III-V nitride growth has been studied for over twenty years [29], [39], [40]. Early workers used rf (13.56 MHz) plasmas which had many disadvantages including high ion energies and unfavorable plasma source geometries. In the past four years, we have seen a revitalization of plasma-based nitride research which has been stimulated by the development and commercial availability of MBE compatible compact ECR microwave plasma sources. For our nitride crystal growth, we used two different commercial ECR designs which performed roughly equivalently. The two source schematics are shown in Figs. 3.5 and 3.6.

These sources operate at 2.45 GHz instead of 13.56 MHz. The shorter wavelength allows the plasma to be lit in the small volume available in an MBE source flange. To better meet the low pressure requirements of MBE, ECR sources introduce a magnetic field designed to match the electron cyclotron frequency to 2.45 GHz. Resonant absorption by the electrons greatly enhances the coupling of the microwave input to the plasma. Each source is compact, allowing it to be inserted into the source flange and through the

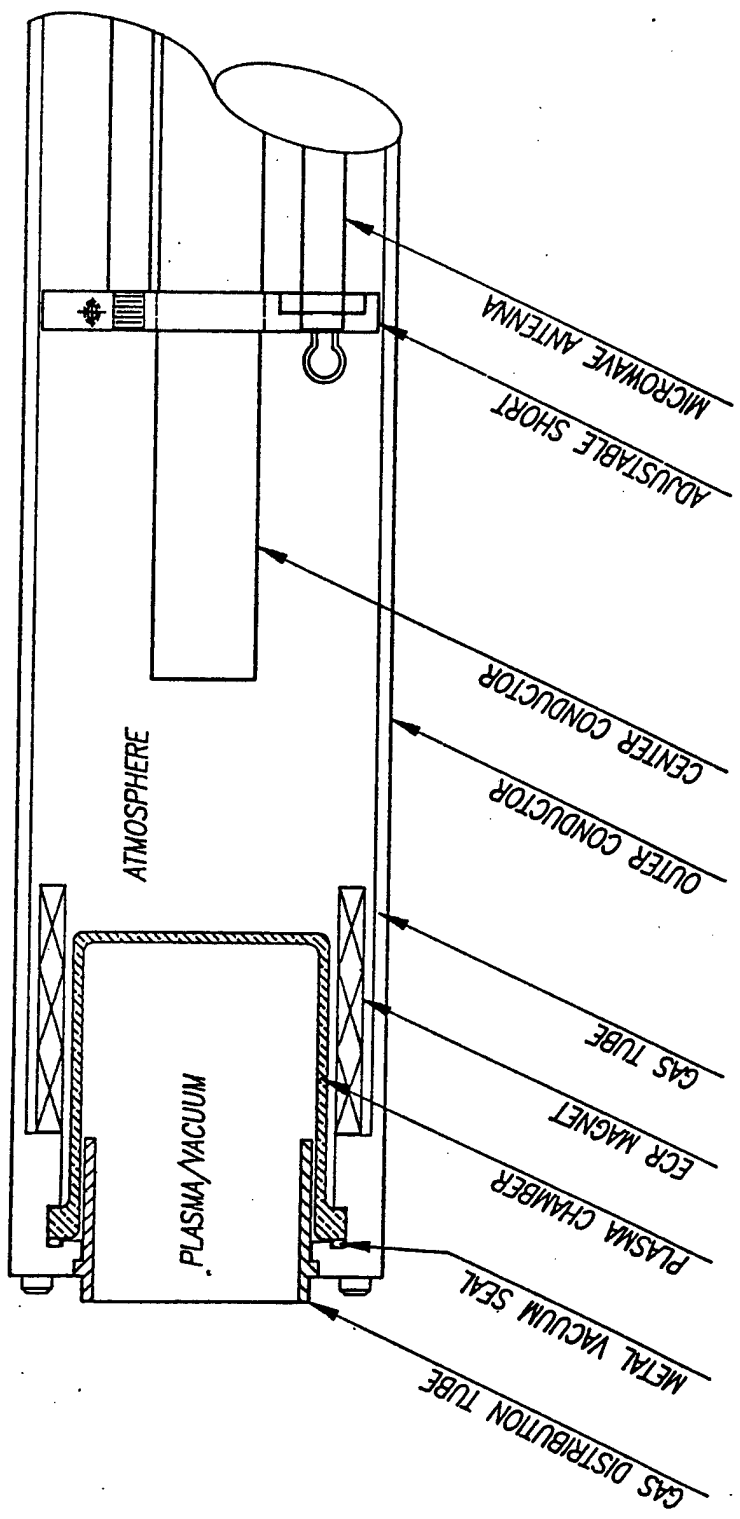


Fig. 3.5. Schematic of a Wavemat MPDR compact plasma source using the coaxial cavity geometry.

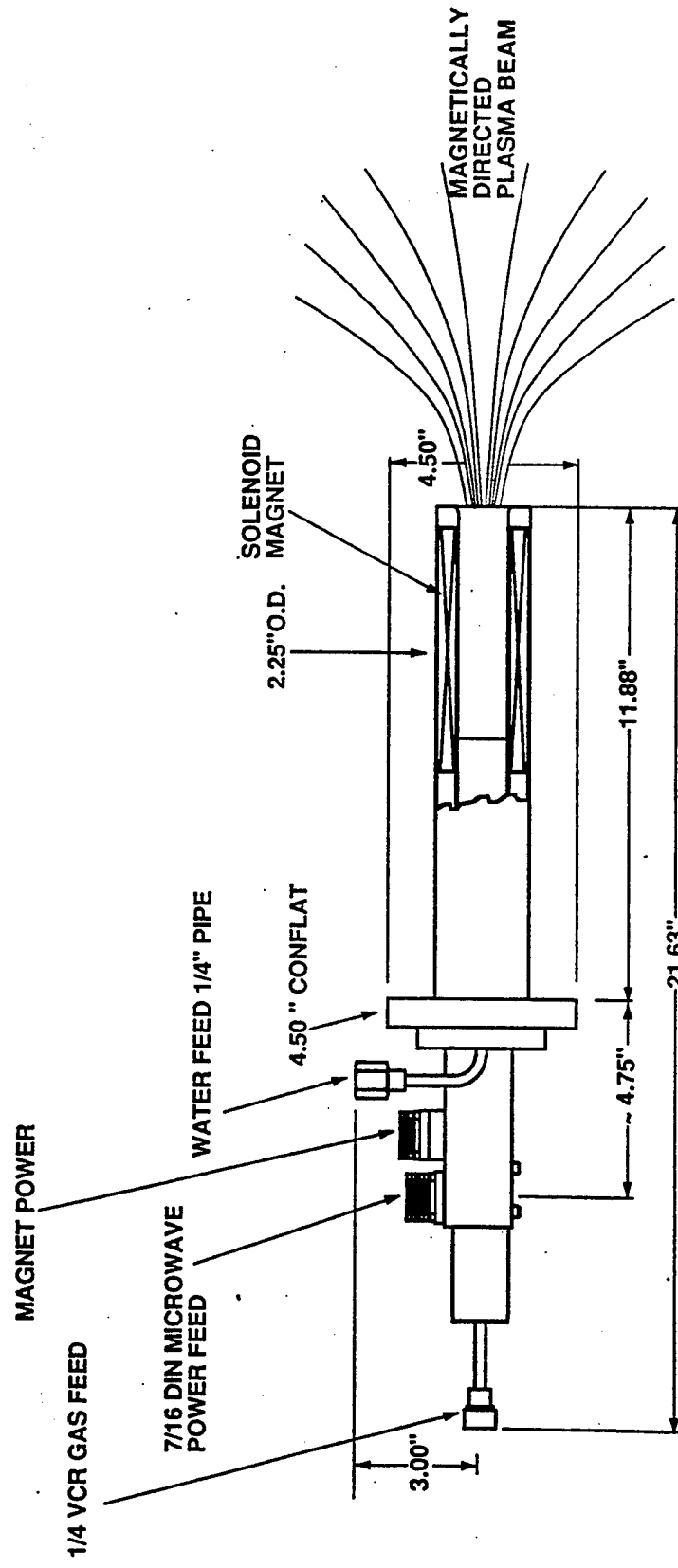


Fig. 3.6. Schematic of an ASTEX CECR compact plasma source using the waveguide geometry.

cryoshroud of an MBE chamber. The plasma enjoys a direct line of sight to the substrate so that collision losses are minimized.

The Wavemat MPDR 610 ECR source (Fig. 3.5) uses a coaxial cavity geometry. The cylindrical cavity region is defined by the outer wall and an inner coaxial short. The remainder of the cavity is defined by the sliding back short, which allows the length of the cavity to be varied for tuning, and by the plasma itself which acts as a lossy conductor. Microwave power is coupled into the cavity by a loop antenna positioned on the sliding back short. Fine tuning is achieved by adjusting the position of the coaxial conductor. Wavemat uses a permanent magnet to provide the magnetic field which creates several ECR surfaces within the plasma. Because a permanent magnet is used, the Wavemat source requires only air cooling.

The ASTEX CECR source (Fig. 3.6) uses a geometry in which microwave energy propagates along a waveguide into the plasma discharge region. The magnetic field is provided by a water cooled electromagnet. Due to the cylindrical symmetry, the electromagnets provide a uniform magnetic field so that the ECR condition exists throughout the entire plasma volume. Tuning is accomplished both by an external matching circuit and by adjusting the magnetic field and gas flow.

ECR sources have been successfully applied towards the MBE growth of all of the III-V nitrides [32], [35], [41], [42], [43], [44], [45], [46]. We have noticed several problems. The largest of these is the tradeoff between growth rate and ion damage. Because of the stringent space restrictions placed on plasma source designers by existing MBE source flange designs, optimal plasma geometries are not possible. To operate at low pressures in non-optimal geometries, high field conditions are introduced leading to the creation of energetic ions which damage the bulk film. When grown at high plasma power (200W),

GaN films are highly defective. This observation is consistent with that of other researchers [47]. To obtain better quality material, we found it necessary to operate at lower power levels at the expense of high growth rates. GaN growth rates in the $0.1 \mu\text{m}/\text{hr}$ range, a tenth of typical vapor phase epitaxy growth rates [6], were used to achieve our best material quality. However, since GaAs is poorly matched to the nitrides, the growth of thick layers is desirable to isolate the epilayer from the deleterious effects of the substrate. Subsequently, a typical GaN growth run require one to several full days to obtain a reasonable film thickness.

3.3.3 Growth on GaAs substrates

Because of the poor thermal and lattice match between the nitrides and GaAs, much care had to be taken during the initial stages of epitaxy. In any heteroepitaxial system, the majority of defects generally are nucleated at the substrate/epilayer interface and at three dimensional islands. Ideally, epitaxy should occur in the form of layer by layer growth on a two dimensional surface. Often the challenge of heteroepitaxy is to obtain uniform surface coverage as quickly as possible so that the crystal growth can become two dimensional. The initial growth conditions are therefore the most critical point of the growth.

In our early efforts, GaN growth was initiated by simply replacing the As flux with the nitrogen plasma stream and reducing the Ga flux to match the availability of nitrogen radicals [44]. Interfaces grown in this manner were studied by RHEED and by transmission electron microscopy (TEM). Figure 3.7 shows the electron diffraction patterns obtained along the [011] and [0 $\bar{1}$ 1] azimuths during GaN heteroepitaxy on GaAs substrates. Figure 3.7 (a) shows the spotty diffraction pattern observed after 27 \AA of GaN heteroepitaxy. The spottiness is indicative of three dimensional island growth. Figure 3.7 (b) was taken after the growth of 100 \AA of GaN. Diffraction lines were visible but diffuse and spotty

indicating that considerable surface roughness remained. It was not until 500 Å of GaN was grown that a smooth GaN growth front was obtained as was evidenced by the sharp (2×2) reconstruction in Figure 3.7 (c).

Electron micrographs of the heterointerface support the RHEED data. Figure 3.8 is a TEM image of the same GaN/GaAs interface. Significant roughening (of the order of 100 Å) of the initially smooth GaAs surface occurred as a result of GaN heteroepitaxy. Large disordered regions are apparent at the interface (arrow 1). Points of maximum interface roughness serve as the nucleation sites of the majority of defects which are seen to propagate into the bulk GaN film (arrow 2). It was therefore determined that a growth initiation procedure which minimized surface roughening and disorder needed to be developed in order to grow the highest quality GaN.

Several different initial growth procedures were monitored by RHEED. We noticed the most significant improvement when the Ga flux was shuttered during the initial stages of growth [48]. Specifically, after the growth of the GaAs buffer layer, the Ga shutter was closed and the Ga cell temperature was adjusted to provide a 0.1 $\mu\text{m}/\text{hr}$ GaN growth rate. In the meantime, N_2 was introduced into the chamber and a plasma was lit. Simultaneously, the As shutter was closed and the ECR and Ga shutters were opened. After an amount of Ga sufficient to grow a single monolayer had been provided, the Ga shutter was closed for an equal amount of time. In this way, we hoped to allow the surface Ga atoms sufficient time to migrate until they found a free N atom with which to bond. We continued to open and close the Ga shutter periodically during the growth of the initial 100 Å of GaN.

Figure 3.9 shows the progression of RHEED patterns which were observed when the above growth initiation was carried out. In Fig. 3.9 (a), diffraction streaks are evident

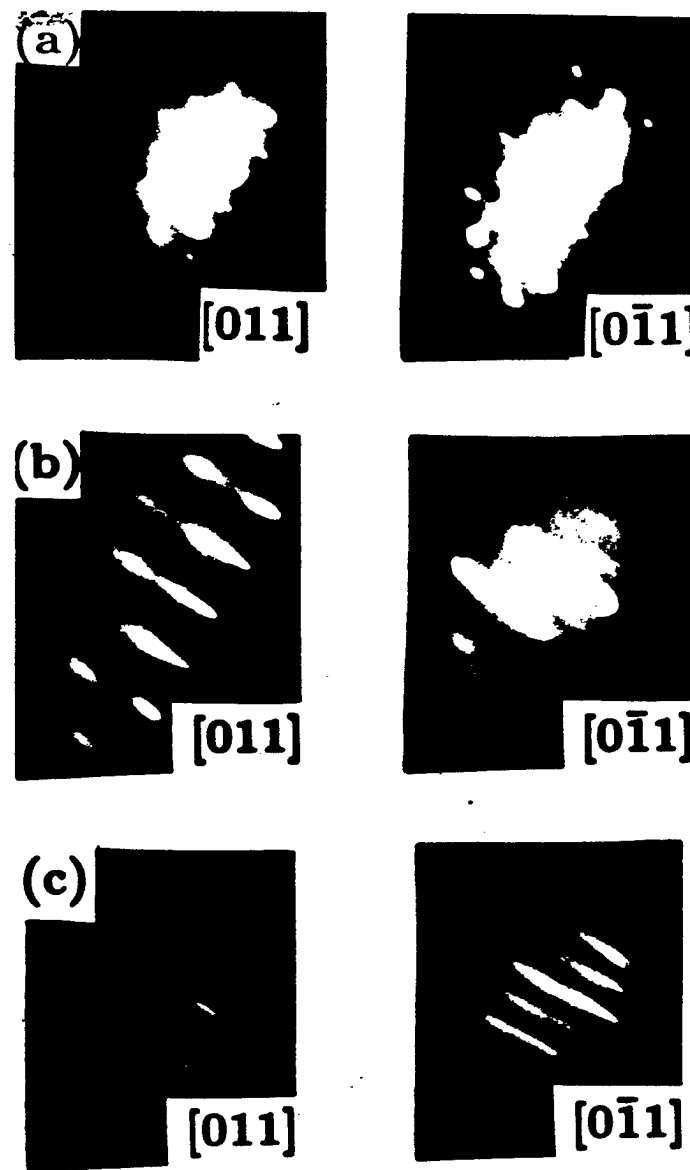


Fig. 3.7. RHEED photographs of GaN/GaAs epitaxy. (a) Spotty surface after 27 Å indicating roughness during initial stages of heteroepitaxy. (b) Diffraction lines become visible after 100 Å of GaN deposition. (c) Sharp (2×2) RHEED after 500 Å of deposition.



Fig. 3.8. Electron micrograph of the GaN/GaAs interface. Numerous twins and stacking faults are apparent. The initially smooth GaAs surface is roughened by the GaN growth. Large disordered regions at the interface (arrow 1) and kinks in the GaAs surface (arrow 2) are the source of most of the defects.

after the deposition of only 14 Å of GaN with the (2×2) reconstruction already beginning to emerge along the [011] azimuth. After 27 Å of GaN growth, the second order diffraction lines are clearly observed (Fig. 3.9 (b)) and after 100 Å of GaN heteroepitaxy we have attained the optimal sharp (2×2) reconstruction (Fig. 3.9 (c)). Once the smooth GaN surface was realized, two dimensional growth could be maintained thereafter under continuous Ga flux.

Electron microscopy confirmed that GaN grown on GaAs using the above initiation procedure had a significantly smoother interface with the GaAs. Figure 3.10 shows TEM images taken on a GaAs/GaN/GaAs heterostructure in which it was possible to grow a continuous 45 Å thick GaN interlayer between GaAs layers. The continuity and quality of the GaN interlayer was verified by the fabrication of semiconductor-insulator-semiconductor diodes [48], [49] which will be described in Chapter 6. Figure 3.11 is a high resolution image highlighting the microstructure of the GaN interlayer. Arrow 1 indicates a region of mild interface roughness above which the GaN is heavily defected. Arrow 2 highlights an atomically abrupt region of the interface above which the GaN is perfect.

We noted earlier that GaAs substrates are not an ideal substrate material for GaN heteroepitaxy due to the large thermal and lattice mismatches. GaN is an extremely hard material as a result of its tight bonding. Early workers noted that 100 μm thick GaN epilayers were capable of cracking their sapphire substrates. Even a relatively thin (3000 Å) GaN epilayer can damage the much thicker GaAs substrates on which they are grown as a result of stress created during the post growth cooling [44].

3.3.4 Growth on SiC Substrates

SiC is a much more ideal substrate material for epitaxial nitride growth due to its excellent thermal and lattice matches with all of the nitrides, AlN in particular. After

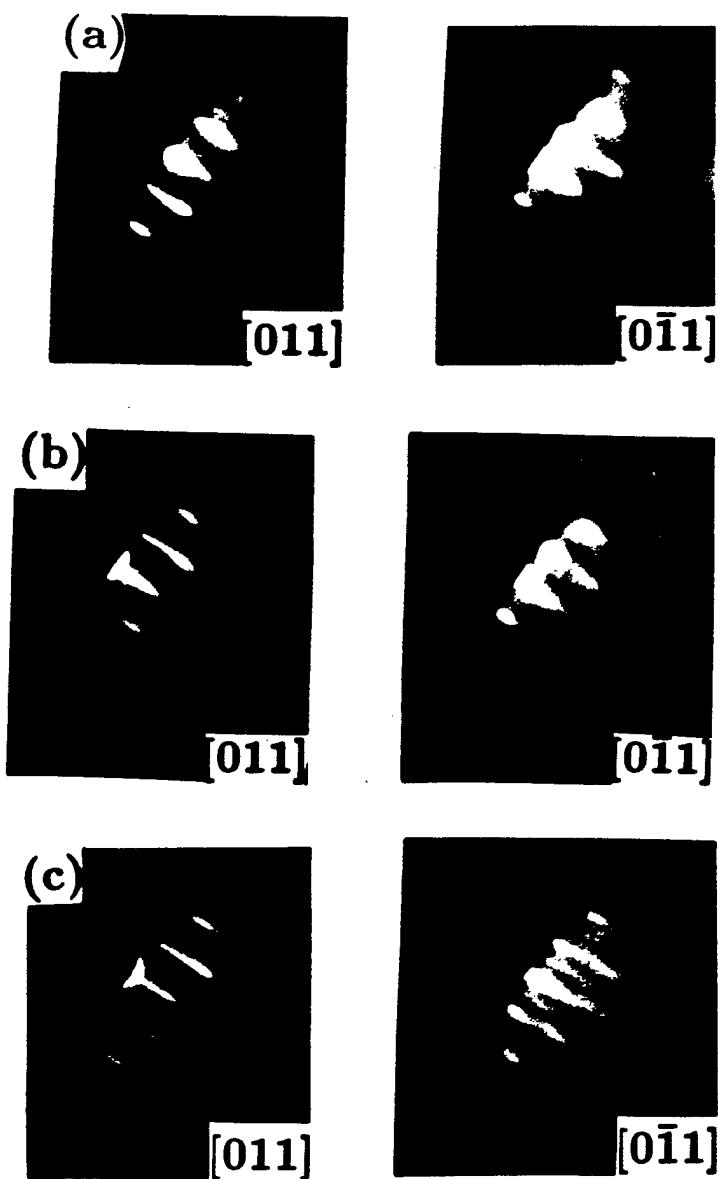


Fig. 3.9. RHEED photographs of GaN/GaAs epitaxy employing shuttered initial Ga flux. (a) Streaks apparent after 14 Å of growth. (b) Second order evident after 27 Å of growth. (c) Sharp (2×2) reconstruction after 100 Å of GaN.

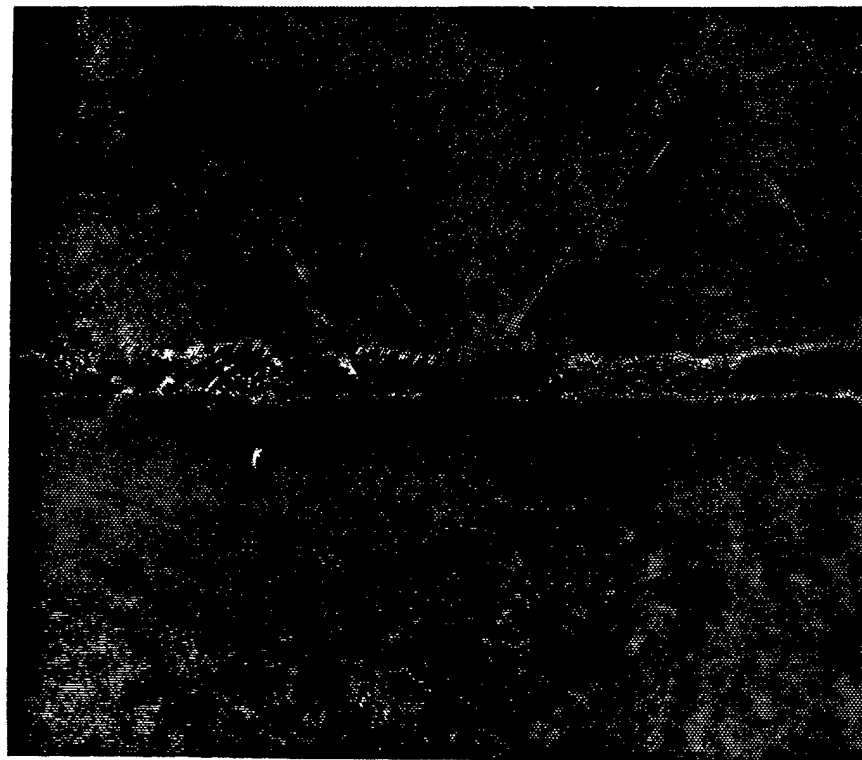


Fig. 3.10. Electron micrograph of a GaAs/GaN/GaAs heterostructure in which the initial Ga flux was shuttered.

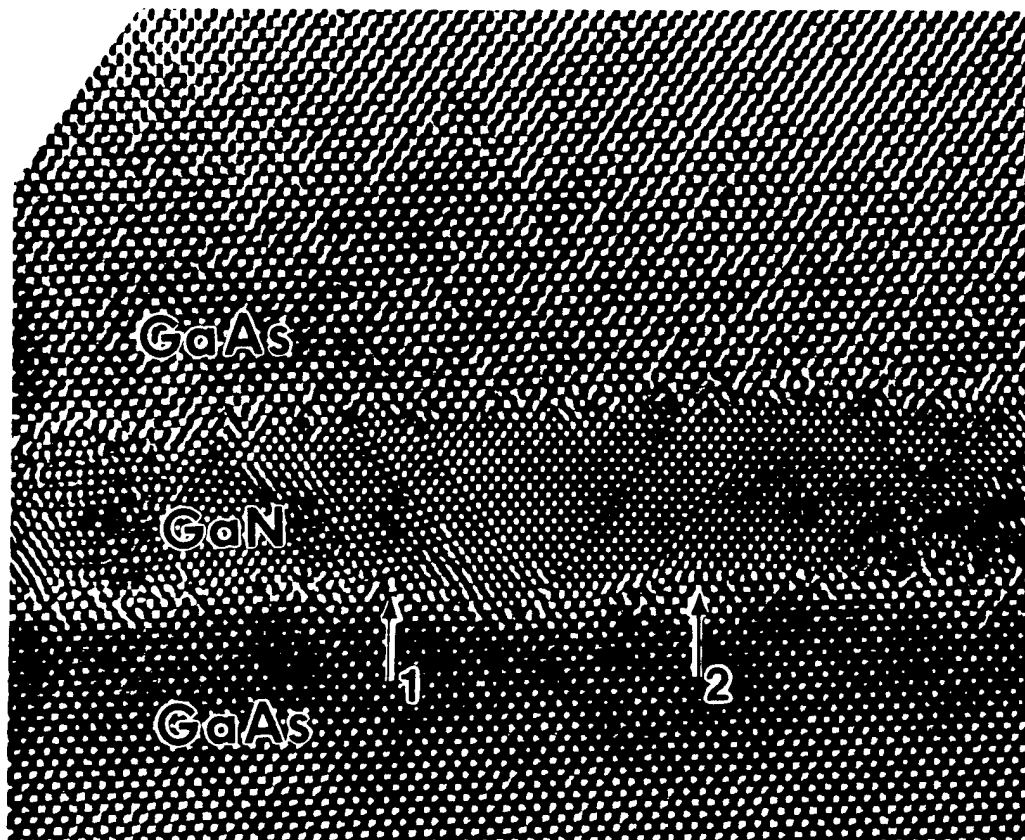


Fig. 3.11. High resolution micrograph of the same structure shown in Fig. 3.10. Arrow 1 indicates a region of interface roughness at which numerous planar defects are nucleated. Arrow 2 points to a smooth region with excellent GaN crystallinity.

performing our preparation procedure, we observed that the initial nitride overgrowth proceeded in a two dimensional manner across a broad range of growth temperatures and rates. The major concern faced in nitride heteroepitaxy on SiC substrates is avoiding the formation of amorphous SiN_x at the interface [50]. This can be avoided by depositing a monolayer of Ga or Al onto the clean $(0001)_{\text{Si}}$ surface before exposure to nitrogen [18]. Photoelectron spectroscopy has been used to determine that Ga, not N, bonds preferentially to surface Si atoms on the $(0001)_{\text{Si}}$ face of SiC [51]. Therefore, by initiating with a group III prelayer, in addition to avoiding the formation of SiN_x , we promote the preferred interface bonding for this system. Since only thin layers were necessary for the photoemission experiments, conservative growth rates of 30 nm/hr were employed. GaN and AlN were grown at a substrate temperature of 680°C. InN was grown at 490°C.

4. THE ZINCBLENDE NITRIDES AND POLYTYPISM

When our investigation of the III-V nitride semiconductors began, researchers had not yet solved many of the problems hindering the development of wurtzite GaN. We decided to investigate the little studied zincblende nitride polytypes with the hopes that the cubic materials were also wide bandgap semiconductors, yet easier materials to dope and process. In this chapter we will briefly review the crystal structures of the various nitride polytypes and then describe the structural properties of InN and GaN thin films grown on (001) GaAs substrates.

4.1 Wurtzite and Zincblende Crystal Structures

The difference between the wurtzite and zincblende crystal structures (Fig. 4.1) lies in the stacking sequence of double layers of group III and N atoms. The wurtzite structure has an ABABAB... stacking sequence along its [001] direction which gives rise to the commonly employed shorthand of 2H for this polytype. The number 2 denotes the periodicity of the stacking while H refers to the overall hexagonal symmetry of the crystal. Similarly, the zincblende structure, with its ABCABC... stacking sequence along the [111] direction is often denoted as 3C, due to its 3 plane periodicity and overall cubic symmetry. A common defect in these crystal structures is the stacking fault, in which the ideal stacking sequence is broken. In both structures, the atoms are tetrahedrally coordinated with almost identical nearest neighbor spacings. In the zincblende structure, one atom's bonds are rotated 60° with respect its neighbors, while in the wurtzite structure there is no rotation between adjacent atoms (Fig 4.2). In other materials which crystallize in both the 2H and 3C polytypes, such as SiC, the similarity in atomic environment leads to similar overall properties although their bandgaps differ by 1.1 eV. In the case of the nitrides, existing theoretical work predicted that the zincblende GaN [52], [53] and InN [54] polytypes would have direct bandgaps roughly equal to those of the wurtzite polytypes.

Nitride Polytypes

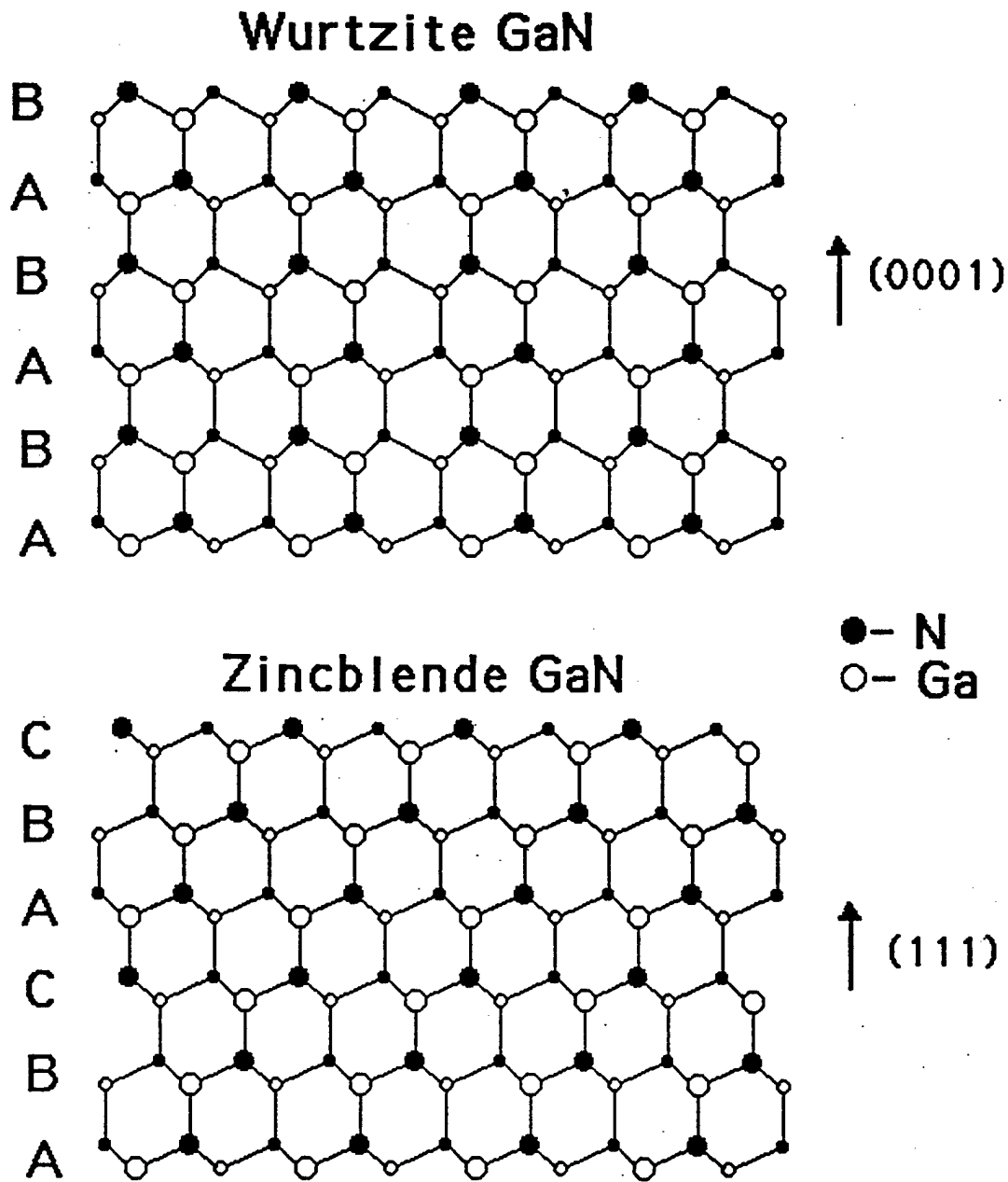


Fig. 4.1. Crystal structure of two most common nitride polytypes. Wurtzite (top) has the hcp unit cell with an ABABAB... stacking sequence normal to its (0001) face. Zincblende (bottom) has an fcc unit cell with an ABCABC... stacking sequence normal to its (111) face.

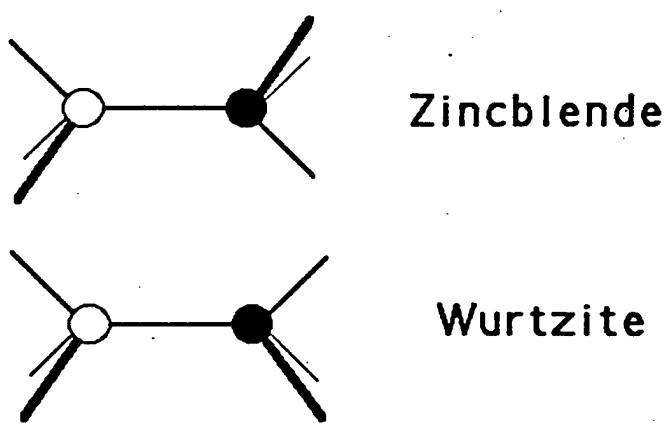


Fig. 4.2. The local environment of atoms in the two crystal structures differs by a 60° rotation of adjacent tetrahedral bonds in the zincblende case.

4.2 Structural Properties of InN Thin Films Grown on GaAs

Figure 4.3 is a low resolution transmission electron micrograph (TEM) taken at the GaAs substrate - InN epilayer interface in the cross sectional geometry. Selected area diffraction patterns identified the presence of an unintentionally grown InAs interlayer, roughly 80 nm thick, between the GaAs substrate and the InN epilayer. The As background pressure in the chamber was insufficient to account for the growth of such a thick InAs layer. We surmise that As was drawn from the GaAs substrate to react with impinging In atoms on the surface. An inclusion of InAs into the GaAs substrate is clearly visible in Fig. 4.3 which lends weight to the supposition of a solid phase reaction with the substrate. The InN film is highly disordered with a large number of stacking faults running along the $\langle 111 \rangle$ planes.

Figure 4.4 shows a high resolution lattice image of the InN film which reveals the coexistence of both 2H and 3C InN polytypes. This is the first observation of zincblende InN in nature. In some regions, pure zincblende InN is obtained, whereas adjacent areas are wurtzite. The zincblende InN is oriented epitaxially to the GaAs substrate while the c axis of the wurtzite InN is normal to the zincblende (111) plane. In other words, the stacking direction of both polytypes are parallel and the domains are bounded by a stacking fault. In other more heavily faulted regions (Fig. 4.5), it becomes impossible to identify either phase because there is no long range stacking order.

Figure 4.6 shows two types of stacking faults. The fault in Fig. 4.6 (top) introduces dislocations at the termination of the atomic plane and therefore acts as a form of strain relief. Figure 4.6 (bottom) illustrates a stacking fault which introduces no dislocations. Such a stacking fault can occur if the epitaxial material is grown on zincblende (111) or wurtzite (0001) surfaces so that growth occurs in a plane by plane manner in the stacking

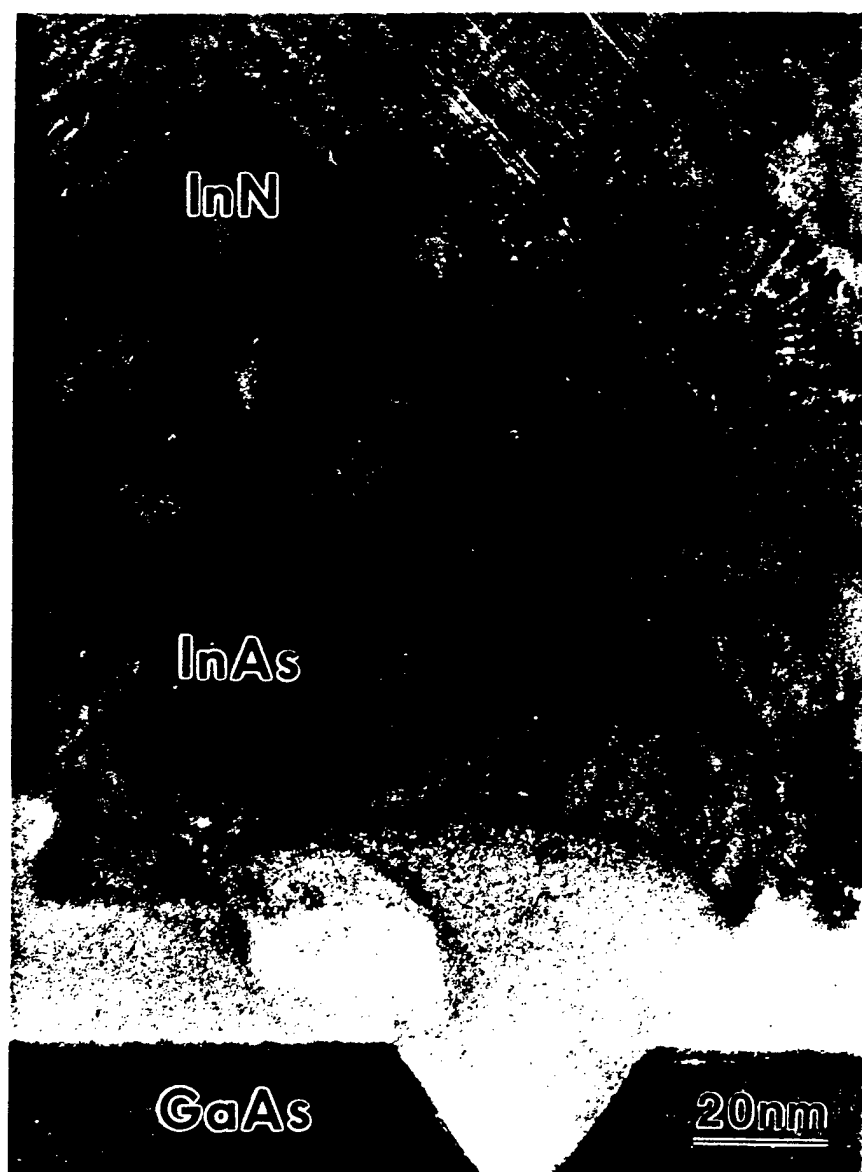


Fig. 4.3. Low resolution TEM micrograph of an InN epilayer interface with the GaAs substrate. An unintentionally deposited InAs interlayer (~ 80 nm) is present between the GaAs substrate and the InN film. A high density of stacking faults appears along both $\langle 111 \rangle$ planes of the InN.

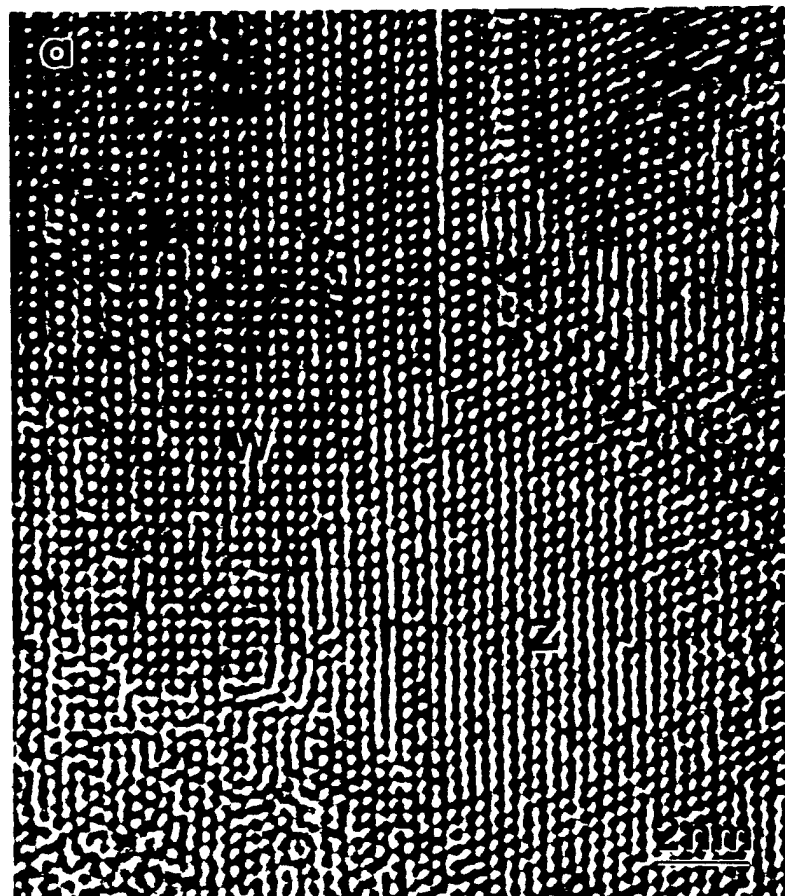


Fig. 4.4. High resolution TEM micrograph of the InN film showing the boundary between wurtzite (upper left) and zincblende (lower right) domains. The boundary runs normal to the stacking direction of both crystals.

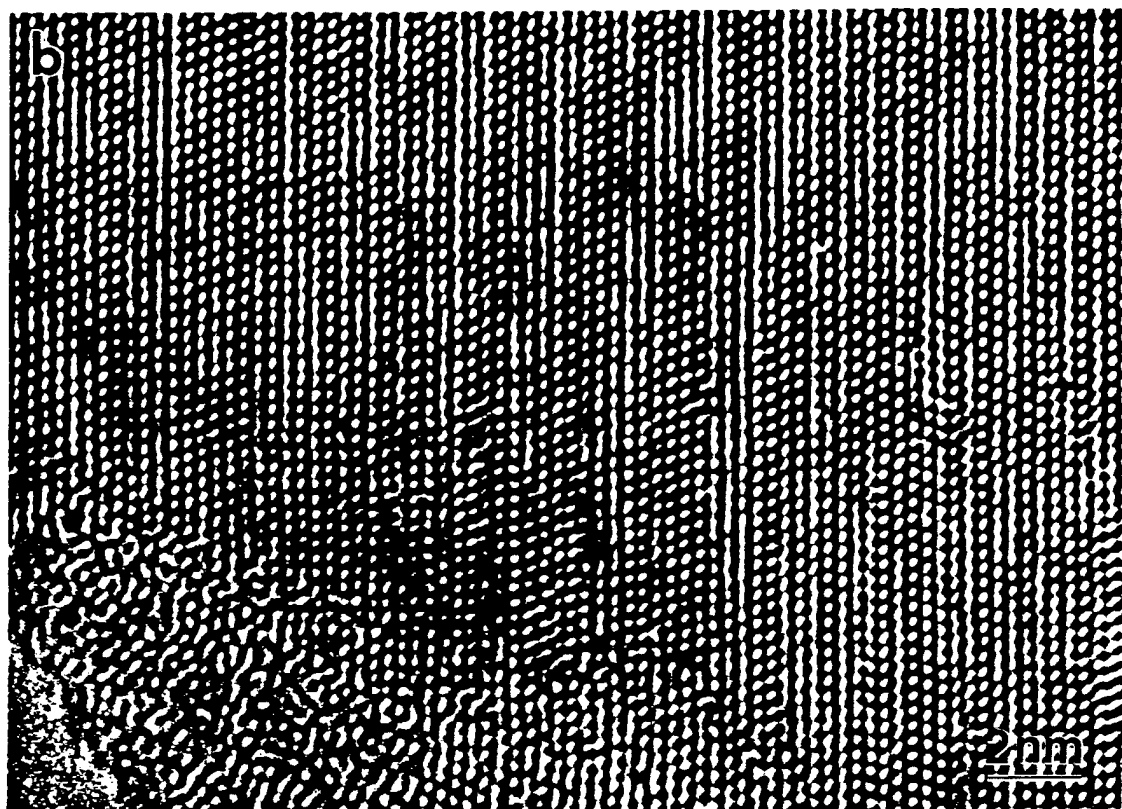


Fig. 4.5. High resolution TEM micrograph of the InN film showing heavily faulted material having no long range stacking order.

Stacking Fault Defect

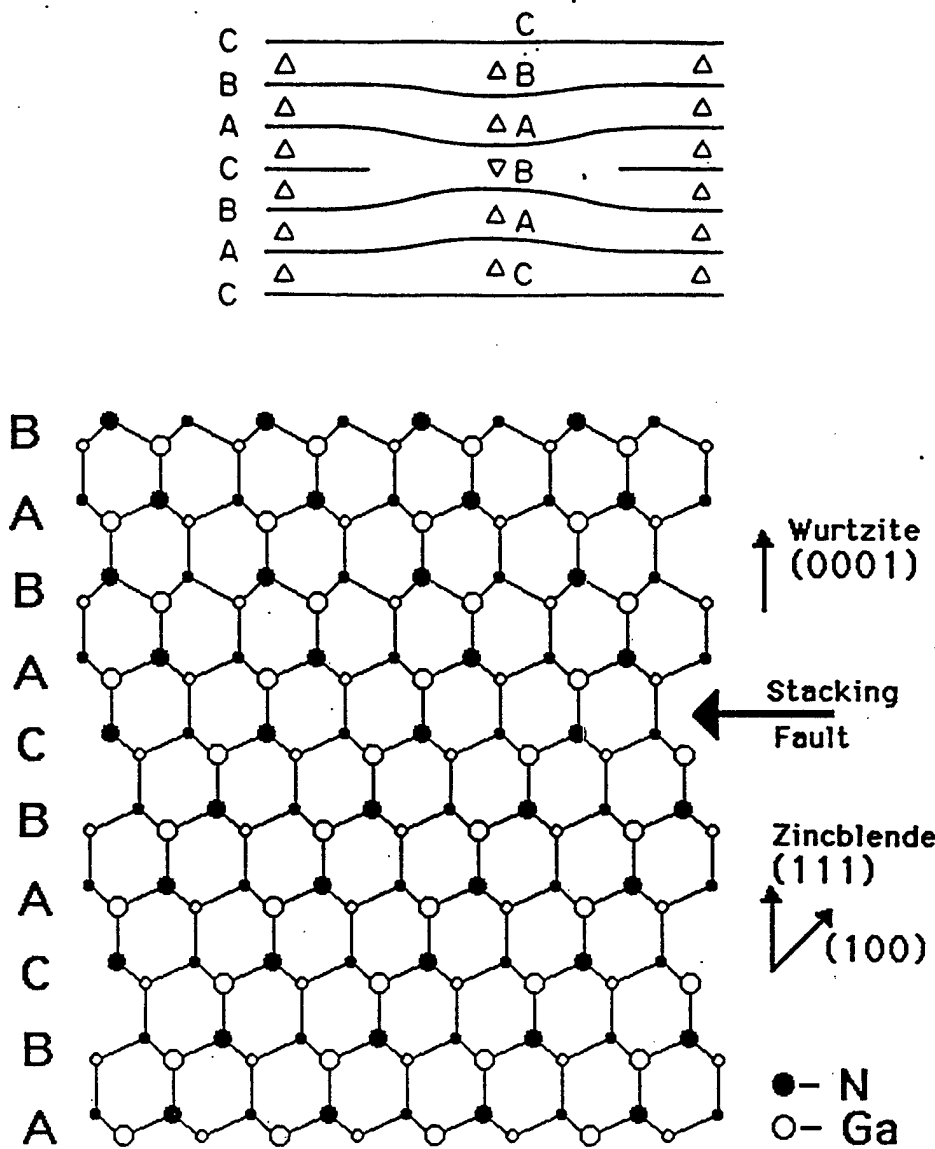


Fig. 4.6. Schematic of two types of stacking fault defects. For growth not along the stacking direction, stacking faults require the termination of an atomic plane (top) at a dislocation. Along the stacking direction (top), the sequence can change without dislocations creating a coherent heterojunction. Polytype conversion requires a 60° rotation of the crystal above the stacking fault to accommodate the wurtzite bonding sequence (see Fig. 4.2).

direction. SiC researchers have been aware of this possibility for a coherent interface for some time and the same idea may be used for the III-V nitrides in the future. If the bandgaps of the two polytypes are different, the resulting interface will be a heterojunction, yet an isoelectronic one in which troublesome autodoping and interface charge effects are non-existent.

To understand the mechanisms governing the growth of InN thin films on (001) zincblende substrates, one must consider both the relative formation energies of the two InN polytypes and the lattice mismatch between InN and GaAs (or InAs, in this specific case). We believe that the zincblende InN polytype is metastable and that the wurtzite phase has a significantly lower formation energy. We base this supposition on the fact that all polycrystalline InN thin films grown previously on a wide variety of substrates have exhibited only wurtzite structure. It is therefore the zincblende template provided by the (001) substrate which is responsible for the epitaxial growth of the 3C InN. Due to the high level of lattice mismatch present, dislocations are expected to form immediately (during the first monolayer of growth) in the epitaxial InN. We believe that these dislocations serve as nucleation sites for stacking faults. The dislocation/stacking fault mechanism not only lowers the total energy by relieving strain, but it allows wurtzite InN domains to be formed which have a lower bulk energy than the metastable zincblende InN polytype.

A conventional $\theta - 2\theta$ x-ray diffraction measurement was used to accurately determine the lattice constant of zincblende InN (Fig. 4.7). Both the (200) ($2\theta = 36.037^\circ$) and the (400) ($2\theta = 76.520^\circ$) zincblende InN peaks were observed alongside the corresponding substrate peaks which confirms the zincblende material to be epitaxial to the substrate. To determine the lattice constant and the experimental error, the GaAs (200) K_α and the GaAs (400) K_{α_1} and K_{α_2} peaks were used as a standard to correct for instrumental shift and broadening. From the (200) and (400) InN peaks, the zincblende InN lattice

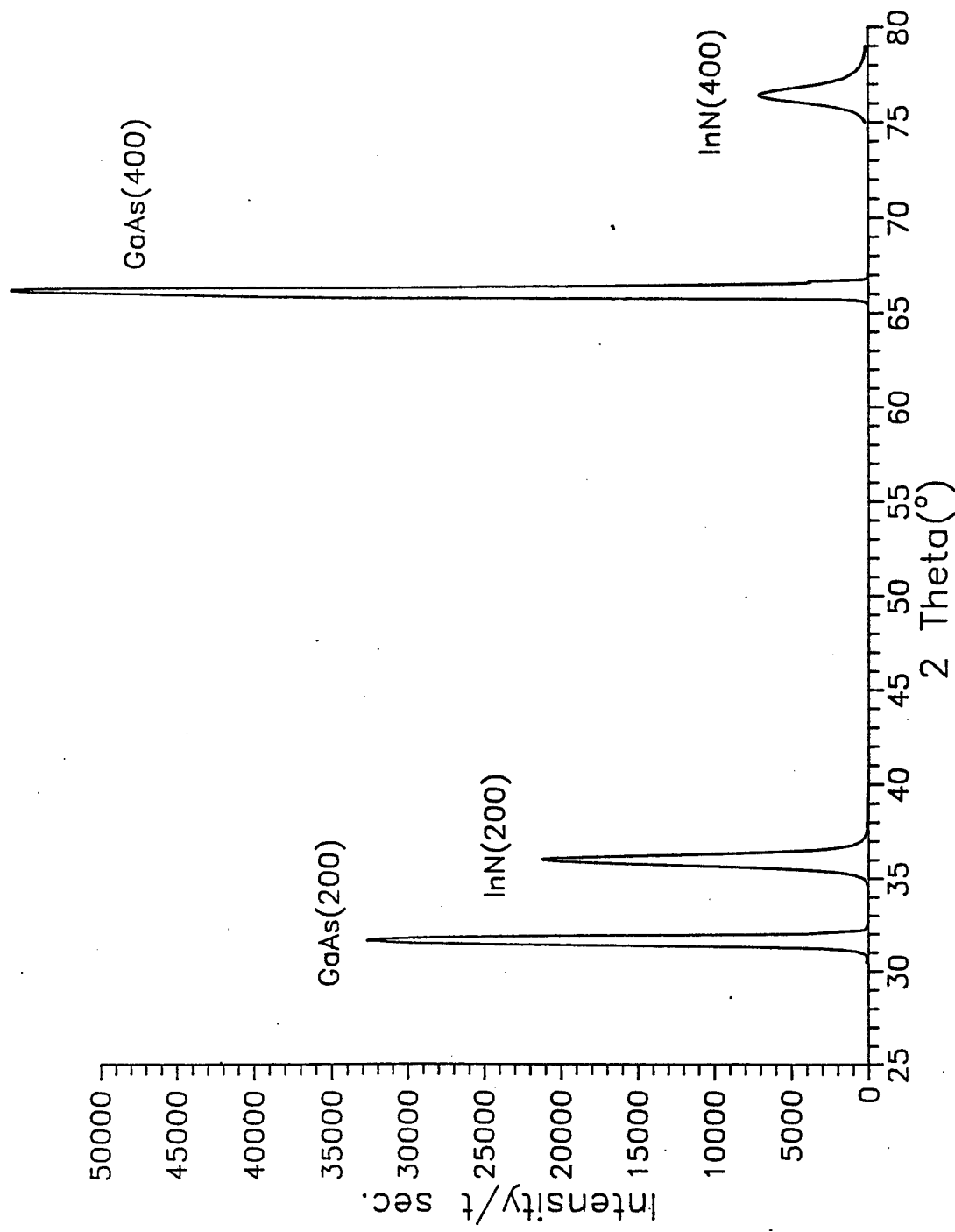


Fig. 4.7. θ - 2θ x-ray scan of the InN/GaAs layer showing the (200) and (400) peaks of the epitaxial InN material and the GaAs substrate.

constant was determined to be $a = 0.498 \pm .001$ nm. Measurements of high resolution TEM micrographs and selected area diffraction patterns, while intrinsically less accurate, gave a value of $0.495 \pm .005$ nm. A rocking curve taken of the (200) InN peak had a full width at half maximum of 3° after instrumental width correction which is quite large and is in accordance with the poor overall film quality and small domain sizes observed by HRTEM (Fig. 4.8).

Notice that the $\theta - 2\theta$ x-ray scan does not detect the presence of the wurtzite InN since no wurtzite planes satisfy the Bragg condition in this geometry. Following the work of Lei et al. [45], [46] who used triple axis x-ray diffractometry to observe zincblende domains in bulk wurtzite GaN, we measured the wurtzite phase by rotating the sample to $2\theta = 51.60^\circ$ and $\chi \approx 65^\circ$ aligned to the (110) peak of the wurtzite domains observed by TEM. This orientation is revealing because it is normal to the stacking direction of both polytype domains, i.e. [001] for wurtzite, [111] for zincblende. When rotating around the (110) axis (ϕ axis in our geometry) the ABABAB stacking of the wurtzite polytype is expected to produce the four equally spaced peaks corresponding to the four $\langle 110 \rangle$ planes. This was indeed experimentally observed (Fig. 4.9) which confirms the crystallographic relationship of the 2H and 3C InN domains observed by TEM, and reinforces the notion of stacking faults as the nucleation mechanism of the wurtzite domains. The lattice constants of the wurtzite polytype were calculated to be $a = 0.36 \pm .01$ nm from the (110) peak and $c = 0.574 \pm .001$ nm from the (002) peak which are in good agreement with previous work [31].

4.3 Structural Properties of GaN Thin Films Grown on GaAs

A similar study was performed on GaN thin films grown on (001) GaAs substrates. Our samples represent the first structural analysis of zincblende GaN following the initial

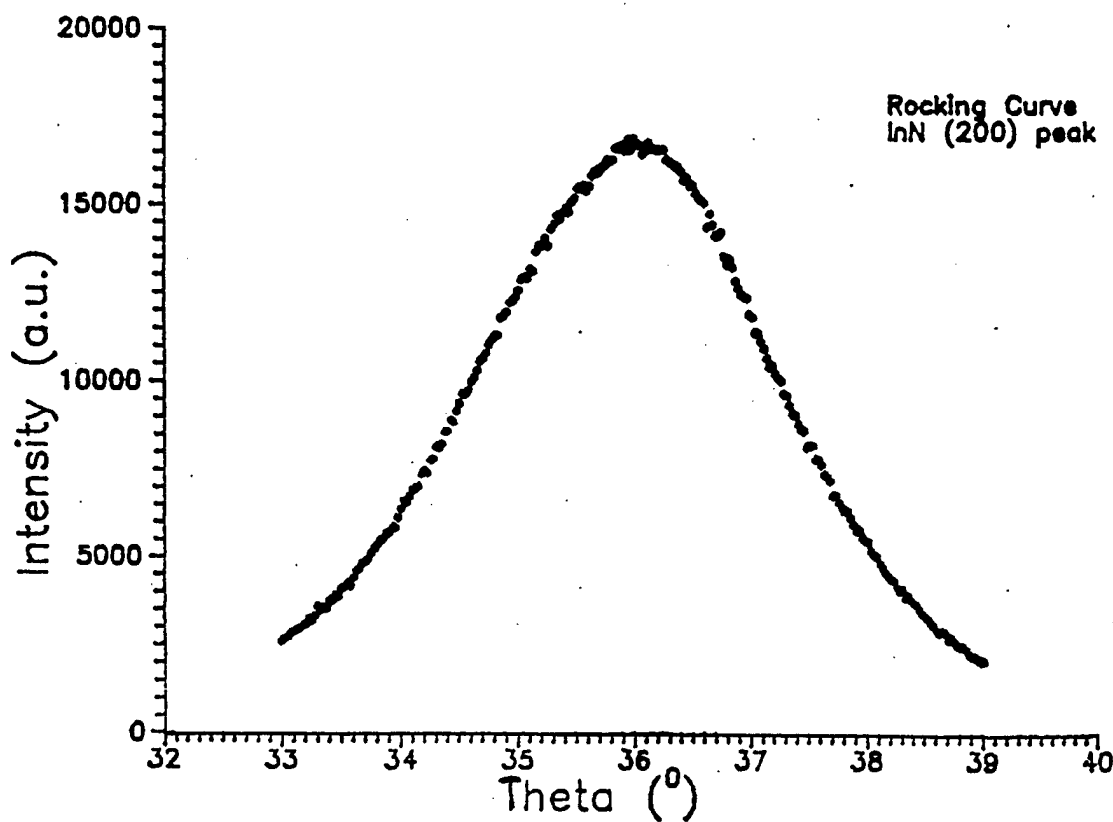


Fig. 4.8. Rocking curve of the InN (200) peak having a broad 3° FWHM resulting from the small zincblende domain size and large amounts of residual strain.

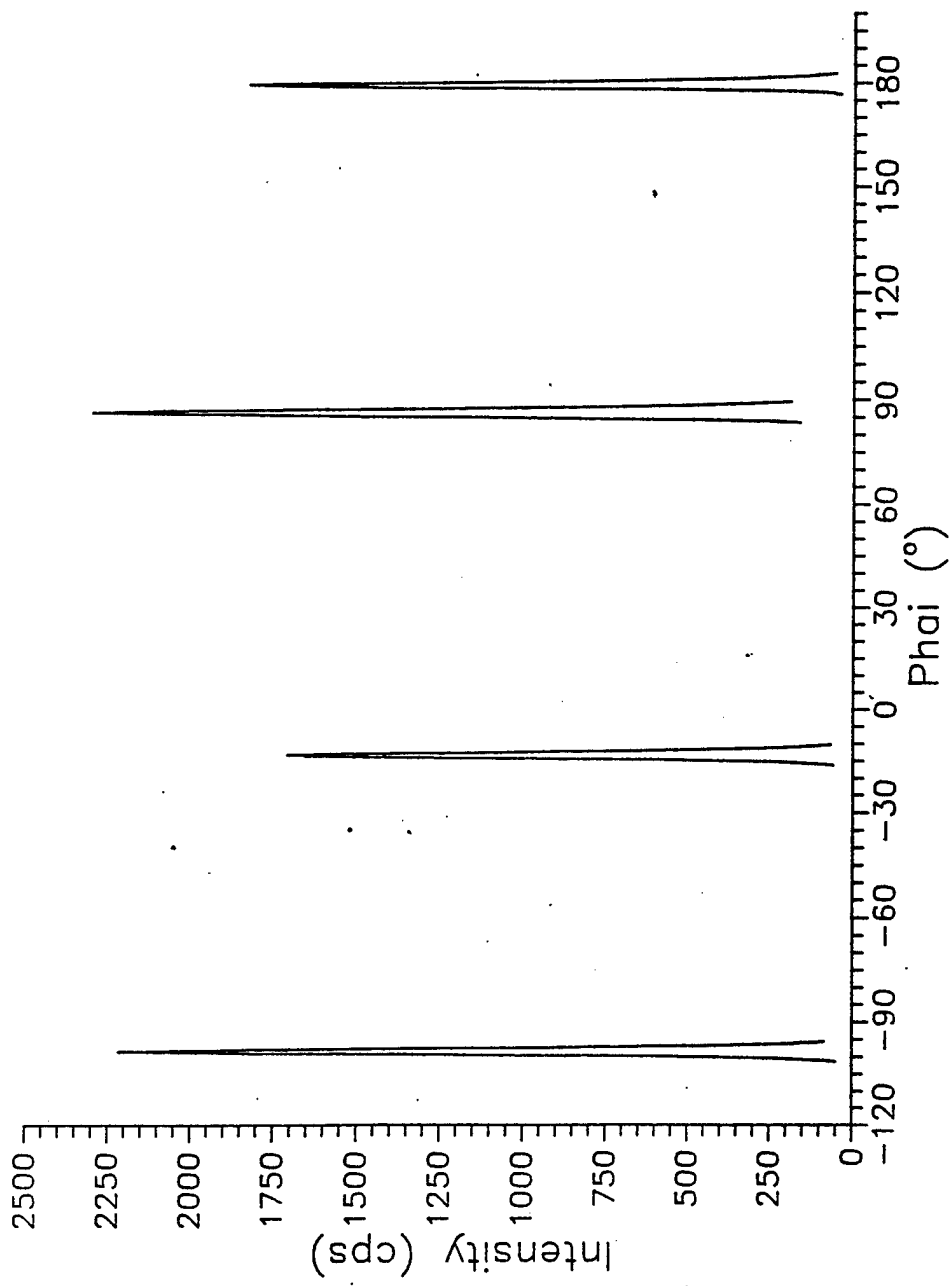


Fig. 4.9. X-ray scan around the (110) wurtzite axis reveals the four $\langle 110 \rangle$ peaks at roughly 90° intervals confirming the stacking sequence of the (0001) wurtzite planes to be normal to the stacking fault direction.

work of Mizuta et al. [4] who estimated the lattice constants of zincblende GaN, also grown on (001) GaAs. Figure 3.8 is a TEM micrograph showing the GaN/GaAs interface. As was the case for InN films, numerous stacking faults are evident in the GaN epilayer. However, high resolution TEM found no evidence of large wurtzite domains in the several zincblende GaN samples studied. TEM is a highly selective technique with which it is only possible to view a tiny volume of the total film, so it is not possible to state categorically from the TEM evidence that wurtzite domains do not exist in our zincblende GaN films. However, we can say that if wurtzite domains are present, they exist in significantly less quantity in these GaN films.

A $\theta - 2\theta$ x-ray diffraction measurement was used to determine the lattice constant of zincblende GaN. Figure 4.10 shows the (200) GaN peak which was observed at $2\theta = 40.10^\circ$ from which the lattice constant of $a = 0.454 \pm .002$ nm was calculated in a manner identical to that used for InN. The width of the rocking curve was 96 min. (Fig. 4.11) which, while significantly less than the InN value, is still quite high. We attribute this to the high defect density stemming from the large lattice mismatch and the relative thinness of our films (~ 200 nm) which causes a larger fraction of the total GaN volume to be disturbed by the presence of the mismatched GaAs substrate. When the sample was rotated in the x-ray diffractometer to the correct coordinates, (011) wurtzite peaks were observed at 90° intervals (Fig. 4.12) indicating the presence of a wurtzite component in the bulk zincblende GaN film.

Based on our TEM results, we believe that the wurtzitic component in our films exists as small domains near some of the numerous stacking faults, and not in larger polytype domains as was the case for our InN films. The GaN was grown on the (001) GaAs face, and based on the excellent RHEED (Fig. 3.9), we can assume that the growth proceeded in a layer by layer mode in that direction. A stacking fault, defining a polytype domain

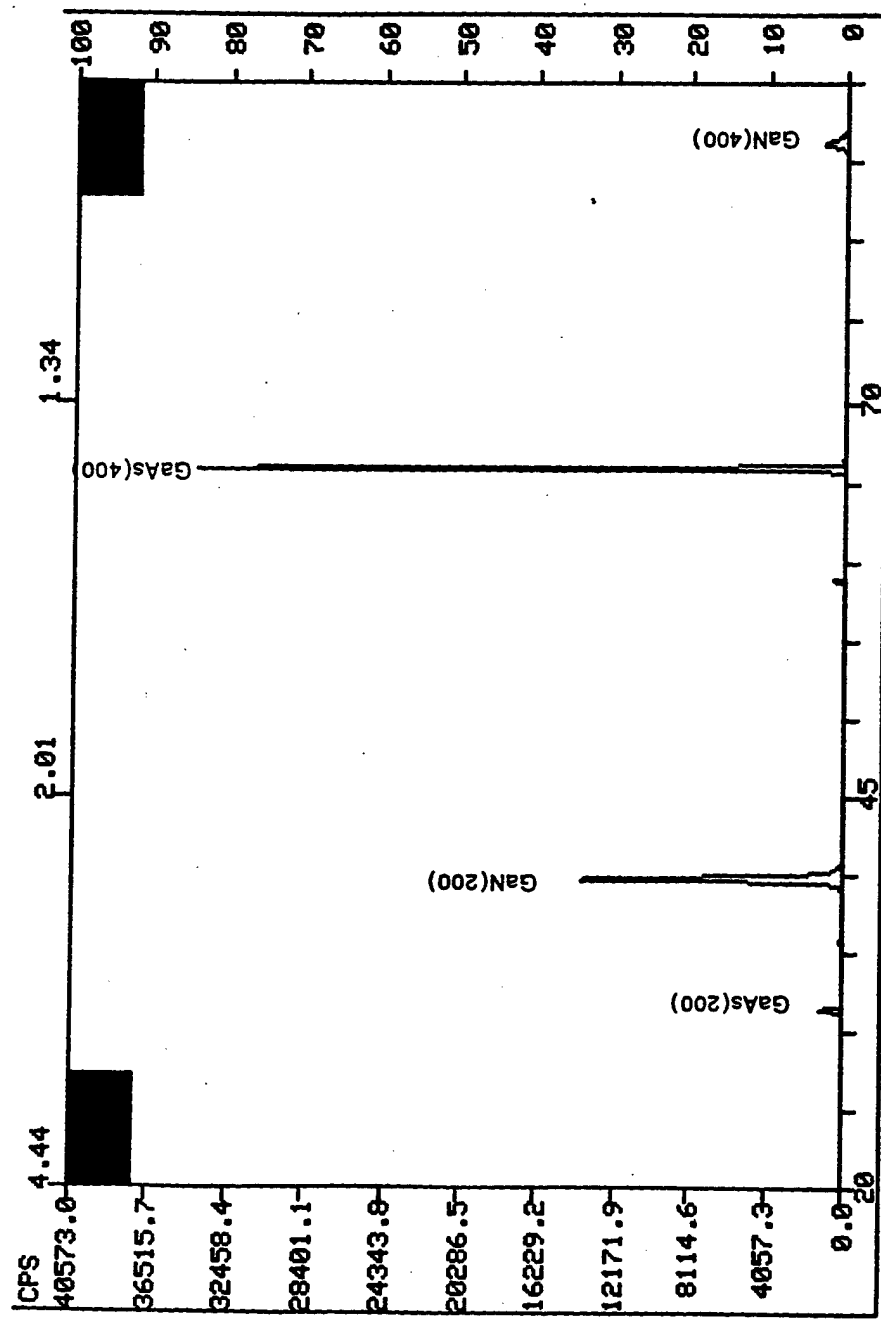


Fig. 4.10. θ - 2θ x-ray scan of the GaN/GaAs layer showing the (200) and (400) peaks of the epitaxial GaN material and the GaAs substrate.

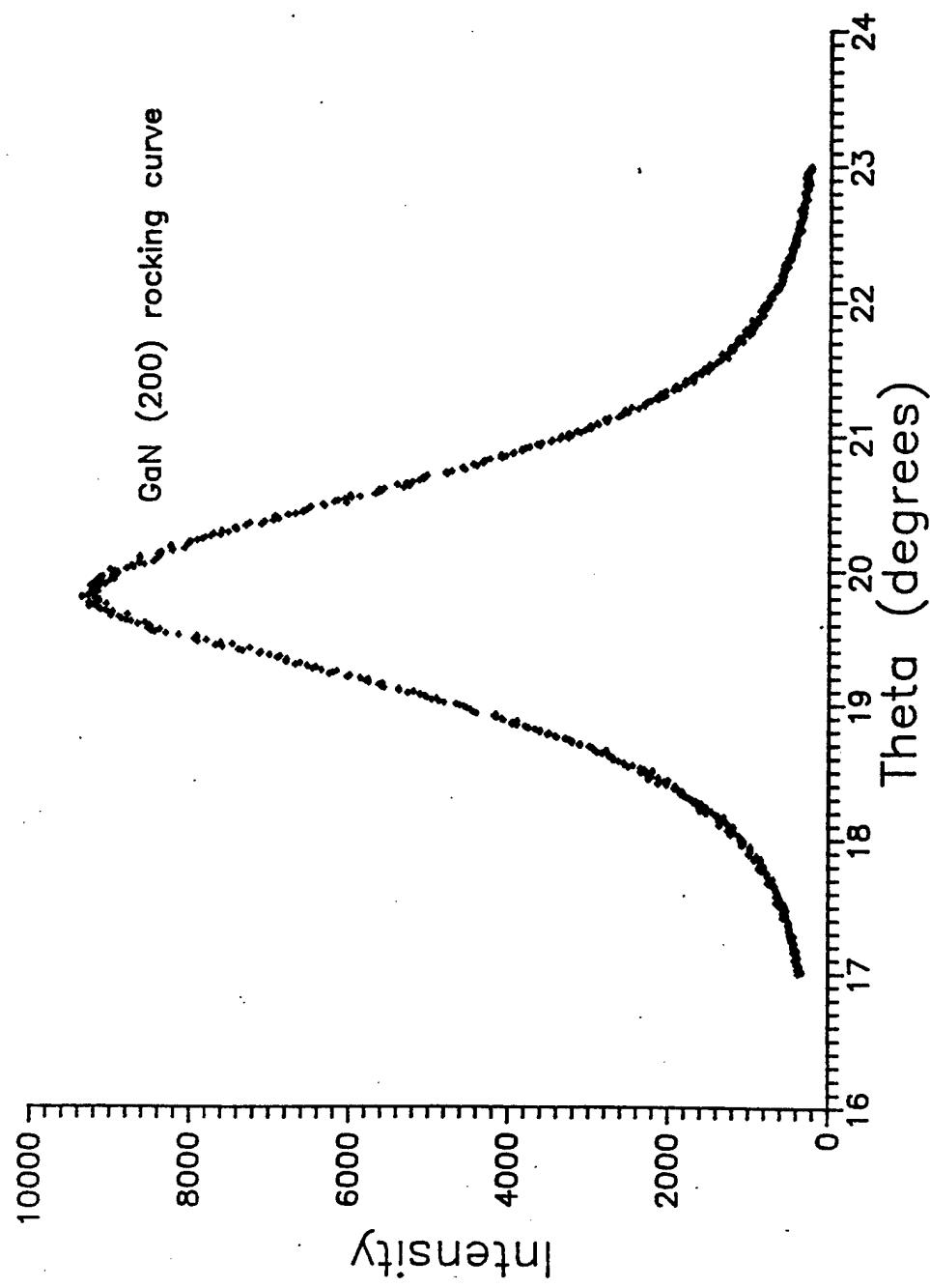


Fig. 4.11. Rocking curve of the GaN (200) peak having a FWHM of 96 minutes, a factor of two narrower than the same InN data.

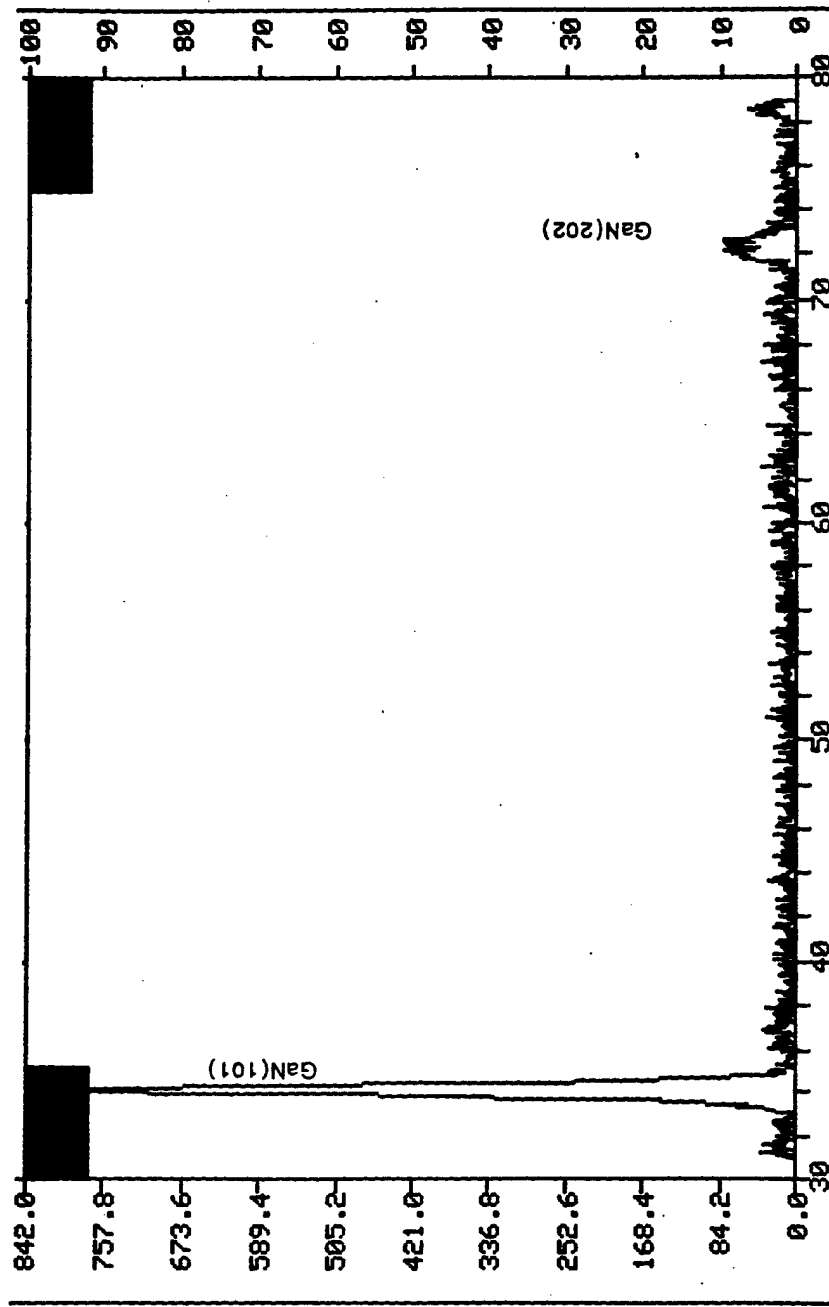


Fig. 4.12. Wurtzite GaN x-ray data for one of the wurtzite $<110>$ planes also showing the higher order (202) signal. From the position of the signal it is determined that the wurtzite GaN is stacked parallel to the epitaxial zincblend GaN.

boundary, must then be of the type shown in Fig. 4.6 (top), involving a dislocation at either end, since growth does not follow the stacking direction. Many dislocations are present, as a result of the large lattice mismatch, and these act as nucleation sites for the stacking faults. The question becomes why do we not see large wurtzite GaN domains?

We believe that the formation energies of wurtzite and zincblende GaN are roughly equal. It is then not energetically favorable, as it is in the case of InN, to nucleate a large wurtzite domain. To do so would require the formation of a polytype domain boundary as the crystal continues to grow along the [001] direction. Due to the equivalent formation energies of the two polytypes, the wurtzite domain does not find it to be energetically favorable to fight the wishes of the adjacent crystal structure and reverts quickly back to zincblende stacking. There is ample experimental evidence in the literature which supports our supposition of equivalent formation energies between the two GaN polytypes. Lei et al. [46] reported x-ray diffraction evidence of zincblende GaN in bulk wurtzite GaN films grown on (111) Si. Humphreys et al. [55] has reported the growth of bulk zincblende GaN on (0001) sapphire substrates at reduced temperatures. This proves that, under certain growth conditions, zincblende GaN is the favored phase.

The above data leads to an interesting point which is not fully appreciated in the literature. Nearly all nitride films grown to date have been deposited on either (111) cubic or (0001) hexagonal substrates on which growth proceeds along the stacking direction. Neither of these substrate orientations serves as a template for either polytype and the atomic planes are free to order in the manner dictated by thermodynamics. Numerous others have reported wurtzite GaN grown on (111) cubic and (0001) hexagonal substrates. In most cases, their determination was based on $\theta - 2\theta$ x-ray diffraction measurements which were not supported by TEM or more detailed x-ray investigation. In the 2H and 3C crystal structures, the spacing between planes in the stacking direction is nearly identical.

Therefore, $\theta - 2\theta$ x-ray diffraction measurements will obtain virtually the same data for either film type. We suspect that several workers have falsely assumed their GaN to be wurtzite based on $\theta - 2\theta$ x-ray analysis. In the future, we feel strongly that further characterization must be done before any positive determination of crystal structure can be made.

5. OPTICAL PROPERTIES OF ZINCBLENDE GaN

The motivation of our investigations of the zincblende nitride polytypes was to evaluate their potential as a short wavelength optical material. Having successfully grown zincblende GaN on GaAs, our next step was to evaluate its fundamental optical properties. Section 5.1 discusses our cathodoluminescence investigations of the 3C GaN optical spectrum which revealed several near bandedge peaks and allowed us to estimate the bandgap energy and its temperature dependence [44]. In Section 5.2, we report on the spectral dependence of the index of refraction was measured by optical reflectivity.

5.1 Cathodoluminescence

For cathodoluminescence (CL) studies of the optical quality of the zincblende GaN, the sample was mounted in an ultra high vacuum environment and spectra were obtained at various temperatures ranging from 4 K to 280 K. Figure 5.1 shows the CL spectra obtained at 4 K, 77 K and 280 K over a broad wavelength range. Each spectrum displays a broad midgap emission at energies slightly above 2 eV which becomes more dominant as the temperature is increased. Such midgap emissions are commonly observed in mediocre quality semiconductor samples as a result of impurities or other defects which act as midgap recombination centers. Numerous other workers [12], [50], [54], [56] have observed a similar broad emission in hexagonal GaN as a result of impurities or poor crystal quality. On the positive side, for the first time, a good deal of structure is apparent in the vicinity of 3.2 eV, especially at the lower temperatures.

Figure 5.2 shows the same spectra in the narrow range containing the detailed structure. A total of seven peaks are resolved and their positions at various temperatures are summarized in Table 5.1. On the high energy side, three peaks, labeled a, b, and c in order of descending energy, are clearly resolved. The peaks are roughly evenly spaced in energy.

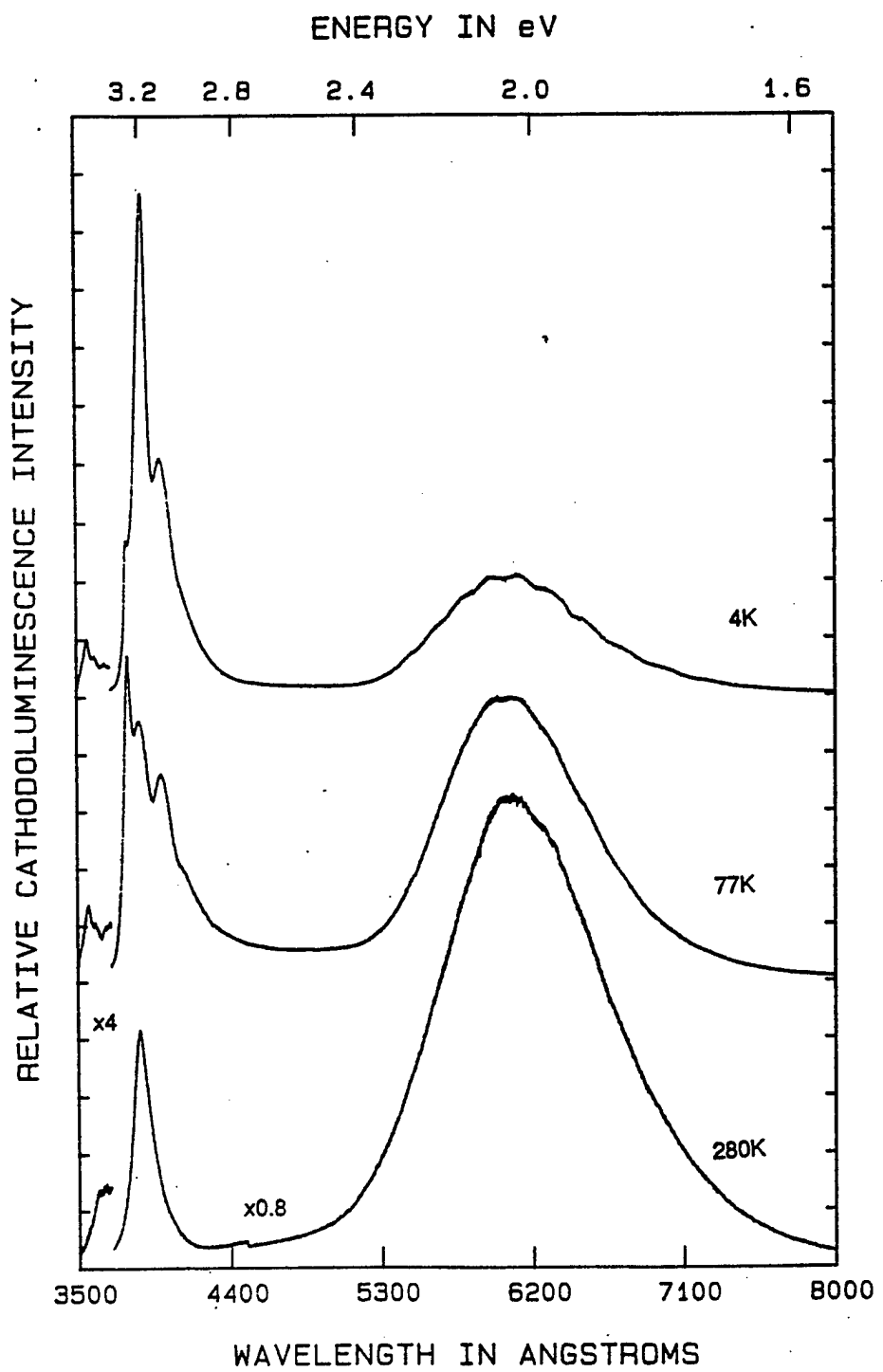


Fig. 5.1. Zincblende GaN cathodoluminescence spectra measured at 4, 77 and 280 K.

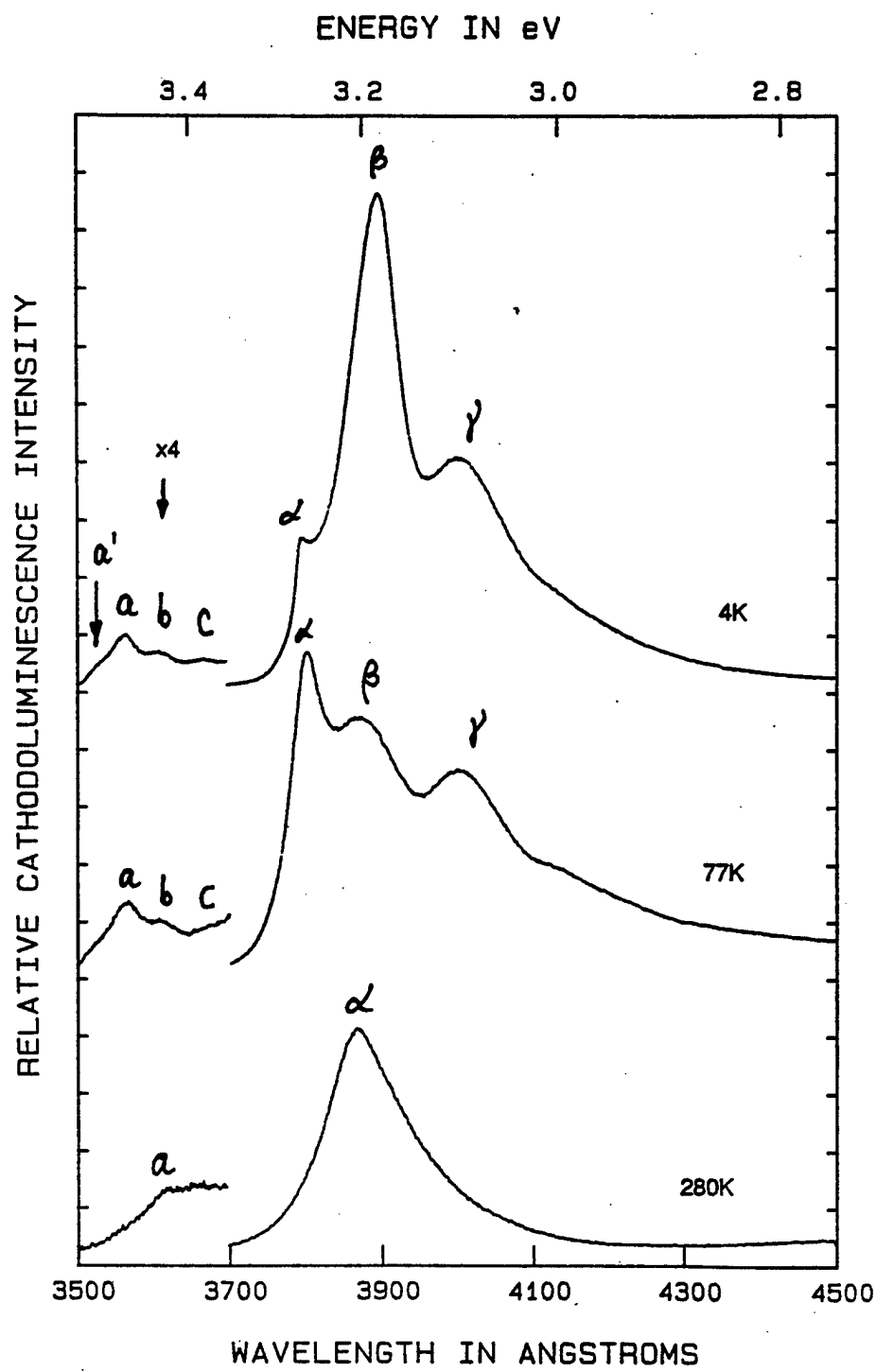


Fig. 5.2. Expanded view of Fig. 5.1 highlighting the structure in the near bandgap energy region.

No notable temperature dependence is apparent, although the relatively low intensity of these peaks makes any measurement of their temperature dependence imprecise. A weaker fourth peak situated near 3.52 eV (a') is also detected. It is most prominent in the 53 K spectrum shown in Fig. 5.3. The location of these peaks are consistent with the low temperature luminescence spectra observed in wurtzite GaN [12], [56] whose bandgap is 3.5 eV at 1.6 K [56]. The relatively low intensity of the wurtzite signal is expected in light of the structural evidence presented in the previous chapter.

Table 5.1 Temperature Dependence of Cathodoluminescence Peaks

Peak	4 K	53 K	280 K
α	3.267 eV	3.262 eV	3.206 eV
β	3.183 eV	3.196 eV	—
γ	3.096 eV	3.106 eV	—
a	3.48 eV	3.48 eV	—
b	3.44 eV	3.43 eV	—
a	3.38 eV	3.38 eV	—
a'	~3.51 eV	~3.52 eV	—

The three most intense peaks, labeled α , β , and γ in order of decreasing energy, have different temperature dependences. At 4 K the 3.18 eV β peak dominates the spectrum. As the temperature increases, the α peak becomes predominant with the β peak falling off rapidly in intensity. The α peak shows a marked temperature dependence, shifting to lower energy as the temperature is raised, while the β and γ peaks shift to higher energy. At 280 K, only the α peak, now shifted to 3.21 eV, is resolved.

Because there are no optical data for cubic GaN available in the literature, we must speculate as to the nature of the α , β and γ peaks. It is enlightening to compare our data with that of wurtzite GaN. Based on the photoluminescence data of Dingle et. al. [11],

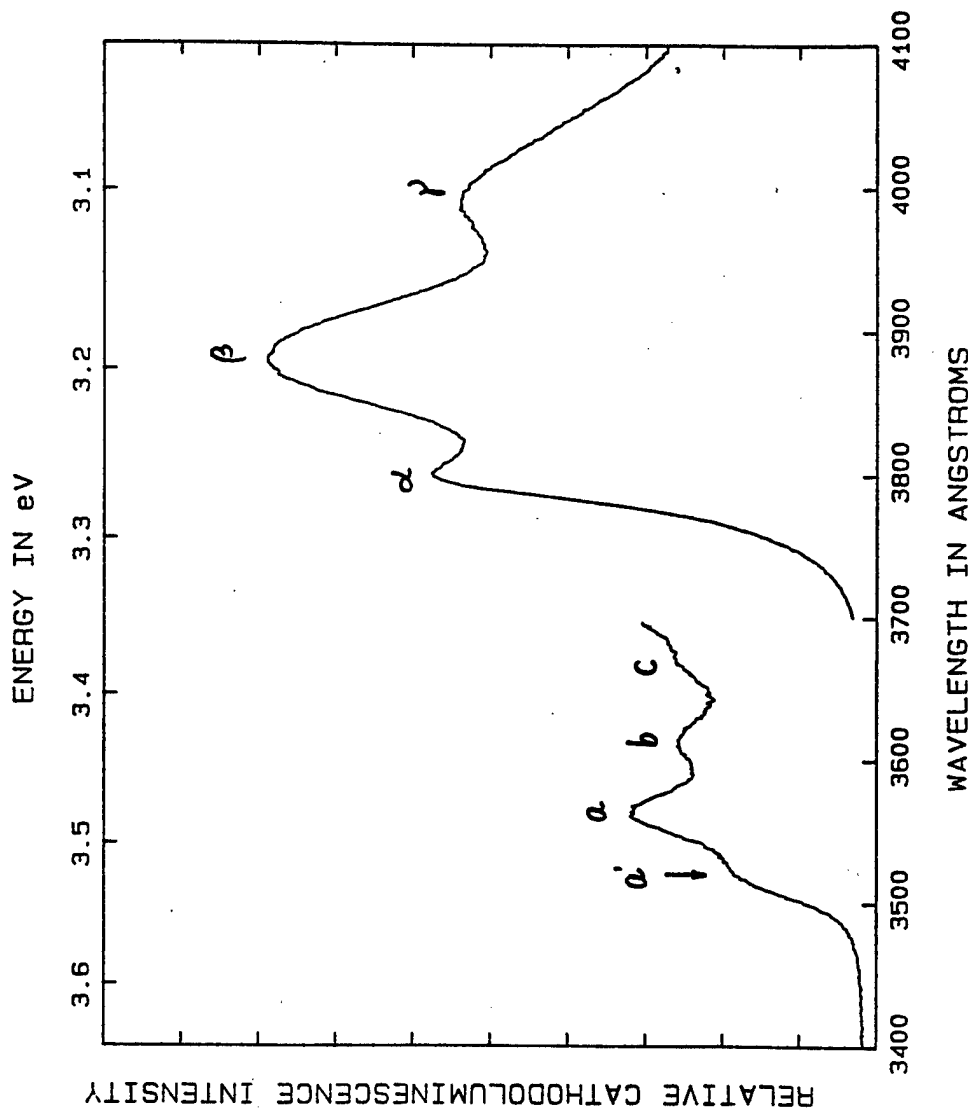


Fig. 5.3. Cathodoluminescence spectrum at 53 K which best reveals the highest energy wurtzite GaN peak.

we believe that our α and β peaks may also be the free electron-bound hole and donor-acceptor (D-A) pair recombination signals, respectively. In wurtzite GaN, those workers reported a high-energy band (HEB) superimposed onto the D-A pair spectrum. At high temperature, the HEB dominated the D-A pair recombination spectrum. Our data behave similarly, with the β peak being dominant at low temperature while being supplanted by the higher energy α peak at higher temperatures. This is consistent with the thermal activation of the donor level which quenches the D-A emission.

The broadened room temperature α peak is almost certainly the band-to-band transition or the free-to-bound since it is unlikely that room temperature excitons could exist amidst so many structural defects. In that case, we can establish the bandgap of zincblende GaN to be 3.2 - 3.3 eV. Our value is consistent with two subsequent bandgap measurements which obtained 3.3 eV [57] and 3.2 eV [44] by optical transmittance and absorption respectively. Our data and others' indicate that zincblende GaN has a direct bandgap slightly below that of the wurtzite GaN polytype.

Following our earlier assignment of the α peak to the free to bound transition, then the temperature dependence of the α peak should follow the temperature dependence of the bandgap. Figure 5.4 displays the relationship of the α peak position with temperature in which the data were fit to the polynomial function

$$E = 3.266 - 2.015 \times 10^{-6}T - 7.105 \times 10^{-7}T^2 - 6.366 \times 10^{-11}T^3. \quad (5.1)$$

The function predicts the low temperature bandgap value to be 3.266 eV. At high temperature, the data fall closely onto a straight line having a slope of -3.5×10^{-4} eV/K.

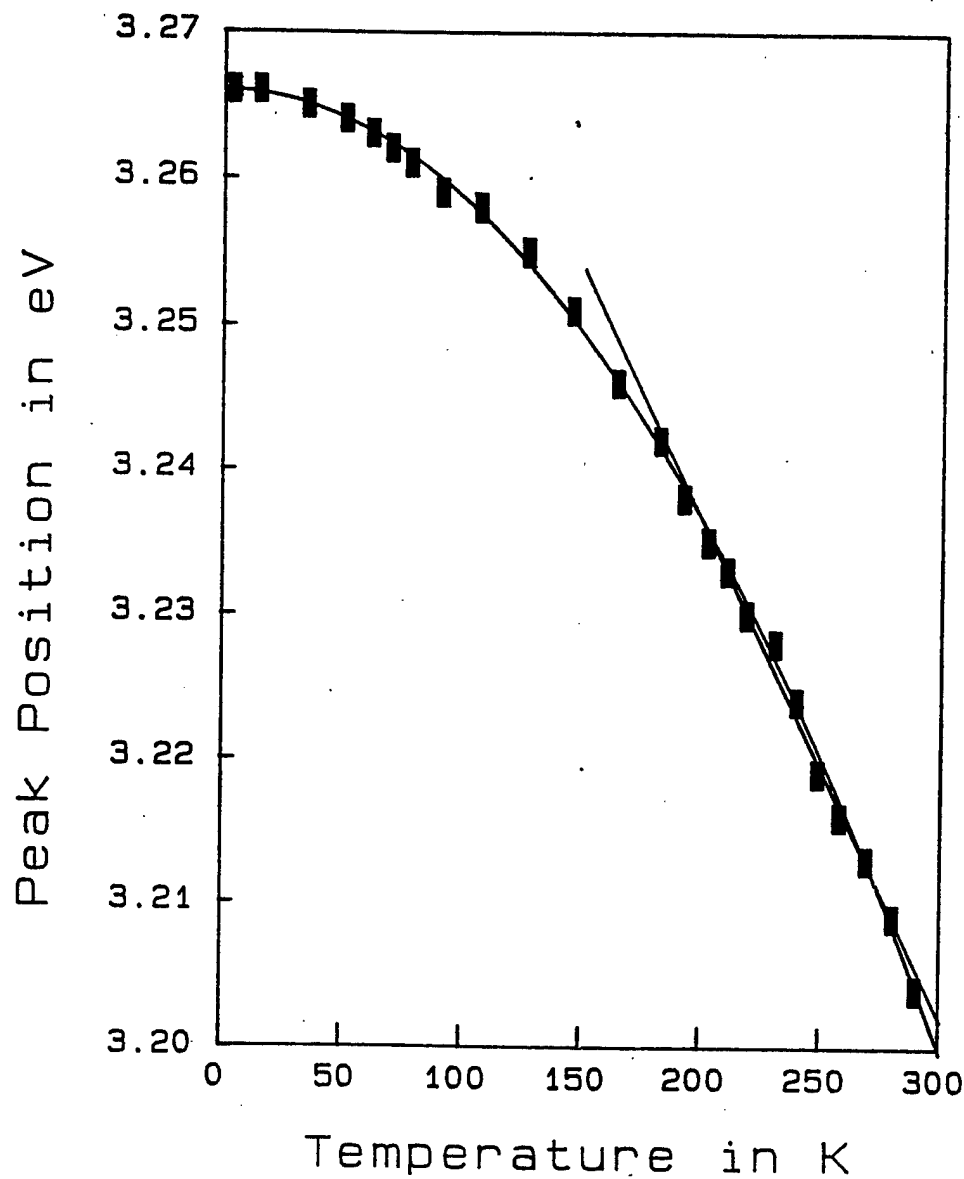


Fig. 5.4. Temperature dependence of the α peak position. A roughly linear region extends down to 150 K.

5.2 Optical Reflectivity and the Refractive Index

An important property of semiconductor materials is the wavelength dependent index of refraction which can be measured by observing the modulation of the optical reflectivity as a function of the incident light wavelength. Zincblende GaN grown on GaAs substrates is particularly well suited for this experiment since the expected value of the GaN refractive index falls midway between that of GaAs and air causing multiple internal reflections and large amplitude oscillations in the reflected light intensity.

In our experiment, an unpolarized collimated beam from a broadband Tungsten-Halogen lamp was shone on GaN/GaAs samples. The reflected beam was collected at the entrance slit of a grating monochromator. By using several gratings, we were able to obtain data from 0.8 eV - 3 eV. The light intensity was measured from 3.3 eV to 1.2 eV using an ultraviolet enhanced Si photodiode which was replaced by a PbSe photoresistor for the infrared wavelengths. The spectral resolution of our optical experiment was roughly 20 Å. Thickness measurements of the GaN epilayers were made using secondary ion mass spectroscopy (SIMS). The SIMS technique uses electrostatically accelerated ions to sputter a crater in the material to be studied. An in situ mass spectrometer measures the composition of the sputtered material. Our samples were sputtered down to the GaN/GaAs interface which was detected by the onset of an As signal. The depth of the crater was then measured using an Alpha-Step profilometer which allowed the total thickness of the GaN epilayer to be measured to within an estimated accuracy of 300 Å.

Figure 5.5 shows the raw reflectivity data collected with the Si photodiode from one sample. Because of the large modulation of the reflected light intensity, we could accurately measure the position of the maxima and minima. Table 5.2 is a compilation of those data for our best sample, A908, whose measured thickness was $1.58 \pm 0.03 \mu\text{m}$.

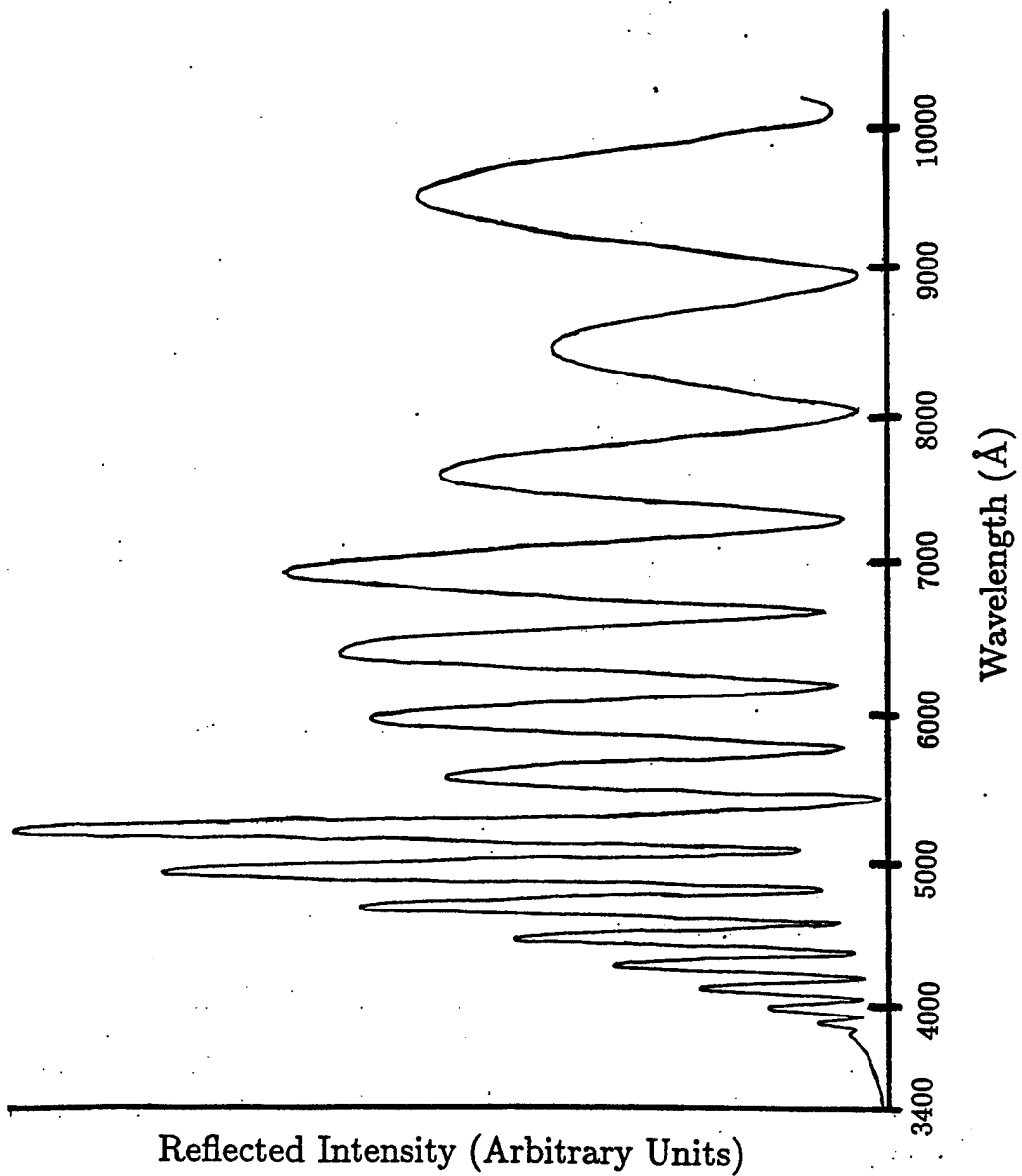


Fig. 5.5. Raw reflectivity data from A908 collected using the Si photodiode.

Table 5.2 A908 Reflectivity Maxima and Minima

Maxima	λ (Å)	Energy (eV)	Minima	λ (Å)	Energy (eV)
	3855	3.214		3882	3.192
	3910	3.169		3935	3.149
	3977	3.115		4023	3.080
	4080	3.037		4140	2.993
	4210	2.943		4282	2.894
	4357	2.844		4448	2.786
	4543	2.727		4645	2.667
	4760	2.603		4877	2.540
	4995	2.480		—	—
	5290	2.342		5440	2.278
	5620	2.205		5810	2.133
	6010	2.062		6220	1.992
	6480	1.912		6730	1.841
	6990	1.773		7320	1.693
	7640	1.622		8050	1.539
	8490	1.459		8900	1.392
	9600	1.291		10400	1.191
	10850	1.142		11650	1.064
	12600	0.983		13650	0.908
	14860	0.834		—	—

Each maximum and minimum of the reflectivity data corresponds to a condition of constructive or destructive interference, respectively. To correctly calculate the index of refraction, the effect of the GaAs substrate had to be taken into account. The GaAs acts as a lossy dielectric, allowing the field to impinge into it while absorbing some of the light ($E_g^{\text{GaAs}} = 1.4$ eV). The presence of the GaAs serves to slightly increase the effective thickness of the GaN cavity and also introduces a phase shift upon reflection of the incident light. Both the real and imaginary refractive indices of GaAs have been measured and are readily available. The GaN index of refraction was assumed to be real since all of the data

was collected below the bandgap energy where the GaN is transparent.

Our approach was to numerically calculate a reflectivity spectrum for our structure from the known optical constants of GaAs and our measured GaN thickness. At normal incidence, Fresnel's equation for the reflected light amplitude reduces to:

$$r_{1,2}^p = \frac{n_2 - n_1}{n_2 + n_1}, \quad (5.2)$$

and

$$r_{1,2}^s = \frac{n_1 - n_2}{n_2 + n_1}, \quad (5.3)$$

where the superscripts s and p represent the two perpendicular polarizations and the refractive indices are, in general, complex numbers. The experimentally observed reflected intensity of unpolarized light is the magnitude of the amplitudes of the two polarizations given by

$$R = \frac{1}{2}(r^p r^{p*} + r^s r^{s*}). \quad (5.4)$$

The model for the two interface case is shown schematically in Fig. 5.6. The overall amplitude of the reflected light obtained by summing all of the reflected components and matching the boundary conditions is

$$r_{p,s} = \frac{r_{0,1}^{p,s} + r_{1,2}^{p,s} e^{-ix}}{1 + r_{0,1}^{p,s} r_{1,2}^{p,s} e^{-ix}} \quad (5.5)$$

where

$$x = (2\pi/\lambda)2n_1 d_1 \quad (5.6)$$

with λ being the wavelength of incident light and d_1 the measured GaN thickness.

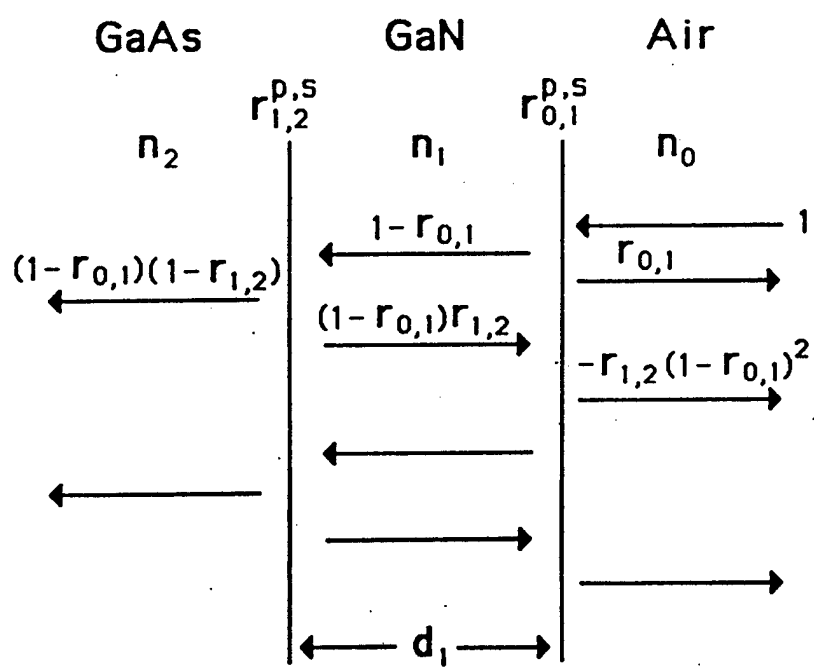


Fig. 5.6. Schematic of our reflectivity experiment.

The GaN index of refraction, n_1 , was used as a fitting parameter at each maxima and minima until the extremum of the calculated reflectivity matched the location of the data point of interest. Figure 5.7 is a plot of our results which shows the measured spectral index of refraction for two zincblende GaN samples, A908 and A943. The major experimental uncertainty in our results arises from the estimated 300 Å uncertainty in the GaN film thickness measurement which enters linearly into the final uncertainty. Our determination of the extrema from the optical data and the accuracy of the numerical calculations each have much smaller uncertainties. The two measured samples were of the order of 1.5 μm , so we estimate that our results for the GaN index of refraction have an error of no more than 3%.

Our index of refraction data for zincblende GaN are typical of a semiconductor. The long wavelength region has a nearly constant refractive index value in the neighborhood of $n = 2.4$. At these wavelengths, the light interacts weakly with the GaN. As the bandgap is approached, the refractive index of A908 increases rapidly as the GaN begins to absorb the incident light, behaving more like a metal. Our measured index of refraction at the zincblende GaN bandgap is $n = 2.91 \pm 0.01$. This is the quantity of most interest for semiconductor laser designers. Notice that the data for A943 appear more flat and diverge less rapidly as the bandgap is approached. This was a lower quality sample with a much larger background electron concentration and more below band edge absorption centers. Therefore, strong absorption occurs at lower photon energies and the onset of the band edge is less dramatic. It was not possible to take data above the bandgap using our modulated reflection technique since the onset of strong absorption means that the amplitude of internally reflected light was insufficiently large to provide reasonable interference with the externally reflected component.

Refractive index of cubic GaN

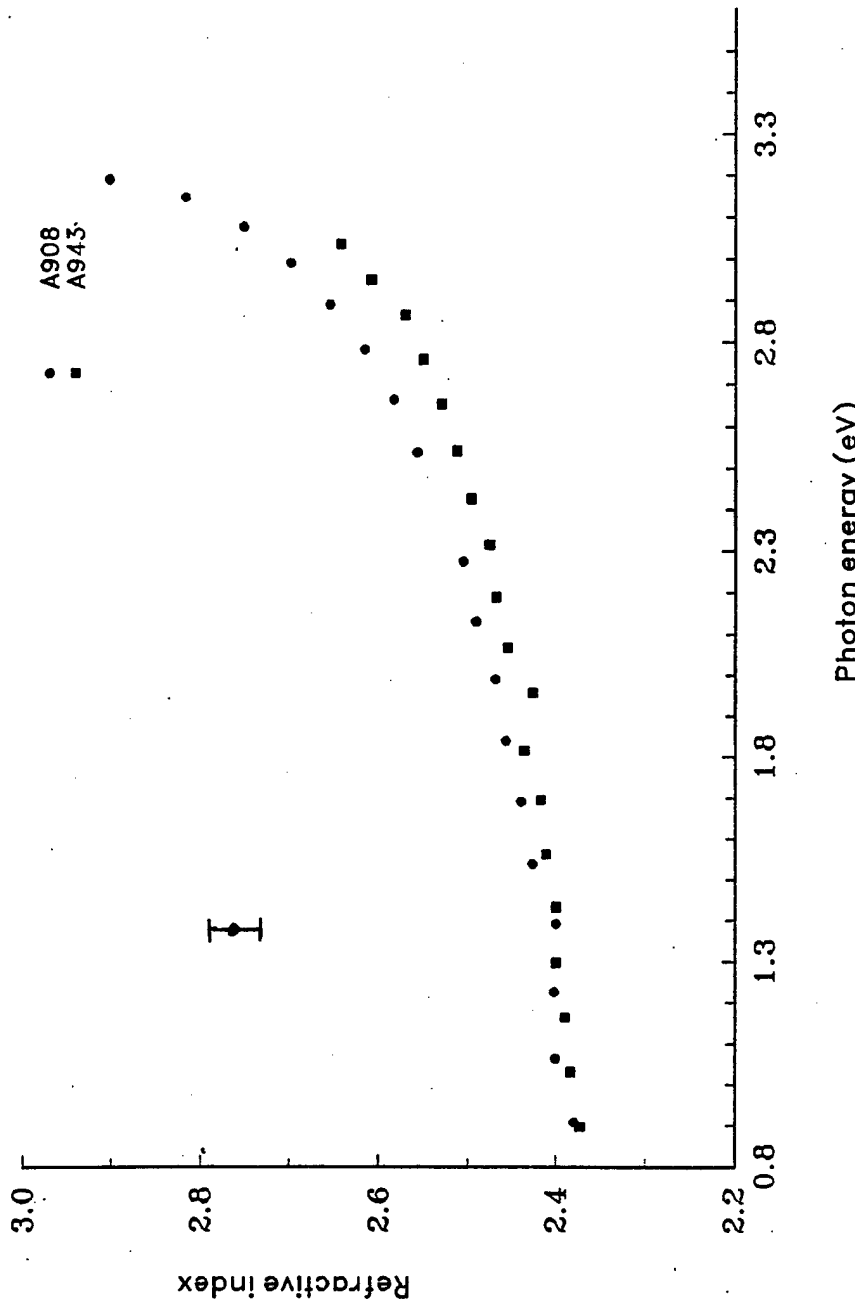


Fig. 5.7. Spectral dependence of the refractive index for the two samples studied. The experimental uncertainty (inset) arises mostly from the SIMS determination of the GaN thicknesses.

6. GaAs-GaN SEMICONDUCTOR-INSULATOR DEVICE STRUCTURES

The III-V nitrides, with their wide bandgaps, have long been viewed as a potential insulator material for GaAs and other compound semiconductors. As a prospective insulator material for GaAs, GaN suffers from a 20 % lattice mismatch as well as significant thermal mismatch (Table 3.1). In its favor, GaN is isoelectronic with GaAs which simplifies the interface considerably. The SiO_2/Si system provides the model insulator-semiconductor interface despite its fairly large lattice mismatch (6.7 %), so it appears possible that the lattice mismatched GaN on GaAs system may perform well. Only one group [60] has previously investigated GaN-GaAs insulator-semiconductor structures and their results were quite poor. By studying such structures, we can investigate the quality of the initial heteroepitaxial GaN as well as evaluate the potential of GaN as an insulator material for GaAs. In this chapter we present the first comprehensive investigation of the insulating properties of zincblende GaN for GaAs device structures. In Section 6.1 we describe the properties of a GaN/GaAs metal-insulator-semiconductor diode [48]. In Section 6.2, the properties of a GaAs/GaN/GaAs semiconductor-insulator-semiconductor diode are presented [49].

6.1 GaN/GaAs Metal-Insulator-Semiconductor Diodes

Figure 6.1 shows the metal-insulator-semiconductor (MIS) diode structure. The devices were grown on n-type conducting GaAs substrates. After the growth of a $1 \mu\text{m}$ lightly doped GaAs buffer layer, GaAs growth was interrupted and nitride growth was initiated using shuttered Ga flux in the manner described in Chapter 3. A total of 500 Å of GaN insulator was deposited. MIS diode structures were fabricated by evaporating 150 μm radius Au Schottky contacts onto the GaN surface. Au evaporated onto the back side of the GaAs substrate formed the ohmic contact.

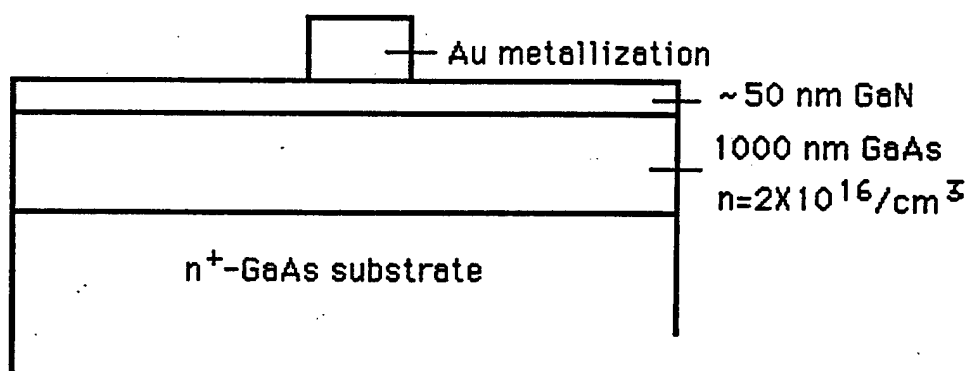


Fig. 6.1. Schematic of GaN/GaAs MIS diode layer structure.

The MIS structures were investigated by room temperature capacitance-voltage (C-V) and current-voltage (I-V) measurements. The room temperature C-V characteristics at 100 kHz and 1 MHz of a GaN/GaAs MIS diode are presented in Fig. 6.2. At each individual frequency there is very little hysteresis which indicates that the number of bulk GaN traps is low. However, there is a significant change in the measured capacitance as a function of the sweep frequency. Similar behavior in the Si_3N_4 /GaAs MIS system [61], [62] has been shown to be interface related. Our C-V data nearly resemble the ideal S-shaped curves generated in the best Si-based MIS structures. In the forward bias condition, the capacitance shows signs of saturation, especially in the 1 MHz sweep, indicating the possibility of accumulation. We attribute the lack of complete saturation to the large leakage current of the device in forward bias mode. Inversion is achieved as indicated by the flat C-V relationship in the reverse bias condition. The C-V data indicate that the interface is unpinned as evidenced by our ability to sweep the Fermi level from inversion nearly to accumulation. Following the methods of Ref. 61, by comparing the amount of experimentally observed stretch-out (voltage necessary to sweep from inversion to accumulation) to a theoretically generated ideal curve, we estimate an interface state density of approximately $5 \times 10^{11}/\text{cm}^2\cdot\text{eV}$ in our GaN/GaAs device. This value is approximately an order of magnitude above what is normally considered to be device quality.

Room temperature I-V measurements (Fig. 6.2 (inset)) show rectification, the expected behavior for a diode structure. However, the current levels in both forward and reverse bias are fairly large which indicates that the GaN is a leaky insulator. The leakiness may stem from the many defects present in the GaN, or from the natural n-type background carrier concentration normally observed in GaN. The insulator breakdown was observed at 22 V reverse bias which corresponds to a field of $4 \times 10^6 \text{ V/cm}$ based upon the 500 Å GaN thickness.

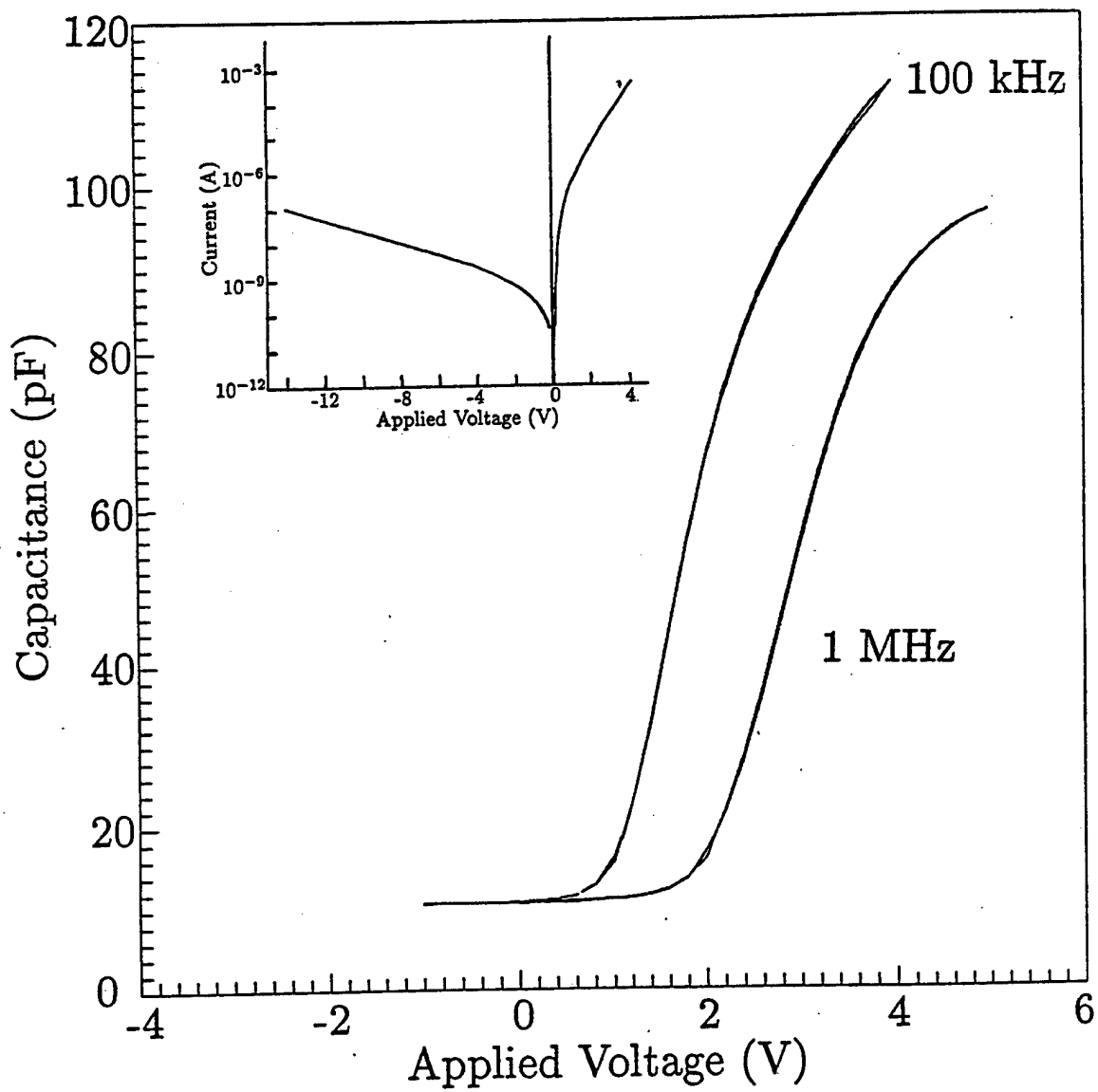


Fig. 6.2. GaN/GaAs MIS C-V characteristics at 100 kHz and 1 MHz. Inset: Room temperature I-V characteristics.

6.2 GaAs/GaN/GaAs Semiconductor-Insulator-Semiconductor Diodes

GaAs/GaN/GaAs semiconductor-insulator-semiconductor (SIS) diodes were also investigated. By making an n-type device, we intended to measure the temperature and voltage dependence of the electron current in order to estimate the conduction band offset between GaAs and GaN. First a thick lightly doped n-type GaAs layer was grown on the semi-insulating GaAs substrate. Next, a GaN interlayer was deposited and finally, a heavily doped GaAs cap layer was grown. A TEM image of the described structure is shown in Figure 3.12, from which an insulator thickness of 45 Å was determined. A thin GaN layer was needed to insure a reasonable amount of current flow. On the other hand, the GaN needed to be sufficiently thick so as to permit negligible amounts of tunnelling current. Figure 6.3 shows the calculated conduction band profiles of the SIS structure under reverse and forward bias conditions.

The current-voltage (I-V) characteristics of the SIS structure was investigated at temperatures ranging from 300 K to 340 K. The data are plotted in Figures 6.4 and 6.5. Below 300 K, the reverse bias current level falls below that which we can reliably measure. Rectification is observed with the reverse bias current remaining quite small even up to 15 V while the forward bias current increases rapidly with applied voltage. The I-V behavior is determined by the properties of the depletion layer. In the reverse biased mode, the majority of the applied voltage is dropped across the depleted region while comparatively little is dropped across the thin GaN barrier. This is shown in Fig. 6.3 (a). Under forward bias the collector region goes into accumulation causing a large fraction of the voltage to appear across the barrier, severely tilting it and adding unwanted complexity to the problem of extracting the effective barrier height. This situation is shown in Fig. 6.3 (b). Two factors control the current flow in the SIS structure, and comparing Figs. 6.3 (a) and (b), we can qualitatively see why the forward bias currents are larger than the reverse bias

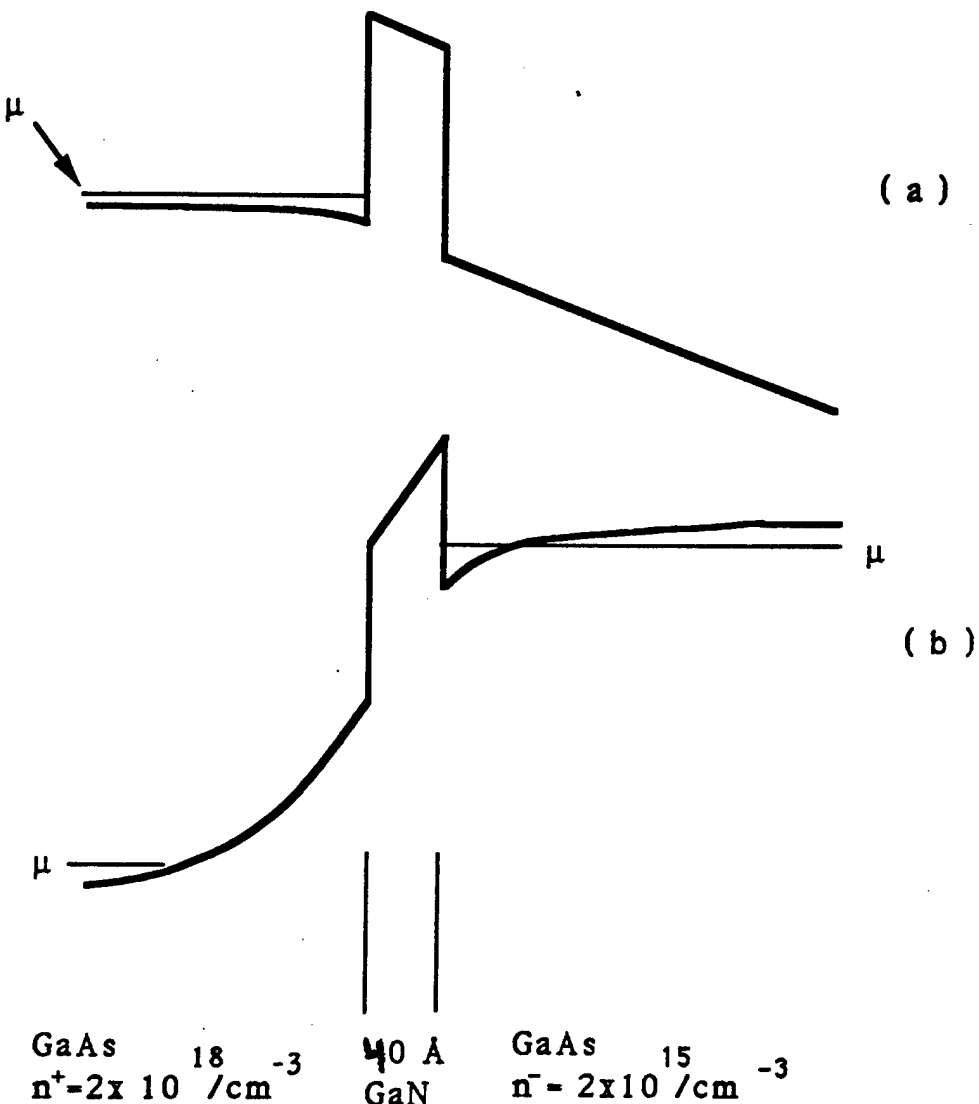


Fig. 6.3. Conduction band profile of the SIS diode showing 300 Å of the emitter and 500 Å of the collector. (a) At 15 V applied reverse bias 0.13 V appears across the barrier. (b) At 2 V forward bias 0.65 V appears across the barrier.

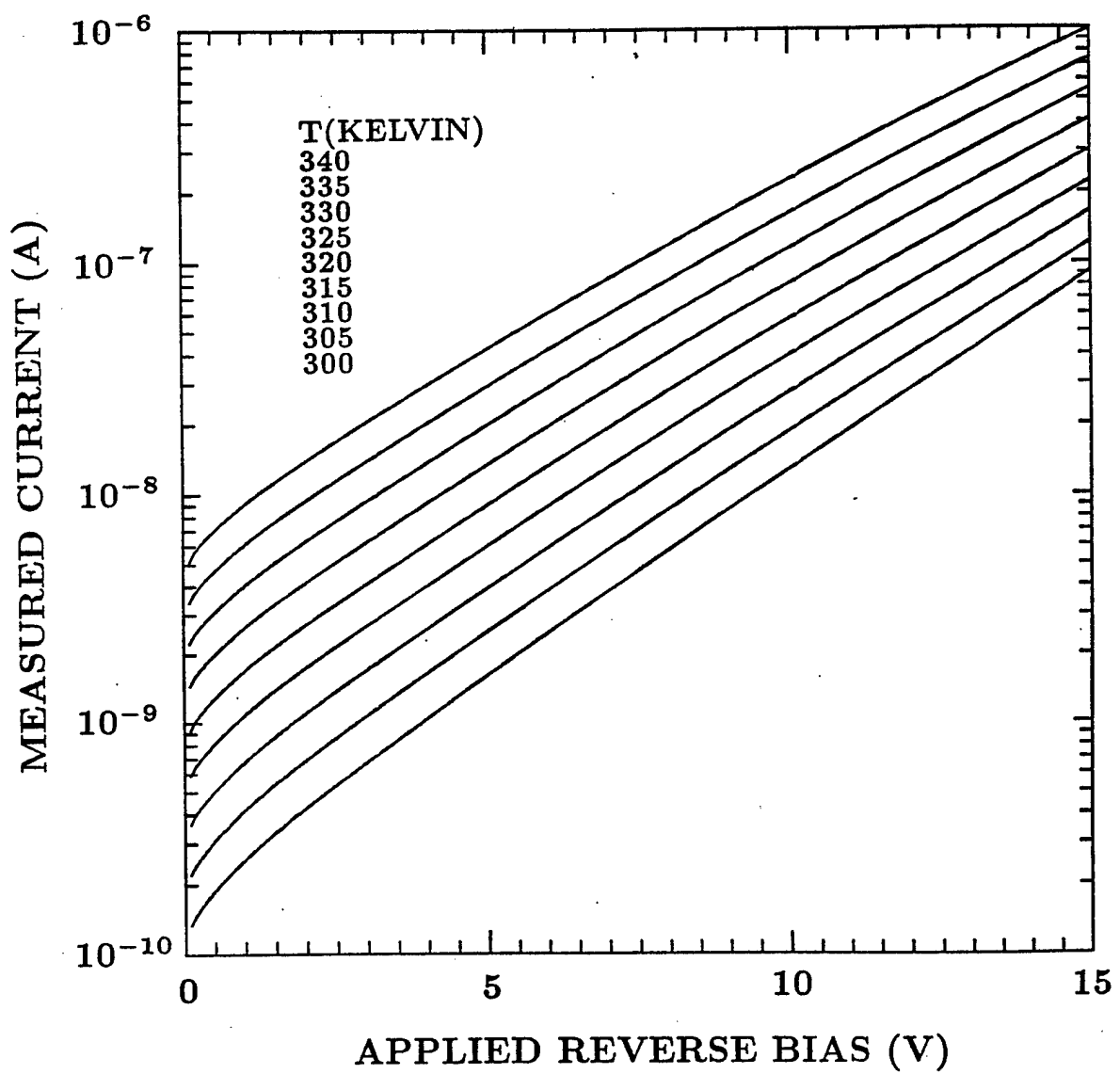


Fig. 6.4. Experimental reverse bias I-V curves from 300 K to 340 K.

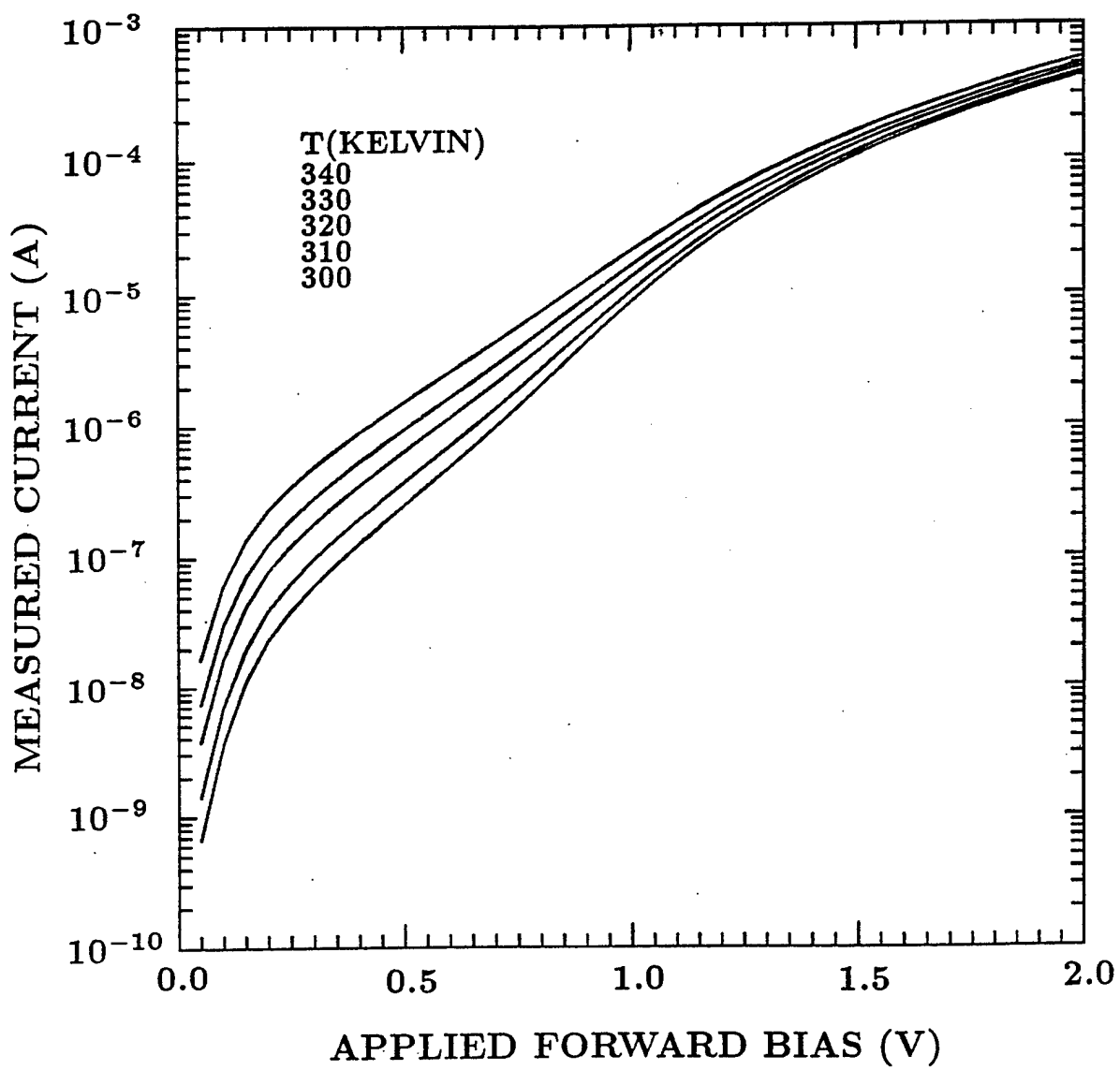


Fig. 6.5. Experimental forward bias I-V curves from 300 K to 340 K.

currents. First, the accumulation band bending in the collector region of Fig. 6.3 (b) is much larger than the accumulation band bending in the emitter of Fig. 6.3 (a). The accumulation band bending pulls down the barrier top with respect to the Fermi level thereby decreasing the effective barrier height to electron current. Second, the triangular top of the barrier is less effective as an insulator because electrons can more easily tunnel through the thin part of the barrier. Both of these factors lead to large forward bias currents.

The reverse bias data show a marked dependence on temperature, and it is from this dependence that we extract the effective conduction band barrier. The essential idea in this analysis is that the majority of the current flow occurs in the narrow energy range just above the effective top of the barrier, and that the concentration of electrons in this energy range is given by a thermal distribution function. The assumption of a thermal distribution is justified because the electron source terminal (emitter for reverse bias, collector for forward bias) is in accumulation so that electron-electron interactions are significant and maintain a thermal distribution even for electrons high in the conduction band. Then the concentration of electrons in the energy range just above the effective barrier top is proportional to $e^{\frac{-(E_b - \mu)}{k_b T}}$ according to Fermi-Dirac statistics, where E_b indicates the effective top of the barrier (assuming $E_b - \mu \gg k_b T$). The concentration of electrons will fall off quickly with energy above E_b so that only the electrons just above the barrier top will contribute significantly to the current. Unfortunately the effective barrier top is approximately an electron volt above the GaAs conduction band minimum which invalidates the effective mass approximation. Therefore we do not know the density of states or the velocity of electrons in this energy range, so the only statement we can make about the current density is that $j = Ce^{\frac{-(E_b - \mu)}{k_b T}}$, according to Fermi statistics, where C is a polynomial in temperature which contains information about the electron density of states and velocity. This statement is fairly general and can be shown for several other examples in which the

majority of conduction electrons are in a narrow energy range, such as thermionic emission over a Schottky barrier and conduction through a narrow midgap state [64]. For these two cases C has a T^2 and T^0 dependence, respectively. The relatively narrow temperature range in which our measurements are restricted does not allow us to distinguish between these cases. C is left as an unknown to be fit by the data.

Plotting $\ln(j)$ versus $\frac{1}{k_b T}$ for the measured temperatures at each voltage gives a straight line with slope $-(E_b - \mu)$ and intercept $\ln(C)$. $E_b - \mu$ is shown in Fig. 6.6 (1) while $\ln(C)$ is shown in Fig. 6.7 (3). $E_b - \mu$ decreases with voltage due to the effects discussed earlier, namely accumulation band bending and slight barrier tilting. The band bending is calculated by assuming the current flow is small and requiring the continuity of electric displacement across the device. By simply adding the relative energy constituents, $E_b - \mu$ can be related to the effective barrier height by

$$E_b - \mu = E_{c,\mu} - q_e \phi_{abb} + q_e \phi_b - q_e \phi_{tri} \quad 6.1$$

where $E_{c,\mu}$ is the difference between the conduction band minimum and the Fermi level in the bulk emitter, ϕ_{abb} is the accumulation band bending at the GaAs/GaN interface, ϕ_b is the effective conduction band barrier height, and ϕ_{tri} is the voltage drop across the barrier (for a first approximation the triangular part of the barrier is assumed to be transparent). $E_{c,\mu}$, ϕ_{abb} , and ϕ_{tri} are all functions of temperature, so the data must be re-fit with these corrections to find ϕ_b . ϕ_b is shown in Fig. 6.6 (2), while the second fit for $\ln(C)$ is shown in Fig. 6.7 (4). Our fit yields an effective conduction band barrier height is about 0.9 eV. Even with the band bending corrections there is still a slight decrease in ϕ_b with increasing voltage. We can expect a large number of defect states spread throughout the GaN forbidden gap due to structural defects arising from the very large lattice mismatch

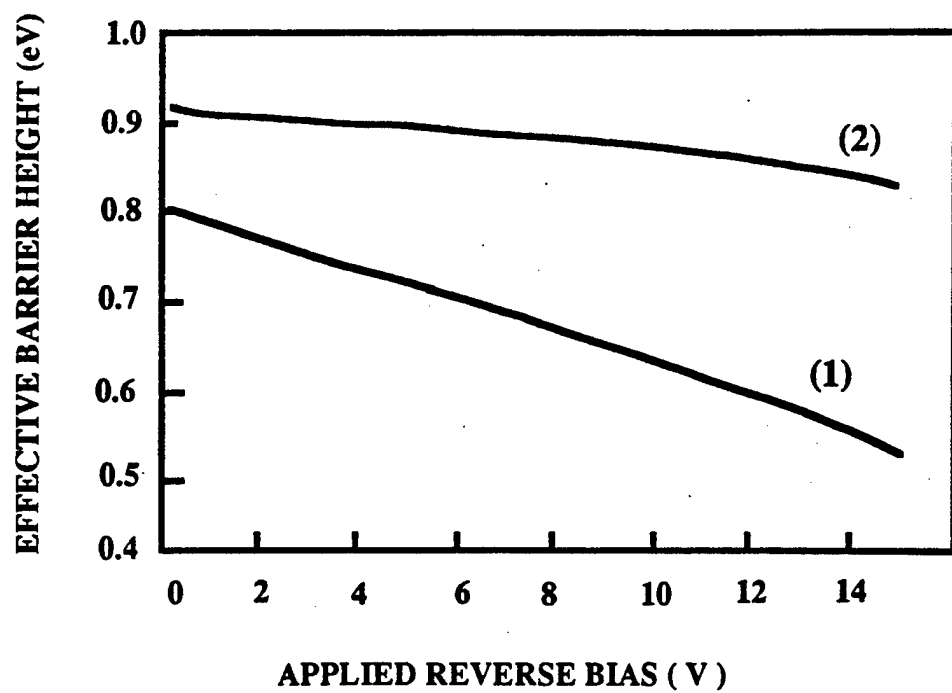


Fig. 6.6. Parameters fit from the experimental data as a function of voltage. Curve (1) displays $E_b - \mu$ while curve (2) shows ϕ_b from the fit adjusted for band bending.

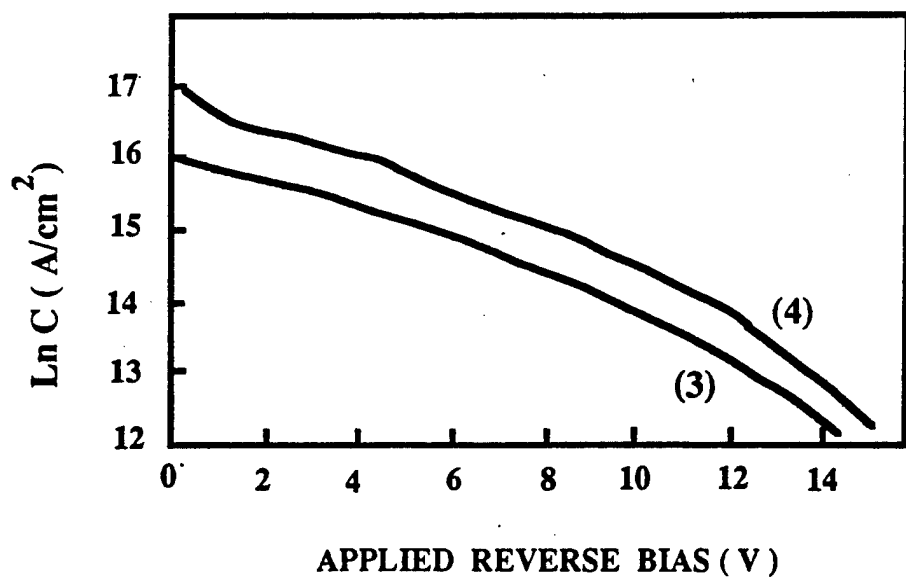


Fig. 6.7. $\ln(C)$ values fit from the experimental data as a function of voltage. Curves (3) and (4) were calculated without and with band bending respectively.

between GaN and GaAs. As voltage increases electrons trapped in defect states just below the conduction band edge can escape more easily through the low energy side due to barrier tilting. Therefore more of the current is conducted through midgap states which decreases the overall effective barrier height. The strong voltage dependence of $\ln(C)$ can be attributed to a decrease in the overall effective barrier height with voltage because of the downward shift in conduction electron energy range and the corresponding decrease in velocity and density of states from which C derives.

7. XPS VALENCE BAND STUDIES

X-ray photoemission spectroscopy (XPS) is not only a useful technique for the study of surface chemistry as reported in Chapter 3, but it can also be used to probe valence band (VB) structure. This is because the XPS technique uses monoenergetic soft x-ray photons to ionize atoms in the material under study. Liberated electrons have kinetic energies equal to the difference between the photon energy and the electron binding energy, and therefore carry information about the energy of the original electronic state. At normal temperatures, the VB is, for practical purposes, fully occupied so the low binding energy region of XPS spectra is roughly proportional to the density of states. In the 10 - 25 eV range, the energy positions of lower VBs can be measured allowing information about the ionicity gap and band structure of the semiconductor to be determined.

The III-V nitrides are an interesting material system for VB studies for several reasons. Due to the strong binding of the nitrogen anion, these semiconductors are more ionic than typical III-V semiconductors. Therefore, the predicted band structures of GaN and AlN have some resemblance to those of II-VI semiconductors while some III-V character is also evident [65]. XPS measurements can provide information about the magnitude of the ionicity or heteropolar gap between the upper and lower lying VBs. This measurement provides important clues regarding the nature of the material's VB structure. In the case of the nitrides, this ionicity gap value is a measure the II-VI versus III-V flavor of the overall band structure. Additionally, both InN and GaN have d-shell core electrons whose energies lie close to the predicted N 2s - like VB. Recently, theorists [66] have realized that these shallow d-shell levels can not be treated as inert core levels, as has often been done in the past [67], [68], [69]. Rather, they hybridize strongly with the s- and p-levels of the VB, having a profound influence on the material's band gap, structure, acceptor energy

levels, and even VB heterojunction offsets [65], [70]. Finally, despite its limited resolution, the relative band gap energy differences between AlN and GaN and InN are sufficiently large that XPS can be used to make a meaningful estimate of the type of band lineups present in GaN/AlN and InN/AlN heterojunctions.

In Section 7.1, we present the details of our experiment and discuss possible sources of error. Section 7.2 describes XPS measurements on bulk zincblende GaN and InN layers. The VB spectra of wurtzite GaN, AlN and InN are reported in Section 7.3. Finally, in Section 7.4, spectra taken on thin GaN/AlN and InN/AlN epilayers are analyzed to estimate the VB offsets of these heterojunctions.

7.1 Experiment

The XPS spectra presented in this chapter were obtained using Al K_{α} radiation ($h\nu = 1486.6$ eV) having a linewidth of ~ 1 eV on a Perkin Elmer PHI 5300 ESCA system. VB photoelectrons, which have kinetic energies roughly equal to the Al K_{α} energy, have an escape depth of ~ 25 Å [71]. Bulk data were collected at electron emission angles of 45° while spectra of heterojunctions were taken at a 75° electron emission angle to increase our sensitivity to the underlying material. All of our data are energy normalized so that a linear extrapolation of the VB edge intersects the x-axis at a binding energy of zero. The size of the ionicity gap was determined by subtracting the linearly extrapolated x-intercepts of the high energy edge of the upper VB and the low energy edge of the d-shell core level (for GaN and InN) or the lower VB (for AlN).

Several possible sources of error were investigated. For wide bandgap semiconductors, surface charging can be a concern since the conductivity of the material may not be sufficient to replace ejected electrons. InN has always been observed to have high background electron concentrations [1] so we were not concerned about these spectra. However, spectra

taken on GaN and AlN showed evidence of charging, namely in broadened peaks and a featureless VB edge. We found that by heavily doping these materials with Si, charging effects could be eliminated allowing the VB structure to be resolved.

The rise and fall rates of the investigated peaks were compared to a Au $4f_{5/2}$ standard which had a full width half maximum (FWHM) of 1.2 eV. Our data approached but did not equal the slopes and FWHM of the Au signal indicating that our data were not instrumentally limited but were nevertheless representative of good material.

The surfaces were all verified to be unreconstructed (1×1) as observed by RHEED. Also, when possible, we compared the energy of shallow core levels to deeper, more chemically isolated core levels. Both a heavily reconstructed surface or a heterojunction interface can be a source of uncertainty due to the core level chemical shifts caused by highly strained surface or interface atomic bonds. Since our surfaces were unreconstructed and our heterojunctions were common anion and isoelectronic, we expected such effects to be minor. Also, the surface and interface contributions to XPS spectra are normally small compared to ultraviolet spectra due to the greater electron escape depth resulting from the higher energy photon source. Surface related shifts were probed by collecting spectra at electron emission angles of 30° (surface sensitive) and 75° (bulk sensitive). We observed no shifts in the shallow core levels. Interface related shifts were determined to be less than 0.1 eV based on a comparison of shallow core level energies with deep core levels in bulk and heterojunction samples.

Finally, the Ga 3d and Al 2p core levels studied were actually doublets composed of the $j = 5/2$ and $3/2$ and $j = 3/2$ and $1/2$ contributions, respectively. Since we were concerned only with the relative positions and shifts of each of these peaks, no effort was made to deconvolve these signals and the maximum of the composite was taken as the

peak position. The uncertainty arising from this approximation is smaller than our major sources of error which we attribute to the relatively broad Al K_α x-ray linewidth and our VB edge estimates.

7.2 Zincblende GaN and InN

Figure 7.1 shows the VB spectrum taken on a thick Si-doped zincblende GaN layer compared with the theoretical density of states (DOS), calculated by Lambrecht and Segall [70], which incorporates the effects of the Ga 3d core level (inset). The details of their local density approach (LDA) calculations, to which results we will compare our data throughout this chapter, are summarized in Appendix A, since at present this work is unpublished. Three features are readily observed. A broad peak appears in the vicinity of 3 eV and two more peaks are resolved at binding energies of 7.1 eV and 8.5 eV. Comparing our data with the theoretical DOS, we can assign the 3 eV signal to the N 2p - Ga 4p band and the higher energy peaks to the N 2p - Ga 4s band. The theoretical DOS predicts only a single higher energy peak which does not coincide with our observation of two peaks. Also, the theory predicts the position of the N 2p - Ga 4s peak to be 6 eV, slightly below the experimental value. The LDA approach is known to underestimate the depth of lower lying VBs, so this discrepancy should not be taken too seriously. Qualitatively, our data better resemble the self-energy corrected LDA calculations of Fiorentini et al. [65], who also take into account the Ga 3d core level. Their calculations predict three maxima in the shallow VB DOS.

Figure 7.2 is a spectrum taken on the same GaN layer for slightly higher binding energies showing the Ga 3d core levels to be at 18.4 eV. We do not observe significant evidence of the predicted N 2s - Ga 4s band, with the possible exception of a small low-energy shoulder. Although the predicted N 2s - Ga 4s band DOS is reasonably large, it

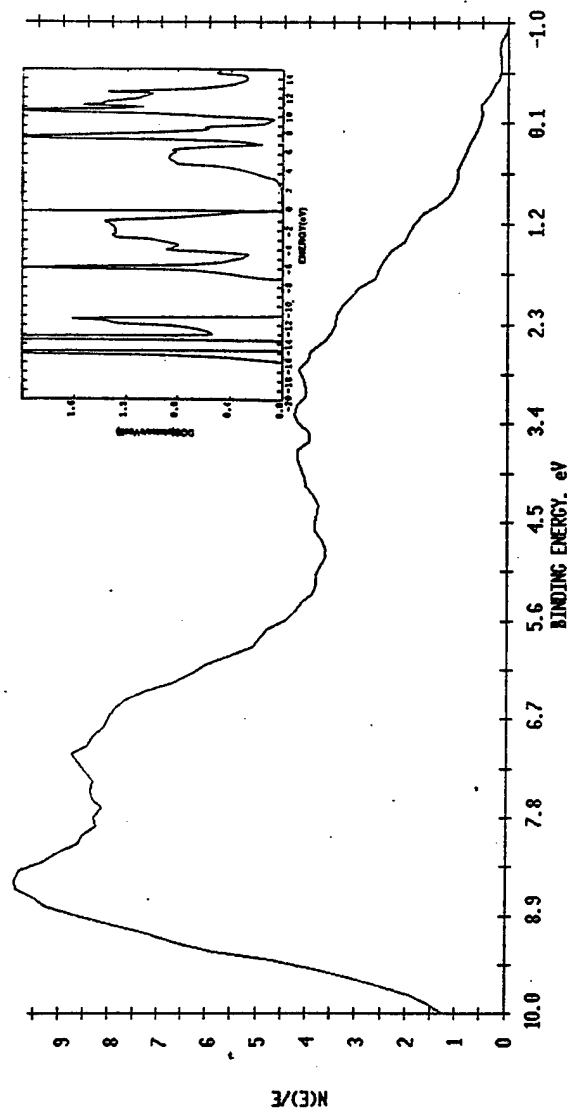


Fig. 7.1. Zincblende GaN upper valence band XPS spectrum. Inset: Calculated DOS of Ref. [70].

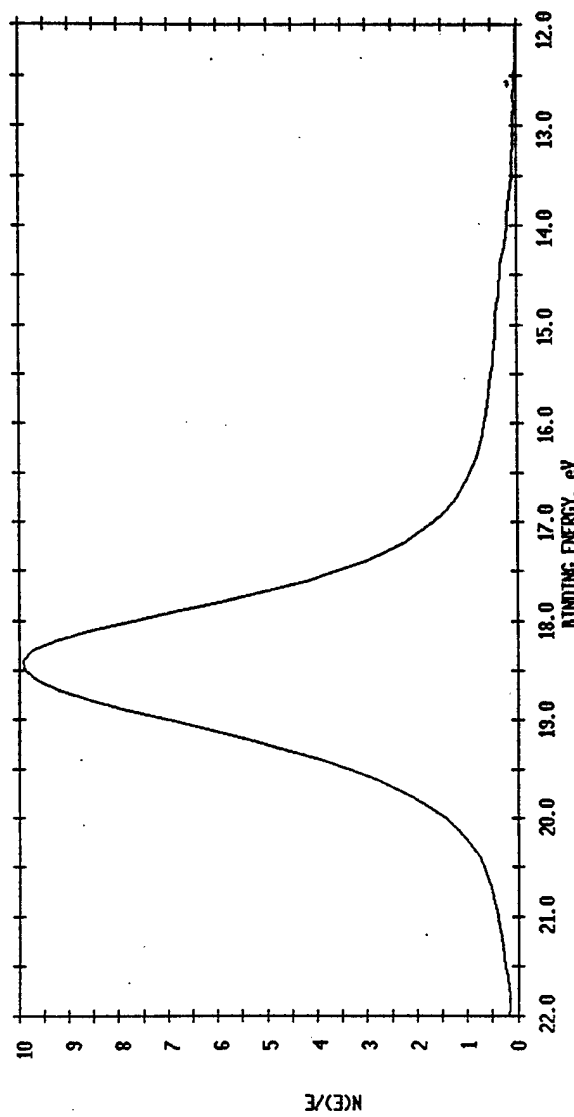


Fig. 7.2. Zincblende GaN Ga 3d core level composite XPS peak.

is difficult to resolve these states by XPS. The x-ray cross sections of the N 2s and Ga 4s orbitals at the Al K_{α} energy are more than a factor of ten less than the sum of the Ga 3d core level cross sections [72]. Also, the predicted DOS [70] of the Ga 3d states is about a factor of three larger than that of the N 2s - Ga 4s band making the expected intensity roughly a factor of thirty less than the Ga 3d signal. Our experimentally determined ionicity gap for zincblende GaN is 6.6 eV compared to the self-energy corrected value of 5.39 eV [65].

The zincblende InN spectrum reveals considerably less structure (Fig. 7.3). The lower energy maximum cannot be resolved from the data. There does appear to be a peak at 7.4 eV. We do not know of any theoretical calculations with which to compare our data, but drawing from the GaN calculations, we can assume that the lower energy signal is the N 2p - In 5p band while the higher energy peak is the N 2p - In 5s band. Our previous study [32] of the zincblende InN material has shown this polytype to be metastable with a strong tendency to revert to the wurtzite polytype. These same InN films were also highly conductive ($n = 10^{20} \text{ cm}^{-3}$). Based on these observations, we attribute the smearing of the VB structure to poor crystal quality and not surface charging.

7.3 Wurtzite GaN, AlN, and InN

Figure 7.4 shows the VB spectrum taken on a thick Si-doped wurtzite GaN layer compared with the theoretical DOS of Ref. [70] and Huang and Ching [69] (inset). A very clear two-tiered spectrum was obtained with maxima at 1.8 eV and 7.5 eV. Both DOS calculations predict two maxima for the N 2p - Ga 4p and the N 2p - Ga 4s bands respectively, which are in reasonable agreement with the experimental data.

A major discrepancy between the two theoretical DOS spectra exists in the lower VB. Huang and Ching, who did not treat the Ga 3d level as a band, predict relatively little

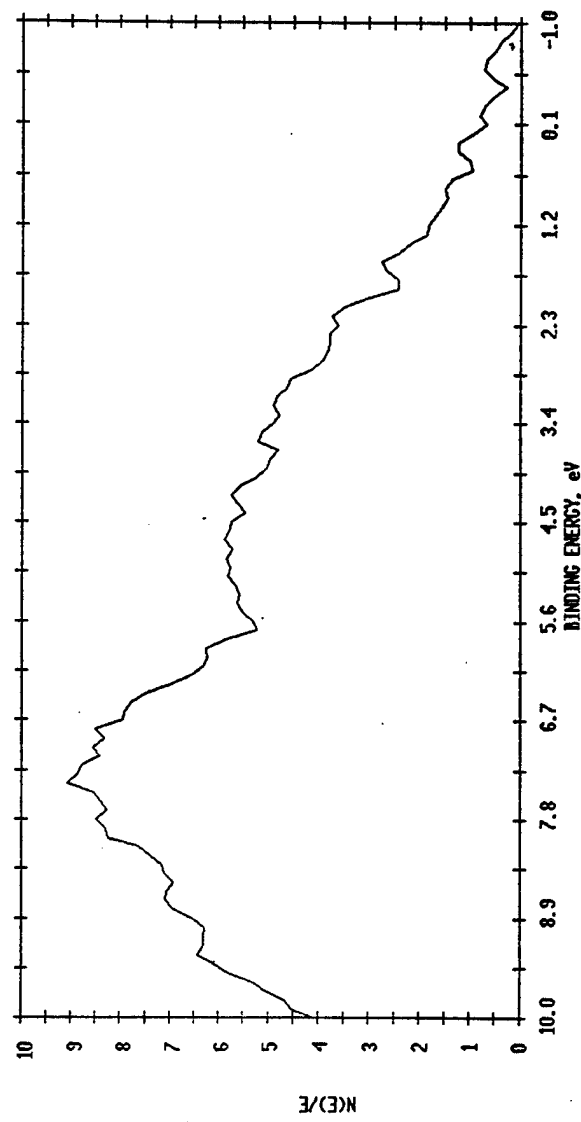


Fig. 7.3. Zincblende InN upper valence band XPS spectrum.

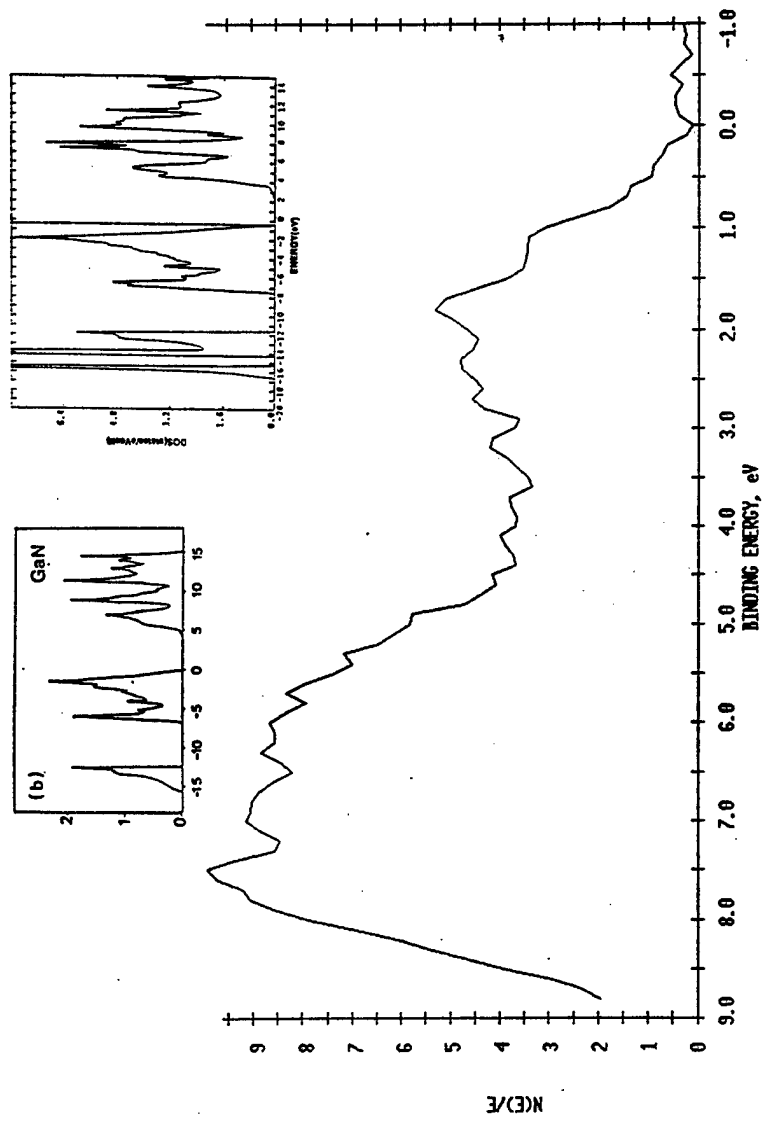


Fig. 7.4. Wurtzite GaN upper valence band XPS spectrum. Inset: Calculated DOS of Refs. [69] (left) and [70] (right).

structure in this region. On the other hand, Lambrecht and Segall calculated a lower VB spectrum which exhibits three large DOS peaks arising from splittings induced by the hybridization of the Ga 3d band with the N 2s - Ga 4s band. Figure 7.5 is a spectrum taken on the same GaN layer for slightly higher binding energies showing the Ga 3d core level peak at 17.2 eV. Again we observe some hint of a shoulder on the low energy side of the Ga 3d signal which may be the predicted N 2s - Ga 4s signal. Unfortunately, due to the lower cross section of these bands and our limited resolution, a definitive study of the structure of this valence band will have to wait for an ultraviolet (uv) photoemission study. Our experimentally observed ionicity gap was 6.6 eV.

Figure 7.6 shows the data taken on a thick Si-doped AlN layer compared with three theoretical DOS (inset). Maxima are observed at \sim 1.9 eV and at 5.7 eV. Olson et al. [73] have also reported an AlN XPS spectrum, superimposed on the theoretical DOS of Ching and Harmon [74], which had two peaks in the upper VB. Comparing with the theoretical predictions, we assign these two peaks to the N 2p - Al 3p and N 2p - Al 3s bands, respectively. Due to the lightness of both Al and N, the VB x-ray cross sections are small [72], which is the cause of the increased noise levels in this spectrum. The slopes of the N 2p - Al 3s band high energy falloff and the VB edge are among the sharpest observed so we do not suspect that charging effects are present in this spectrum despite the larger expected depth of Si donors in this wide bandgap semiconductor.

Al, unlike Ga and In, does not have a low lying d-electron core level. It is interesting to note that the theoretical VB DOS predictions of all three groups are therefore quite similar. Our experimental data from the lower AlN valence band structure is shown in Fig. 7.7. The maximum is centered at 17.5 eV with some evidence of a possible doublet having a \sim 0.5 eV splitting. The low energy edge shows a significant tail which makes our determination of the ionicity gap difficult. Depending on which edge we used for our

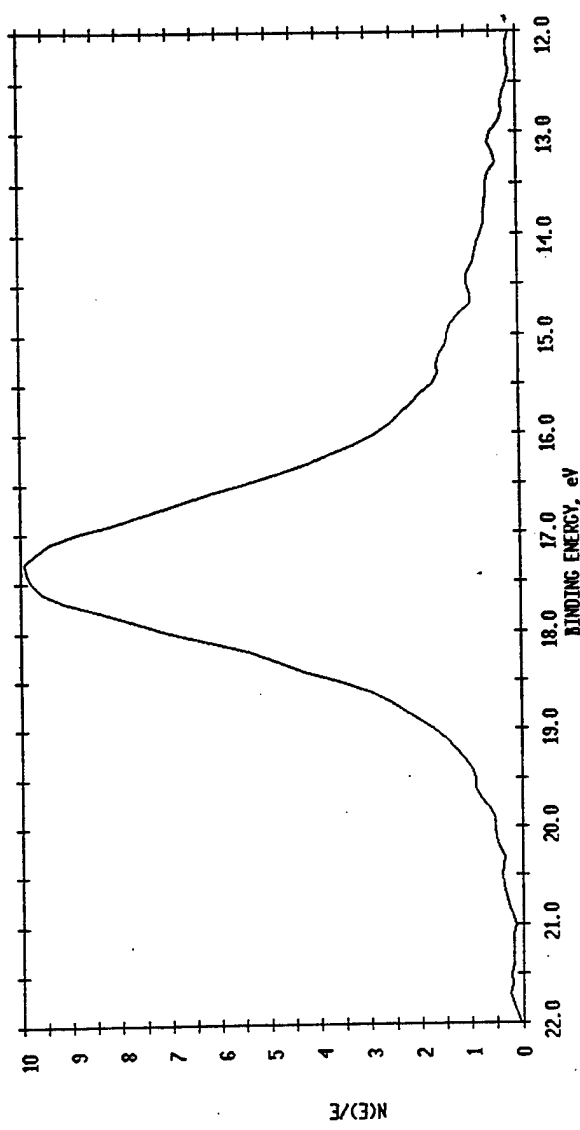


Fig. 7.5. Wurtzite GaN Ga 3d core level composite XPS peak.

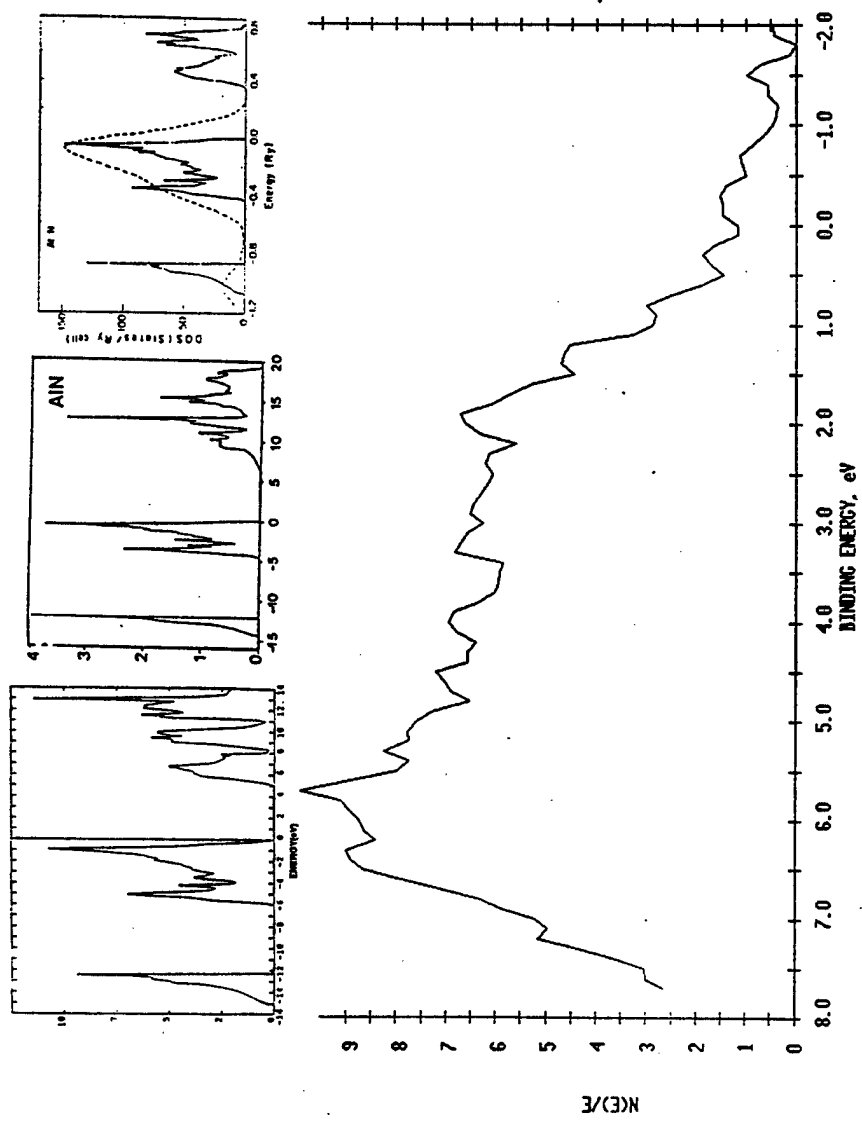


Fig. 7.6. Wurtzite AlN upper valence band XPS spectrum. Inset: Calculated DOS of Refs. [70] (left), [69] (middle) and [74] (right).

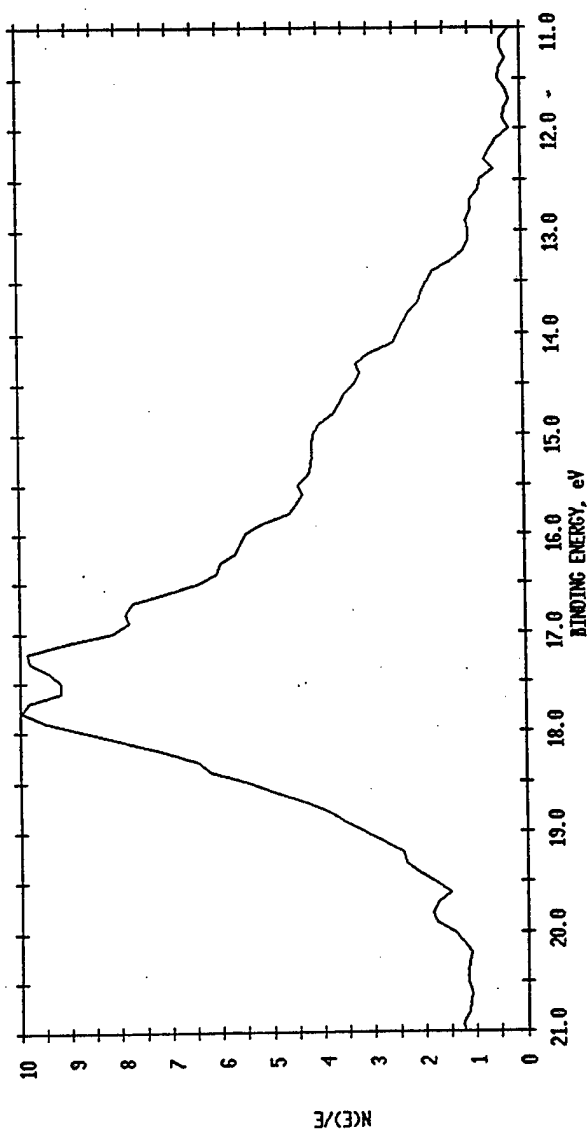


Fig. 7.7. Wurtzite AlN lower valence band XPS spectrum.

extrapolation, we obtained values of 6.2 eV and 4.1 eV for the ionicity gap. Figure 7.8 shows the Al 2p core level signal which is observed at 71.3 eV.

Figure 7.9 shows the data taken on a thick InN sample. Maxima are observed at \sim 1.2 eV and 6.2 eV. We are not aware of any theoretical calculations with which to compare our data but we can again draw from the calculations on the related materials and assume that the lower energy signal is the N 2p - In 5p band and the higher energy peak is the N 2p - In 5s band. We do observe a sharp falloff in the N 2p - In 5s signal which indicates that this sample was reasonably good and can be assumed to be representative of the true wurtzite InN band structure. In, like Ga, has shallow (In 4d) core levels which are expected to strongly hybridize with both the upper and lower valence bands. Our experimental data from the lower InN valence band structure is shown in Fig. 7.10. We observe the maximum of the composite In 4d core level peak to be at 16.1 eV. As was the case for GaN, there is a hint of a low energy N 2s - In 5s shoulder, but better measurements are needed to make a positive determination. Our experimental value for the InN ionicity gap is 5.9 eV. The In $3d_{5/2}$ and $3d_{3/2}$ peaks were observed at 443.0 eV and 450.6 eV, respectively (Fig. 7.11).

7.4 Valence Band Offsets

Photoemission measurements have been applied often in the past to determine heterojunction valence band offsets [75], [76]. Normally, an ultraviolet light source is used because of their relatively narrower line widths. Excellent resolution is necessary since the quantities to be measured require accuracies in the 50 meV range to be of use to device designers. On the other hand, the III-V nitride semiconductors can be probed meaningfully by XPS due to the overall large bandgap differences between AlN and GaN and InN. There has been no previous experimental work attempting to measure the III-V nitride heterojunction band discontinuities despite the critical importance of these quantities for correctly evaluating the potential of these materials for lasers and other optical devices.

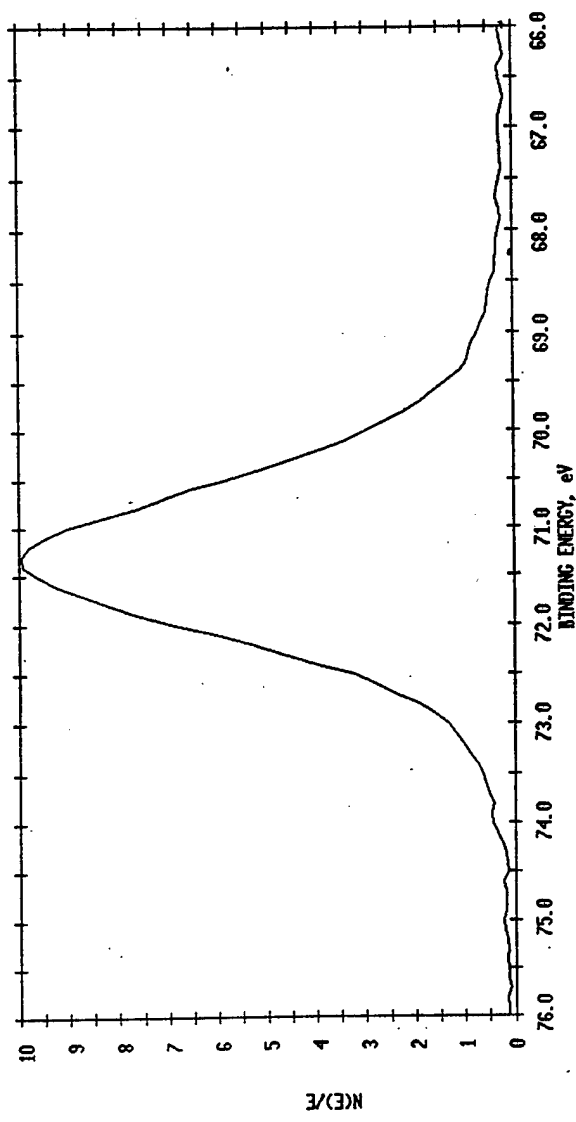


Fig. 7.8. Wurtzite AlN Al 2p core level composite XPS peak.

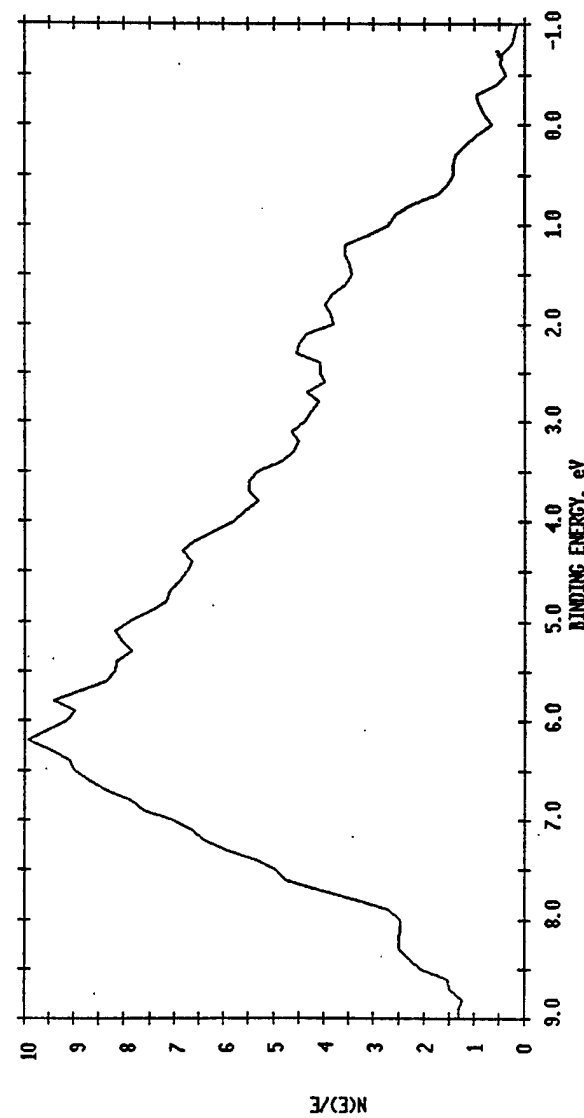


Fig. 7.9. Wurtzite InN upper valence band XPS spectrum.

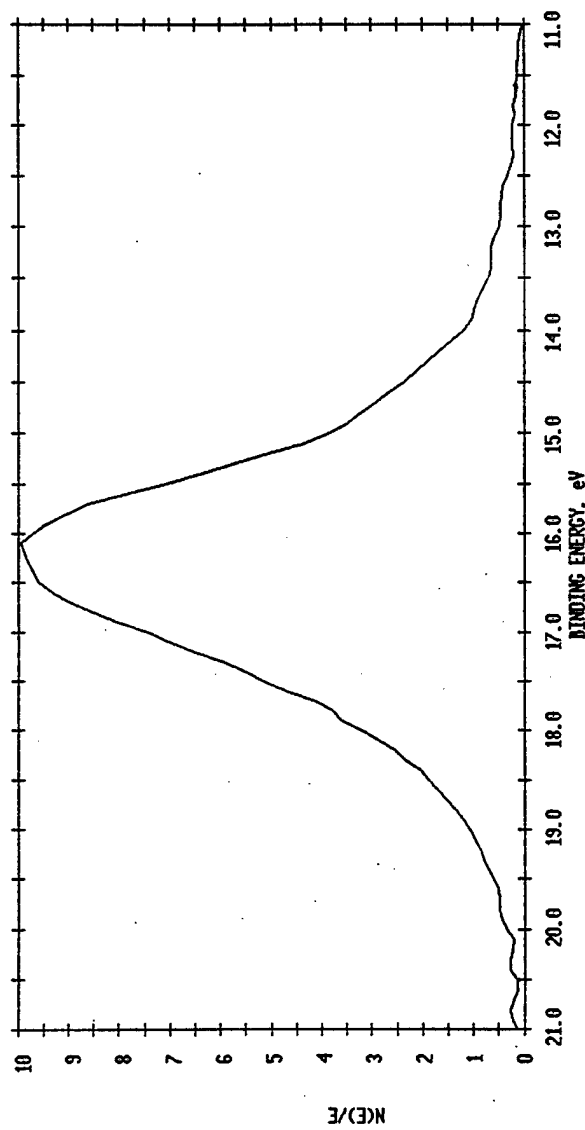


Fig. 7.10. Wurtzite InN In 4d core level composite XPS peak.

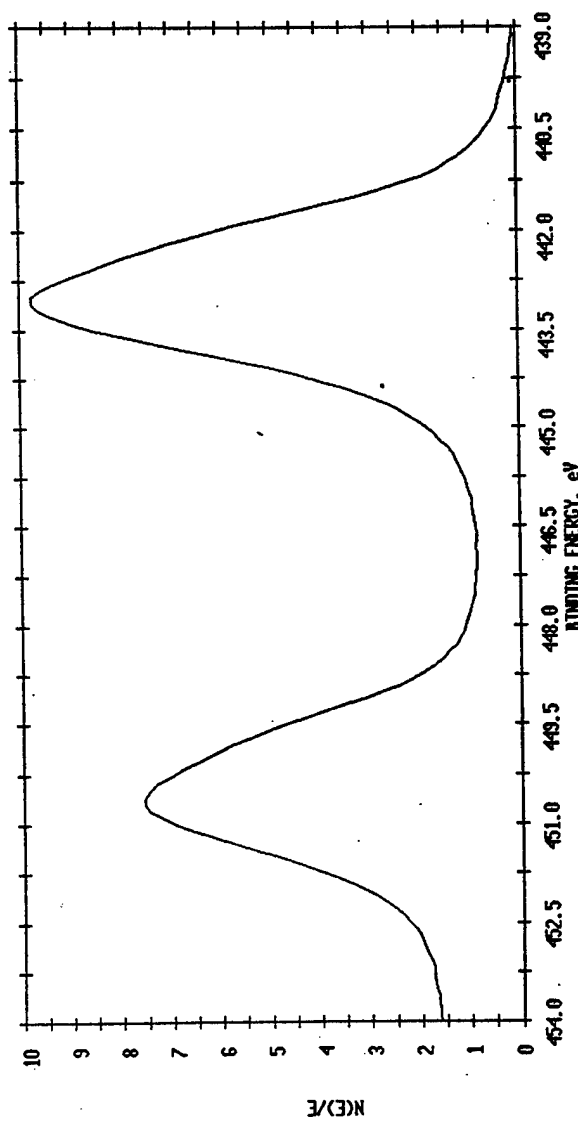


Fig. 7.11. Wurtzite InN In 3d_{3/2} (left) and In 3d_{5/2} (right) core level XPS peaks.

Following the approach of Waldrop et al. [76], illustrated schematically in Fig. 7.12, we obtained core level spectra from thin ($\sim 15 \text{ \AA}$) GaN and InN overlayers on bulk AlN films. Figures 7.13 and 7.14 show the core level spectra collected from the GaN/AlN and InN/AlN heterojunctions, respectively. We attempted, but were unable to resolve a superposition of the valence band edges of both materials in our heterojunctions which would have allowed for a direct measurement of the valence band offset. Table 7.1 summarizes the various relevant core level data used in the VB offset calculations.

Table 7.1 XPS Data Used to Calculate Valence Band Offsets

Epilayer Type	Core Level	Energy Position	FWHM
Bulk AlN	Al 2p	71.3 eV	1.7 eV
Bulk GaN	Ga 3d	17.2 eV	1.6 eV
Bulk InN	In 3d _{5/2}	443.0 eV	2.0 eV
	In 3d _{3/2}	450.6 eV	1.8 eV
15 \AA GaN/AlN	Ga 3d	17.6 eV	2.0 eV
	Al 2p	72.1 eV	1.9 eV
15 \AA InN/AlN	In 3d _{5/2}	443.6 eV	1.7 eV
	In 3d _{3/2}	451.2 eV	1.5 eV
	Al 2p	73.0 eV	1.5 eV

The equations used to calculate the VB offsets are (Fig. 7.12) [76]:

$$\Delta E_v^{\text{AlN, GaN}} = \Delta E_{\text{CL}} + E_{\text{CL}}^{\text{GaN}} - E_{\text{CL}}^{\text{AlN}} \quad 7.1$$

and

$$\Delta E_v^{\text{AlN, InN}} = E_{\text{CL}}^{\text{InN}} - \Delta E_{\text{CL}} - E_{\text{CL}}^{\text{AlN}} \quad 7.2$$

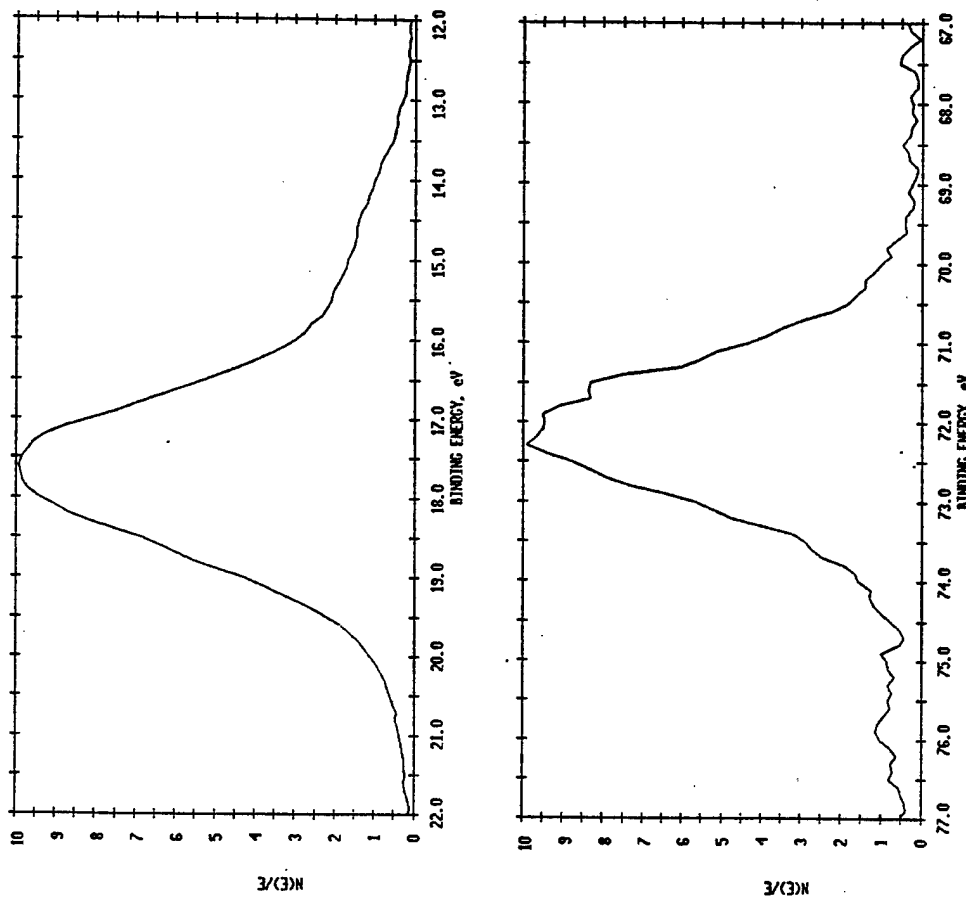


Fig. 7.12. XPS spectra of the Ga 3d (top) and Al 2p (bottom) composite core levels observed on a 15 Å GaN/AlN heterostructure.

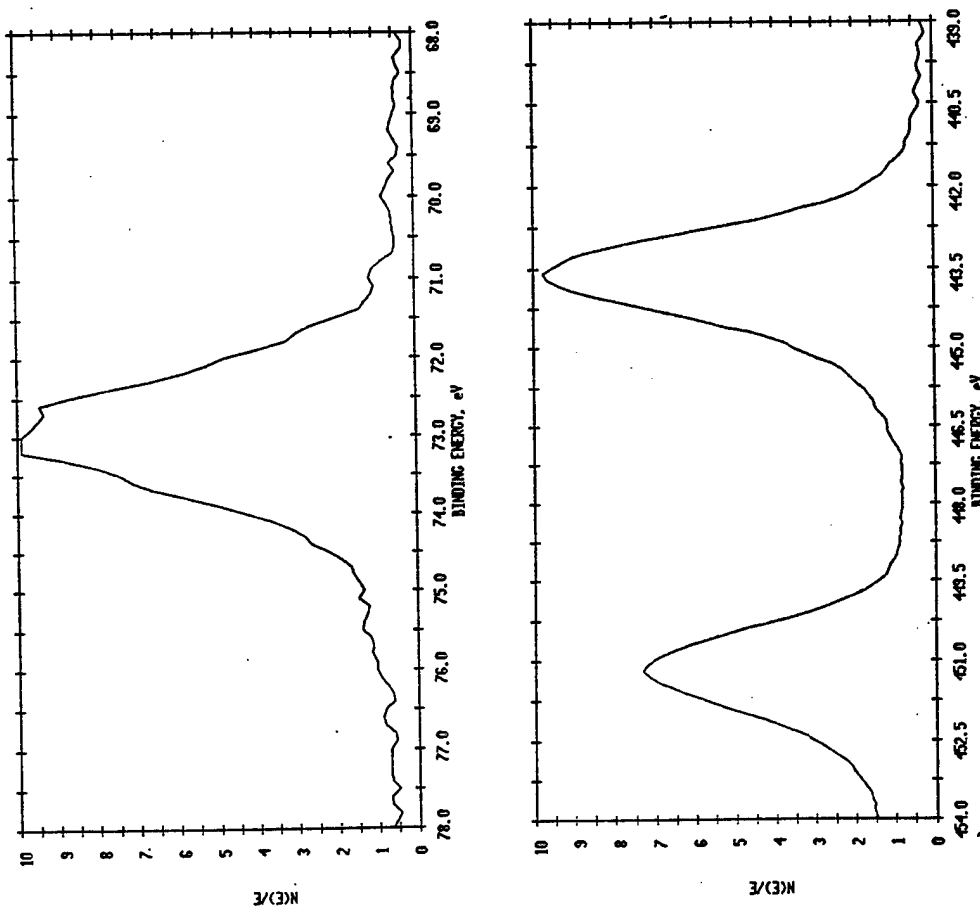
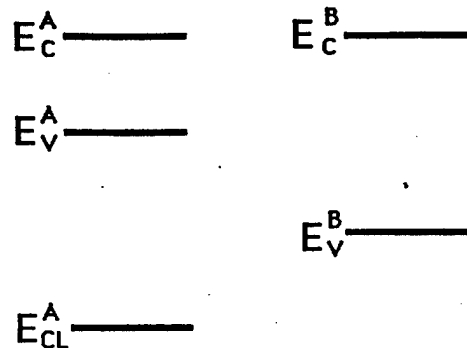


Fig. 7.13. XPS spectra of the Al 2p (top) and In 3d (bottom) core levels observed on a 15 Å InN/AlN heterostructure.

Bulk Band Structures



Heterojunction Band Lineups

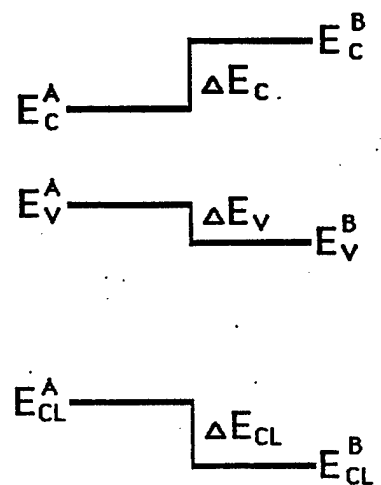


Fig. 7.14. Schematic of the valence band offset measurement approach of Ref. 19 for generic semiconductors A and B. On bulk samples (top), the energy positions of each core level are measured with respect to the valence band edge. Then, on heterojunction samples (bottom), the energy difference between the two core levels is simultaneously measured. From these quantities, the heterojunction valence band offsets are deduced (Eqs. (1) and (2)).

which yielded (Table 7.1):

$$\Delta E_v^{\text{AlN, GaN}} = 54.5\text{eV} + 17.2\text{eV} - 71.3\text{eV} = 0.4\text{eV}$$

7.3

and

$$\Delta E_v^{\text{AlN, InN}} = 443.0\text{eV} - 370.6\text{eV} - 71.3\text{eV} = 1.1\text{eV}.$$

7.4

Figures 7.15 and 7.16 show the full conduction and valence band lineups extrapolated from the VB offset values for these heterojunctions. As discussed in Section 7.1, we attribute the majority of our experimental error to unavoidable broadening resulting from the ~ 1 eV x-ray linewidth and to our determination of the VB edges based on a linear extrapolation of the low energy falloff to the x-axis. Given our experimental FWHM of the core level peaks and the variation observed in the extrapolated VB edge for the largest reasonable variations in our linear fit, a conservative estimate of the maximum possible error in each determination is 0.2 eV. Therefore, we estimate that our VB offset accuracies are accurate to within ± 0.4 eV. Each measurement was repeated several times on different epilayers and the result obtained was always within 0.4 eV of the results quoted above.

The results above should be considered as a first approximation of the actual band lineups in these two heterojunction systems. The measurements described above could be repeated with greater accuracy using an uv photon source which typically have much narrower linewidths. Although the photon energy is insufficient to measure most core level positions, the improved resolution allows the VB leading edges of both materials to be observed on a single scan of a thin heterojunction layer [75]. In this way, the valence band discontinuity can be directly observed rather than deduced as we have done here. An uv measurement would also be able to detect the N 2s - Ga 4s band which was near

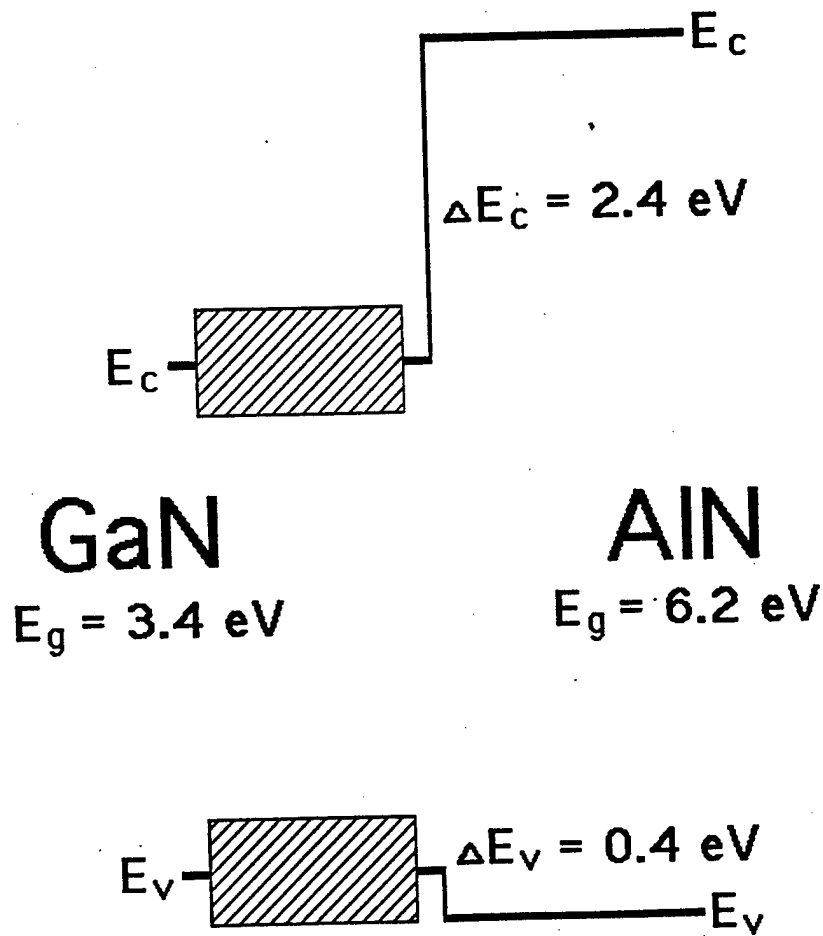


Fig. 7.15. Measured heterojunction band lineups for GaN/AlN. Experimental error is $\pm 0.4 \text{ eV}$.

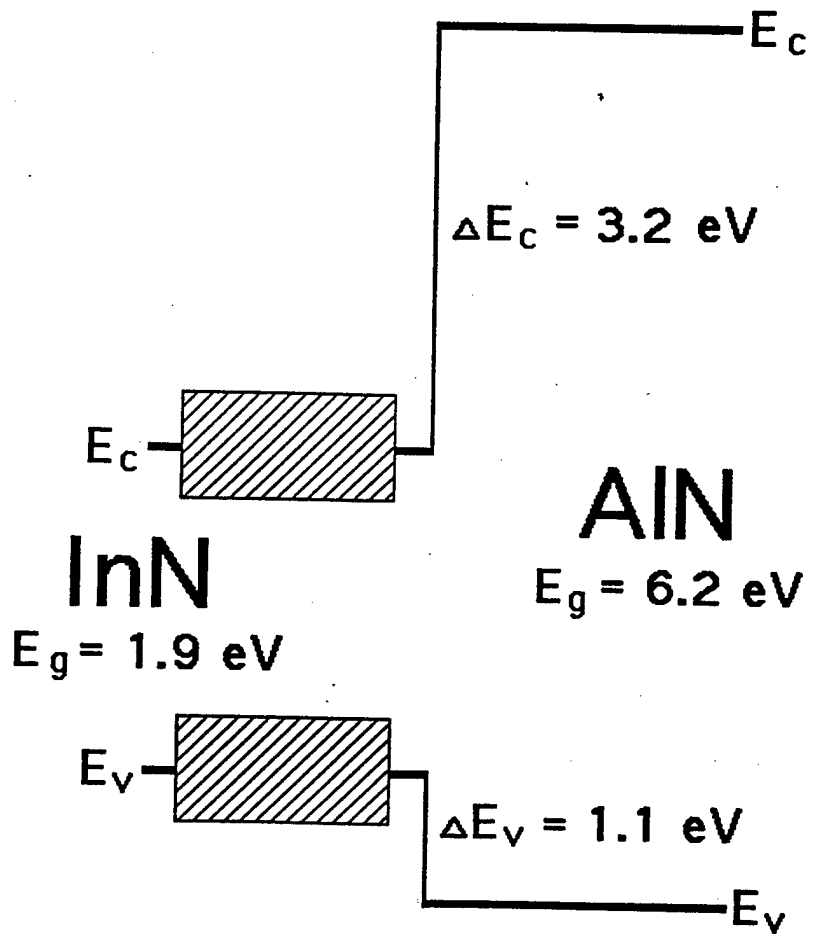


Fig. 7.16. Measured heterojunction band lineups for InN/AlN. Experimental error is $\pm 0.4 \text{ eV}$.

8. CONCLUSIONS

The III-V nitride semiconductors continue to be a frontrunning material system for the development of a semiconductor technology active in the ultraviolet and blue spectrum. This work has attempted to examine some of the relevant issues which will ultimately determine how extensive a role the Group III - Nitrides will play. At the outset of this work, very little was known about the physical properties of the zincblende nitride polytypes. We attempted to measure some of the fundamental physical properties of these materials and to make a determination of their potential for optical device applications. The better understood wurtzite polytypes are already the focus of numerous optical device development efforts. Many of these device designs will rely on the characteristics of AlN/GaN (or similarly AlGaN/GaN) heterojunctions which have not yet been studied in detail.

Our studies of the zincblende polytypes of GaN and InN have revealed, among other things, that zincblende GaN, like its wurtzite counterpart, is a direct bandgap semiconductor having a bandgap active in the near ultraviolet spectrum. In this sense, zincblende GaN has potential for short wavelength optical device applications. However, structural studies of both zincblende GaN and InN have revealed that it will be difficult to obtain good crystal quality in either material due to their tendencies to nucleate wurtzite domains at stacking fault sites. Another study has observed similar behavior in zincblende AlN [18], which has been observed microscopically, but has not yet even been stabilized in bulk form. It appears that the zincblende nitrides, as a material system, offer less potential for development compared to their wurtzite counterparts as a result of their metastability and continued lack of a suitable substrate material.

Based on the conclusions of the first chapters, the focus of our investigation shifted to the wurtzite polytypes. Since the nitrides are primarily of interest as an optical material, and modern optical device designs are almost exclusively of the heterojunction variety,

or below the noise level of our measurements. An energy resolution below 50 meV is routinely obtained with uv light sources, which is sufficiently good to allow engineers to accurately predict device performance and theorists to semi-empirically generate improved band structures.

the heterojunction properties of AlN are of great interest. Our results indicate that at least two thirds of the AlN/GaN and AlN/InN bandgap discontinuities appear across the conduction band leaving relatively little of the bandgap difference at the valence band offset. Furthermore, the true valence band discontinuities may be considerably less than one third of the bandgap difference within our experimental uncertainty. An important criteria by which a heterojunction system is evaluated for quantum well laser applications is the type of band lineup. Three types exist. The forbidden band of the narrow bandgap semiconductor can lie completely within, partially, or completely out of the forbidden band of the larger semiconductor resulting in Type I, II and III heterojunctions, respectively. Only Type I heterojunctions form quantum wells which confine both electrons and holes allowing a population inversion to be most easily reached. Our data show that InN/AlN is clearly Type I while GaN/AlN is almost certainly Type I or at worst, has zero valence band discontinuity. Therefore, despite the unequal heterojunction band lineups observed, each heterojunction is fundamentally suitable for heterojunction laser designs.

APPENDIX A. APPROACH OF LAMBRECHT AND SEGALL

In Chapter 7 we compare our experimental density of state (DOS) measurements with the as yet unpublished theoretically generated DOS of Lambrecht and Segall [70]. In this Appendix, we briefly summarize the calculational approach used to generate these DOS spectra and provide the interested reader with further references describing similar calculations on other wide bandgap semiconductors.

The general framework of the electronic structure calculations is the widely accepted local density functional theory [77], [78]. It is a theory for the ground state of an electronic system which enables the total energy of the bonding of the nuclei with the electrons in a solid to be calculated. Because it is a ground state theory, it is most accurate for the calculation of valence band structure. Basically, it reduces the many-body problem of interacting electrons to an effective single particle problem of one electron in the average potential produced by the fixed nuclear charges and the other electrons. The theory includes correlations and quantum mechanical exchange interactions. In practice, this method requires an iterative solution of the Schrödinger equation for a potential derived from the charge density obtained from the occupied eigenstates themselves. The method of choice for performing these calculations was Andersen's linear muffin tin orbital (LMTO) method [79]. An advantage of this approach for the nitrides is that, being an all electron approach, it has no problems dealing with elements having deep potentials such as nitrogen. Two recent publications by Lambrecht and Segall describe the calculated band structures of zincblende SiC and zincblende AlN [53] by the technique described above and will provide the interested reader with sufficient detail regarding the exact calculational technique used to generate the DOS spectra discussed in Chapter 7.

REFERENCES

- [1] S. Strite and H. Morkoç, "GaN, AlN and InN: a review," *J. Vac. Sci. Technol. B*, vol. 10, pp. 1237-1265, 1992.
- [2] H. P. Maruska and J. J. Tietjen, "The preparation and properties of vapor-deposited single-crystal-line GaN," *Appl. Phys. Lett.*, vol. 15, pp. 327-329, 1969.
- [3] W. Seifert and A. Tempel, "Cubic phase gallium nitride by chemical vapour deposition," *Phys. Status Solidi A*, vol. 23, pp. K39-K40, 1974.
- [4] M. Mizuta, S. Fujieda, Y. Matsumoto, and T. Kawamura, "Low temperature growth of GaN and AlN on GaAs utilizing metalorganics and hydrazine," *Jpn. J. Appl. Phys.*, vol. 25, pp. L945-L948, 1986.
- [5] E. K. Sichel and J. I. Pankove, "Thermal conductivity of GaN, 25-360 K," *J. Phys. Chem. Solids*, vol. 38, p. 330, 1977.
- [6] S. Nakamura, "GaN growth using a GaN buffer layer," *Jpn. J. Appl. Phys.*, vol. 30, pp. L1705-1707, 1991.
- [7] H. Amano, M. Kito, K. Hiramatsu, and I. Akasaki, "P-type conduction in Mg-doped GaN treated with low-energy electron beam irradiation (LEEBI)," *Jpn. J. Appl. Phys.*, vol. 28, pp. L2112-2114, 1989.
- [8] S. Nakamura, N. Iwasa, M. Senoh, and T. Mukai, "Hole compensation mechanism of p-type GaN films," *Jpn. J. Appl. Phys.*, vol. 31, pp. 107-115, 1992.
- [9] S. Nakamura, T. Mukai, and M. Senoh, "Si- and Ge-doped GaN films grown with GaN buffer layers," *Jpn. J. Appl. Phys.*, vol. 31, pp. 195-200, 1992.
- [10] J. I. Pankove, J. E. Berkeyheiser, H. P. Maruska, and J. Wittke, "Luminescent properties of GaN," *Solid State Comm.*, vol. 8, pp. 1051-1053, 1970.
- [11] R. Dingle and M. Illegems, "Donor-acceptor pair recombination in GaN," *Solid State Comm.*, vol. 9, pp. 175-180, 1971.
- [12] R. Dingle, D. D. Sell, S. E. Stokowski, and M. Illegems, "Absorption, reflectance, and luminescence of GaN epitaxial layers," *Phys. Rev. B*, vol. 4, pp. 1211-1218, 1971.
- [13] E. Ejder, "Refractive index of GaN," *Phys. Status Solidi A*, vol. 6, pp. 445-448, 1971.
- [14] K. Matsubara and T. Takagi, "Film growth of GaN on a c-axis oriented ZnO film using reactive ionized-cluster beam technique and its applications to thin film devices," *Jpn. J. Appl. Phys.*, vol. 22, pp. 511-514, 1982.
- [15] W. M. Yim, E. J. Stofko, P. J. Zanzucchi, J. I. Pankove, M. Ettenberg, and S. L. Gilbert, "Epitaxially grown AlN and its optical gap," *J. Appl. Phys.*, vol. 44, pp. 292-296, 1973.
- [16] G. A. Slack, "Nonmetallic crystals with high thermal conductivity," *J. Phys. Chem. Solids*, vol. 34, pp. 321-335, 1973.

- [17] W. M. Yim and R. J. Paff, "Thermal expansion of AlN, sapphire and silicon," *J. Appl. Phys.*, vol. 45, pp. 1456-1457, 1974.
- [18] R. F. Davis, "Plasma-assisted MBE grown III-V nitride epilayers on SiC," *Workshop on the Widegap Nitrides*, St. Louis, 1992.
- [19] I. Petrov, E. Mojab, R. C. Powell, J. E. Greene, L. Hultman, and J.-E. Sundgren, "Synthesis of metastable epitaxial zinc-blende-structure AlN by solid-state reaction," *Appl. Phys. Lett.*, vol. 60, pp. 2491-2493, 1992.
- [20] J. Edwards, K. Kawabe, G. Stevens, and R. H. Tredgold, "Space charge conduction and electrical behavior of aluminum nitride single crystals," *Solid State Comm.*, vol. 3, pp. 99-100, 1965.
- [21] K. Kawabe, R. H. Tredgold, and Y. Inuishi, "Electrical and optical properties of AlN - a thermostable semiconductor," *Elect. Eng. Jpn.*, vol. 87, pp. 62-70, 1967.
- [22] G. A. Cox, D. O. Cummins, K. Kawabe, and R. H. Tredgold, "On the preparation, optical properties and electrical behavior of aluminum nitride," *J. Phys. Chem. Solids*, vol. 28, pp. 543-8, 1967.
- [23] J. Duchene, "Radiofrequency reactive sputtering for deposition aluminum nitride thin films," *Thin Solid Films*, vol. 8, pp. 69-79, 1971.
- [24] J. Pastrnak and L. Roskovcova, "Refractive index measurements on AlN single crystals," *Phys. Status Solidi*, vol. 14, pp. K5-K8, 1966.
- [25] I. Akasaki and H. Hashimoto, "Infrared lattice vibrations of vapour-grown AlN," *Solid State Comm.*, vol. 5, pp. 851-853, 1967.
- [26] E. A. Irene, V. J. Silvestri, and G. R. Woolhouse, "Some properties of chemical vapor deposited films of $Al_xO_yN_z$ on silicon," *J. Electron. Mater.*, vol. 4, pp. 409-426, 1975.
- [27] J. Bauer, L. Biste, and D. Bolze, "Optical properties of aluminum nitride prepared by chemical and plasmachemical vapour deposition," *Phys. Status Solidi A*, vol. 39, pp. 173-181, 1977.
- [28] A. T. Collins, E. C. Lightowers, and P. J. Dean, "Lattice vibration spectrum of aluminum nitride," *Phys. Rev.*, vol. 158, pp. 833-838, 1967.
- [29] J. W. Trainor and K. Rose, "Some properties of InN films prepared by reactive evaporation," *J. Electron. Mater.*, vol. 3, pp. 821-828, 1974.
- [30] J. B. MacChesney, P. M. Bridenbaugh, and P. B. O'Connor, "Thermal stability of indium nitride at elevated temperature and nitrogen pressures," *Mater. Res. Bull.*, vol. 5, pp. 783-792, 1970.
- [31] T. L. Tansley and C. P. Foley, "Optical bandgap of indium nitride," *J. Appl. Phys.*, vol. 59, pp. 3241-3244, 1986.
- [32] S. Strite, D. Chandrasekhar, David J. Smith, B. Sariel, H. Chen, N. Teraguchi, and H. Morkoç, "Structural properties of InN films grown on GaAs substrates: observation of the zincblende polytype," *J. Crystal Growth*, in press.

- [33] T. L. Tansley and C. P. Foley, "Electrical mobility of indium nitride," *Electronics Lett.*, vol. 20, pp. 1066-1068, 1984.
- [34] Cree Research Inc., 2810 Meridian Pkwy., Durham, NC 27713.
- [35] M. E. Lin, S. Strite, A. Agarwal, A. Salvador, G. L. Zhou, N. Teraguchi, A. Rockett, and H. Morkoç, "GaN grown on hydrogen plasma cleaned 6H-SiC substrates," *Appl. Phys. Lett.*, in press.
- [36] B. S. Meyerson, F. J. Himpsel, and K. J. Uram, "Bi-stable conditions for low-temperature Si epitaxy," *Appl. Phys. Lett.*, vol. 57, pp. 1034-1036, 1990.
- [37] I. Suemune, Y. Kunitsugu, Y. Tanaka, Y. Kan, and M. Yamanishi, "New low-temperature process for growth of GaAs on Si with metalorganic molecular beam epitaxy assisted by a hydrogen plasma," *Appl. Phys. Lett.*, vol. 53, pp. 2173-2175, 1992.
- [38] G. Hollinger and F.J. Himpsel, "Probing the transition layer at the SiO₂-Si interface using core level photoemission," *Appl. Phys. Lett.*, vol. 44, pp. 93-95, 1984.
- [39] M. T. Wauk and D. K. Winslow, "Vacuum deposition of AlN acoustic transducers," *Appl. Phys. Lett.*, vol. 13, pp. 286-288, 1968.
- [40] B. B. Kosicki and D. Kahng, "Preparation and structural properties of GaN thin films," *J. Vac. Sci. Technol.*, vol. 6, pp. 593-596, 1969.
- [41] K. Osamura, S. Naka, and Y. Murakami, "Preparation and optical properties of Ga_{1-x}In_xN films," *J. Appl. Phys.*, vol. 46, pp. 3432-3437, 1975.
- [42] S. Zembutsu and T. Sasaki, "Low temperature growth of GaN single crystal films using electron cyclotron resonance excited metalorganic vapor phase epitaxy," *J. Cryst. Growth*, vol. 77, pp. 250-256, 1986.
- [43] M. J. Paisley, Z. Sitar, J. B. Posthill, and R. F. Davis, "Growth of cubic phase gallium nitride by modified molecular-beam epitaxy," *J. Vac. Sci. Technol. A*, vol. 7, pp. 701-705, 1989.
- [44] S. Strite, J. Ruan, Z. Li, N. Manning, A. Salvador, H. Chen, David J. Smith, W. J. Choyke, and H. Morkoç, "An investigation of the properties of cubic GaN grown on GaAs by plasma-assisted molecular-beam epitaxy," *J. Vac. Sci. Technol. B*, vol. 9, pp. 1924-1929, 1991.
- [45] T. Lei, M. Fanciulli, R. J. Molnar, T. D. Moustakas, R. J. Graham, and J. Scanlon, "Epitaxial growth of zincblende and wurtzitic gallium nitride thin films on (001) silicon," *Appl. Phys. Lett.*, vol. 59, pp. 944-946, 1991.
- [46] T. Lei, K. F. Ludwig, and T. D. Moustakas, "Heteroepitaxy, polymorphism and faulting in GaN thin films on silicon and sapphire substrates," *J. Appl. Phys.*, in press
- [47] T. Lei, private communication, 1991.
- [48] S. Strite, D. S. L. Mui, G. Martin, Z. Li, David J. Smith, and H. Morkoç, "An investigation of the structural and insulating properties of cubic GaN for GaAs-GaN semiconductor-insulator devices," *Inst. Phys. Conf. Ser.*, vol. 120, pp. 89-93, 1992.

- [49] G. Martin, S. Strite, J. Thornton, and H. Morkoç, "Electrical properties of GaAs/GaN/GaAs semiconductor-insulator-semiconductor structures," *Appl. Phys. Lett.*, vol. 58, pp. 2375-2377, 1991.
- [50] Z. Sitar, M. J. Paisley, B. Yan, J. Ruan, W. J. Choyke, and R. F. Davis, "Growth of AlN/GaN layered structures by gas source molecular-beam epitaxy," *J. Vac. Sci. Technol. B*, vol. 8, pp. 316-321, 1990.
- [51] T. Sasaki and T. Matsuoka, "Substrate polarity dependence on metal-organic vapor-phase epitaxy-grown GaN on SiC," *J. Appl. Phys.*, vol. 64, pp. 4531-4535, 1988.
- [52] S. Bloom, G. Harbecke, E. Meier, and I. B. Ortenburger, "Band structure and reflectivity of GaN," *Phys. Status Solidi B*, vol. 66, pp. 161-168, 1974.
- [53] W. R. L. Lambrecht and B. Segall, "Electronic structure and bonding at SiC/AlN and SiC/BP interfaces," *Phys. Rev. B*, vol. 43, pp. 7070-7085, 1991.
- [54] D. W. Jenkins, R.-D. Hong, and J. D. Dow, "Band structure of InN," *Superlatt. Microstruct.*, vol. 3, pp. 365-369, 1987.
- [55] T. P. Humphreys, C. A. Sukow, R. J. Nemanich, J. B. Posthill, R. A. Rudder, S. V. Hattangaddy, and R. J. Markunas, "Microstructural and optical characterization of GaN films grown by PECVD on (0001) sapphire," *Mater. Res. Soc. Symp. Proc.*, vol. 162, pp. 531-536, 1990.
- [56] J. I. Pankove, J. E. Berkeyheiser, and E. A. Miller, "Properties of Zn-doped GaN. I. Photoluminescence," *J. Appl. Phys.*, vol. 45, pp. 1280-1286, 1974.
- [57] P. Bergman, G. Ying, B. Monemar, and M. Illegems, "Time-resolved spectroscopy of Zn- and Cd-doped GaN," *J. Appl. Phys.*, vol. 61, pp. 4589-4592, 1987.
- [58] B. Monemar, "Fundamental energy gap of GaN from photoluminescence excitation," *Phys. Rev. B*, vol. 10, pp. 676-681, 1974.
- [59] R. C. Powell, G. A. Tomasch, Y.-W. Kim, J. A. Thornton, and J. E. Greene, "Growth of high-resistivity wurtzite and zincblende structure single crystal GaN by reactive-ion molecular beam epitaxy," *Mater. Res. Soc. Symp. Proc.*, vol. 162, pp. 525-530, 1990.
- [60] T. Hariu, T. Usuba, H. Adachi, and Y. Shibata, "Reactive sputtering of gallium nitride thin films for GaAs MIS structures," *Appl. Phys. Lett.*, vol. 32, pp. 252-253, 1978.
- [61] D. S. L. Mui, H. Liaw, A. L. Demirel, S. Strite, and H. Morkoç, "Electrical characteristics of $\text{Si}_3\text{N}_4/\text{Si}/\text{GaAs}$ metal-insulator-metal capacitor," *Appl. Phys. Lett.*, vol. 59, pp. 2847-2849, 1991.
- [62] D. S. L. Mui, D. Biswas, J. Reed, A. L. Demirel, S. Strite, and H. Morkoç, "Investigations of the $\text{Si}_3\text{N}_4/\text{Si}/\text{GaAs}$ insulator-semiconductor interface with low interface trap density," *Appl. Phys. Lett.*, vol. 60, pp. 2511-2513, 1992.
- [63] E. H. Nicollian and J. R. Brews, "MOS Physics and Technology," Wiley, New York, 1982.

- [64] S. M. Sze, "Physics of Semiconductor Devices," Wiley, New York, p. 256, 1981.
- [65] V. Fiorentini, M. Methfessel, and M. Scheffler, "Electronic and structural properties of GaN by the full-potential LMTO method: the role of the d electrons," preprint.
- [66] S.-H. Wei and Alex Zunger, "Role of metal d states in II-VI semiconductors," *Phys. Rev. B*, vol. 37, pp. 8958-8981, 1988.
- [67] B. J. Min, C. T. Chan, and K. M. Ho, "First-principles total-energy calculation of gallium nitride," *Phys. Rev. B*, vol. 45, pp. 1159-1162, 1992.
- [68] M. Palummo, C. M. Bertoni, L. Reining, and F. Finocchi, unpublished
- [69] Ming-Zhu Huang and W. Y. Ching, "A minimal basis semi-ab initio approach to the band structures of semiconductors," *J. Phys. Chem. Solids*, vol. 46, pp. 977-995, 1985.
- [70] W. R. L. Lambrecht and B. Segall, unpublished data.
- [71] I. Lindau and W. E. Spicer, "The probing depth in photoemission and Auger-electron spectroscopy," *J. Electron Spec. and Related Phen.*, vol. 3, pp. 409-413, 1974.
- [72] J. H. Scofield, "Hartree-Slater subshell photoionization cross-sections at 1254 and 1487 eV," *J. Electron Spec. and Related Phen.*, vol. 8, pp. 129-137, 1976.
- [73] C. G. Olsen, J. H. Sexton, D. W. Lynch, A. J. Bevolo, H. R. Shanks, B. N. Harmon, W. Y. Ching, and D. M. Wieliczka, "Photoelectron and electron energy loss spectra of epitaxial aluminum nitride," *Solid State Comm.*, vol. 56, pp. 35-37, 1985.
- [74] W. Y. Ching and B. N. Harmon, "Electronic structure of AlN," *Phys. Rev. B*, vol. 34, pp. 5305-5308, 1986.
- [75] A. D. Katnani and G. Magaritondo, "Microscopic study of semiconductor heterojunctions: Photoemission measurement of the valence-band discontinuity and of the potential barriers," *Phys. Rev. B*, vol. 28, pp. 1944-1956, 1983.
- [76] J. R. Waldrop, R. W. Grant, S. P. Kowalczyk, and E. A. Kraut, "Measurement of semiconductor heterojunction band discontinuities by x-ray photoemission spectroscopy," *J. Vac. Sci. Technol. A*, vol. 3, pp. 835-841, 1985.
- [77] P. Hohenberg and W. Kohn, "Inhomogeneous electron gas," *Phys. Rev.*, vol. 136, pp. B864-B871, 1964.
- [78] W. Kohn and L. J. Sham, "Self-consistent equations including exchange and correlation effects," *Phys. Rev.*, vol. 140, pp. A1133-A1138, 1965.
- [79] O. K. Andersen, "Linear methods in band theory," *Phys. Rev. B*, vol. 12, pp. 3060-3083, 1975.

VITA

Samuel Clagett Strite III was born in Poughkeepsie, New York on March 15, 1965. A graduate of Wootton High School in Rockville, Maryland, he enrolled at Bucknell University in the Fall of 1983. In May 1987, he received a Bachelor of Science degree cum laude with honors in physics. He was awarded the Norwood T. Lowery Prize given to the outstanding graduating senior in physics and a three year National Science Foundation Fellowship for graduate study. In the Fall of 1987, he commenced the PhD program of the Physics Department at the University of Illinois at Urbana-Champaign.

He began his graduate research career in March 1988 as a Research Assistant in the High Speed Devices Laboratory of Professor H. Morkoç, and received the M.S. degree in Physics from the University of Illinois at Urbana-Champaign, in October 1988. Midway through his graduate studies in the Fall of 1990, he was awarded a three year Air Force Office of Scientific Research Graduate Fellowship. In his graduate career, he has worked on the molecular beam epitaxial growth and characterization of numerous semiconductor materials. He has authored or coauthored more than thirty peer reviewed journal articles and thirteen conference papers.